

中国科学技术大学

博士学位论文



RHIC-STAR 200GeV 质子-质子和 金核-金核对撞中重味强子衰变电子 的测量

作者姓名： 张生辉

学科专业： 粒子物理与原子核物理

导师姓名： 李澄 教授 张一飞 副教授 叶震宇 副教授

完成时间： 二〇一八年七月二十三日

University of Science and Technology of China
A dissertation for doctor's degree



**Measurements of electrons from
open heavy flavor hadron decays
in p+p and Au+Au collisions at
 $\sqrt{s_{NN}} = 200$ GeV by the STAR
experiment**

Author: Shenghui Zhang

Speciality: Particle and Nuclear Physics

Supervisors: Prof. Cheng Li, Prof. Yifei Zhang, Prof. Zhenyu Ye

Finished time: July 23, 2018

中国科学技术大学学位论文原创性声明

本人声明所呈交的学位论文，是本人在导师指导下进行研究工作所取得的成果。除已特别加以标注和致谢的地方外，论文中不包含任何他人已经发表或撰写过的研究成果。与我一同工作的同志对本研究所做的贡献均已在论文中作了明确的说明。

作者签名： _____

签字日期： _____

中国科学技术大学学位论文授权使用声明

作为申请学位的条件之一，学位论文著作权拥有者授权中国科学技术大学拥有学位论文的部分使用权，即：学校有权按有关规定向国家有关部门或机构送交论文的复印件和电子版，允许论文被查阅和借阅，可以将学位论文编入《中国学位论文全文数据库》等有关数据库进行检索，可以采用影印、缩印或扫描等复制手段保存、汇编学位论文。本人提交的电子文档的内容和纸质论文的内容相一致。

保密的学位论文在解密后也遵守此规定。

公开 保密（____ 年）

作者签名： _____

导师签名： _____

签字日期： _____

签字日期： _____

摘要

量子色动力学 (QCD) 是用来描述自然界四大基本作用力之一的强相互作用的基本规范场理论。众所周知, 强相互作用的基本粒子是夸克和胶子, 并且具有两个显著特征: 渐近自由和色禁闭。由于色禁闭, 在正常条件下, 实验上尚未观测到自由夸克, 这意味着夸克总是被束缚在色单态的强子内。格点 QCD 计算预言在高温高能量密度的极端条件下会发生从强子气到夸克解禁闭的新物质形态夸克胶子等离子体 (QGP) 的相变。在实验上通过高能重离子碰撞形成高温高密的极端条件来寻找 QGP 并研究它的性质。位于美国布鲁克海文国家实验室 (BNL) 的相对论重离子对撞机 (RHIC) 通过核核碰撞来研究 QGP 的性质以及 QCD 相图。RHIC 自 2000 年运行以来, 在重离子碰撞中发现了大量 QGP 存在的实验证据, 例如“喷注淬火”现象、椭圆流的组分夸克标度性等等。这些实验结果表明在 RHIC 已经形成了强耦合的夸克胶子等离子体 (sQGP), 下一步的核心问题是研究 QGP 的特性以及 QCD 物质的相结构。

由于重味夸克 (粲夸克和底夸克) 的质量比较大, 粲夸克约为 $1.3 \text{ GeV}/c^2$ 和底夸克约为 $4.2 \text{ GeV}/c^2$, 远远大于 Λ_{QCD} (QCD 标度参数) 和 T_{QGP} , 所以它们被认为主要通过胶子聚合在重离子碰撞早期 (QGP 产生之前) 的硬散射过程产生。这就意味着这些重味夸克会经历 QGP 演化的所有阶段, 从而其运动学会携带关于与 QGP 相互作用的信息。因此重味夸克被认为是研究 QGP 性质的理想探针。同时由于重味夸克产生时的大横动量转移, 其截面可以被微扰 QCD 理论计算。理论计算预言, 由于死锥效应, 重味夸克通过胶子辐射损失的能量要比轻夸克少。因此测量重味夸克强子半轻子道衰变电子的核修正因子, 对于我们理解 RHIC 能区核核碰撞部分子的能损机制及 QGP 性质都有着重要意义。特别是, 粲夸克和底夸克核修正因子的分离测量对验证部分子能量损失的质量依赖性至关重要。

本篇论文利用位于 RHIC 上的螺旋径迹探测器 (STAR), 研究了重味夸克强子衰变电子在 200 GeV 质子-质子碰撞中低横动量区的产生和在 200 GeV 金核-金核碰撞中高横动量区的产生。用于本篇论文分析的实验数据是 STAR 分别于 2012 年和 2014 年采集的最小无偏质子-质子碰撞和电磁量能器触发的金核-金核碰撞的数据。利用 STAR 时间投影室提供的电离能损, 在低横动量区结合飞行时间探测器测量的粒子速度和在高横动量区结合桶部电磁量能器测量的簇射总能量 (金核-金核碰撞中额外使用簇射最大探测器测量的簇射形状) 进行电子鉴别。同时电磁过程产生的电子本底 (光子转换, 轻中性介子 π^0 和 η 达利兹衰变) 通过重建标记电子 (正电子) 和所有伴随正电子 (电子) 的不变质量在统计上扣除。经过来自于纯电子样本数据、STAR 探测器模拟和蒙塔卡罗样本分析的效率修正,

我们获得了重味夸克强子衰变电子在质子-质子碰撞中的低横动量微分截面谱和在金核-金核碰撞中不同碰撞中心度下的高横动量不变产额谱。

在质子-质子碰撞中,重味夸克强子衰变电子的微分截面谱在横动量大于 $0.5 \text{ GeV}/c$ 的区间能够被微扰 QCD 理论模型计算很好的描述。而在极低横动量区间, QCD 理论计算低估了电子的产额, 这为以后理论模型的计算提供了实验参考限制。同时这个测量也为重味夸克强子衰变电子在金核-金核碰撞中核修正因子的测量提供了高精度的参考基线。这也是 STAR 第一次将重味夸克强子衰变电子的测量扩展到低横动量区。

在金核-金核碰撞中,相比于之前 STAR 发表的结果, 本论文提高了重味夸克强子衰变电子的不变产额谱和核修正因子的测量精度。在金核-金核对心碰撞中,重味夸克强子衰变电子的不变产额谱明显偏离(低于)核子核子碰撞数目 (N_{coll}) 标度的微扰 QCD 理论计算值, 这表明热核物质效应的存在, 并且从对心到偏心碰撞, 这个偏离变得越来越小, 与偏心碰撞中核物质效应小的预期是相符的。同时, 在金核-金核对心碰撞中, 重味夸克强子衰变电子的核修正因子在高横动量区观测到强烈的压低, 这与重味夸克在致密物质 QGP 里的能量损失一致, 为理论研究重味夸克与 QGP 相互作用的能损机制和 QGP 的性质提供重要的实验参考。更进一步地, 核修正因子的测量也为粲夸克和底夸克的分离测量提供了总的核修正因子, 这为部分子能量损失的质量依赖性的验证创造了条件。

关键词: 量子色动力学; 夸克胶子等离子体; 重味夸克; 半轻子道衰变电子; 横动量谱; 核修正因子; 粲夸克底夸克分离

ABSTRACT

Quantum ChromoDynamics (QCD) is a basic gauge field theory of strong interaction, a fundamental force describing the interactions between quarks and gluons. The strong interaction has two distinctive features: asymptotic freedom and color confinement. Due to color confinement, free quarks have not been observed experimentally under normal conditions. Instead, they are confined within the color-neutral hadrons. The Lattice QCD calculation predicts a phase transition from hadronic gas to a new matter Quark Gluon Plasma (QGP), in which quarks are deconfined, at high temperature and energy density. Experimentally, QGP could be created and studied via high-energy heavy-ion collisions. The Relativistic Heavy Ion Collider (RHIC) at the Brookhaven National Laboratory (BNL) in the United States is a dedicated machine to study the properties of QGP and QCD phase diagram through nucleus-nucleus collisions. Plenty of measurements from RHIC experiments, such as “jet-quenching” and Number of Constituent Quark (NCQ) scaling of elliptic flow, show that a strongly coupled QGP (sQGP) has been formed at RHIC. The next step is to study the QGP properties and the QCD phase structure.

Due to the masses of the heavy quarks (charm and bottom quark) are larger than the Λ_{QCD} (one of QCD scale parameters) and T_{QGP} , they are believed to be dominantly produced in hard scatterings via gluon fusions before the creation of QGP at the early stage of heavy-ion collisions. This means these heavy quarks experience the entire QGP evolution and their kinematics carry the information about their interactions with QGP. Thus, the heavy quarks are suggested as an ideal probe for studying the properties of the QGP. Meanwhile, due to the high transverse momentum transfers when heavy quark produced, their cross-section can be calculated by perturbative QCD (pQCD) theory. Theory predicts heavy quarks lose less energy than light quarks through gluon radiation due to the suppressed radiation angle of the gluon, the so-called “dead cone” effect. Therefore, measuring the nuclear modification factors of the semi-leptonic decayed electrons from open heavy flavor quark hadrons is very important to understand the parton energy loss mechanism and QGP properties in nucleus-nucleus collisions at RHIC energies. In particular, the separate measurements for the nuclear modification factors of heavy quarks are crucial to test the mass hierarchy of the parton energy loss in the QGP.

In this thesis, the data taken by the Solenoidal Tracker at RHIC (STAR) experiment

are used to study the production of electrons from open heavy flavor hadron decays at low transverse momentum (p_T) in $p+p$ collisions and at high p_T in $Au+Au$ collisions at $\sqrt{s_{NN}} = 200$ GeV. The experimental data used for these analyses are from the minimum bias $p+p$ collisions and the high-tower triggered $Au+Au$ collisions collected by STAR in years 2012 and 2014, respectively. Electrons are identified using the Time Projection Chamber combined with the Time Of Flight detector at low p_T and with the Barrel Electromagnetic Calorimeter (and the Shower Maximum Detector in $Au+Au$ collisions) at high p_T . Meanwhile the photonic background electrons (gamma conversion, light neutral meson π^0 and η Dalitz decays) are statistically subtracted by reconstructing the invariant mass of tagged e^\pm and every other partner e^\mp . The efficiencies used in these two analyses are estimated from pure electron data sample and STAR Geant + Monte Carlo embedding data. Then, the p_T spectra of electrons from open heavy flavor hadron decays at low p_T in $p+p$ collisions and at high p_T for different centralities in $Au+Au$ collisions are obtained.

In $p+p$ collisions, the measured spectrum of electrons from open heavy flavor hadron decays is consistent with the calculation of pQCD at $p_T > 0.5$ GeV/ c . And the excess above the pQCD calculation at $p_T < 0.5$ GeV/ c can provide constraints for the future theoretical model development. Moreover, this measurement also provides a high-precision reference for the measurements of nuclear modification factors in $Au+Au$ collisions. This is the first time that STAR extends the measurement of electrons from open heavy flavor hadron decays to the low p_T region.

In $Au+Au$ collisions, the more precise measurements of the invariant yields and the nuclear modification factors for electrons from open heavy flavor hadron decays are obtained compared to the published STAR measurements. For the invariant yield in central $Au+Au$ collisions, there is significant difference between $Au+Au$ measurement and the pQCD calculation scaled by the number of nucleon-nucleon collisions (N_{coll}), indicating existence of hot medium effects. From central to peripheral collisions, the difference is getting smaller, which is consistent with the expectation of less medium effects in peripheral collisions. And a strong suppression of the nuclear modification factor of electrons from open heavy flavor hadron decays at high p_T in central $Au+Au$ collisions is observed, which is consistent with the energy loss of the heavy quarks in the hot and dense matter. This measurement provides an important experimental reference for theoretical study about the energy loss mechanism of heavy flavor quarks through interactions with the QGP. Furthermore, the measurements of the nuclear modification factors are used in separate measurements of open charm and bottom hadron production

ABSTRACT

in $Au + Au$ collisions. This paves the way for testing the mass hierarchy of the parton energy loss in the QGP.

Key Words: Quantum ChromoDynamics; Quark Gluon Plasma; heavy quarks; semi-leptonic decayed electrons; transverse momentum spectra; nuclear modification factor; separation of charm and bottom quark

Contents

Chapter 1	Introductions	1
1.1	Standard Model and Quantum Chromodynamics	1
1.1.1	Standard Model	1
1.1.2	Quantum Chromodynamics	2
1.2	Relativistic Heavy Ion collisions	6
1.2.1	Transverse momentum spectrum, Energy loss and Jet quenching	7
1.2.2	Anisotropic flow	10
1.3	Open heavy flavor production in HIC	13
1.3.1	Heavy quarks as probes of sQGP	13
1.3.2	Experimental results	13
Chapter 2	Experimental Setup	19
2.1	The Relativistic Heavy Ion Collider	19
2.2	The Solenoidal Tracker at RHIC	20
2.2.1	The Time Projection Chamber	22
2.2.2	The Time Of Flight detector	25
2.2.3	The Barrel Electromagnetic Calorimeter	27
Chapter 3	Non-photonic Electron Analysis	31
3.1	Run 2012 200 GeV $p + p$ Collision Analysis	31
3.1.1	Analysis principle	31
3.1.2	Dataset and Event selection	32
3.1.3	Track selection and Electron identification	33
3.1.4	NPE raw yield extraction	33
3.1.5	Efficiency and Acceptance	39
3.1.6	Background subtraction	51
3.1.7	Trigger/Vertex bias correction	54
3.1.8	Bin shift correction	55
3.1.9	Systematic uncertainties	56
3.2	Run 2014 200 GeV $Au + Au$ Collision Analysis	60
3.2.1	Dataset and Event selection	60
3.2.2	Centrality definition	61
3.2.3	Track selection and Electron identification	63

CONTENTS

3.2.4	NPE raw yield extraction	63
3.2.5	Efficiency and Acceptance	67
3.2.6	Equivalent number of MB events	73
3.2.7	Combine NPE results	76
3.2.8	Background from J/Ψ decay	78
3.2.9	Systematic uncertainties	79
Chapter 4 Results and Discussion		81
4.1	Cross-section of NPE at low p_T in 200 GeV $p + p$ collisions	81
4.2	Invariant yields and R_{AA} of NPE at high p_T in 200 GeV $Au + Au$ collisions	81
4.3	R_{AA} at intermediate p_T in 200 GeV $Au + Au$ collisions	84
4.4	Summary	86
Chapter 5 Outlook		87
5.1	The Heavy Flavor Tracker	87
5.2	Invariant yields and R_{AA} of NPE in 200 GeV $Au + Au$ collisions	89
5.3	Bottom decayed electrons in 200 GeV $Au + Au$ collisions	90
Bibliography		94
Acknowledgements		103
Publications		105

List of Figures

1.1 Elementary particles in Standard Model.	1
1.2 First order Feynman diagrams showing screening and anti-screening between two color charges caused by vacuum polarization in QCD.	3
1.3 QCD effective coupling constant α_s as a function of the respective energy scale Q [1].	4
1.4 QCD phase diagram, include the first order (solid line) and crossover (dotted line) phase transition, critical point (circle), and evolution of several colliders (arrow). Figure was taken from [2].	5
1.5 Space-time evolution of a high-energy heavy-ion collisions. Figures were taken from [3, 4].	6
1.6 m_T spectra for light hadrons (π, K, p), Λ, Ξ and multi-strange hadrons (Φ, Ω) in 200 GeV central $Au + Au$ collisions, and charmed hadron (D^0) in 200 GeV minimum bias $Au + Au$ collisions, along with the Blast Wave fit results [5] shown in curves. Figure was taken from [6].	8
1.7 Left panel: $R_{AB}(p_T)$ as a function of p_T for minimum bias and central $d + Au$ collisions and central $Au + Au$ collisions. The bands show the normalization uncertainties. Right panel: Two particle azimuthal angle correlation distributions in $p + p$, central $d + Au$ and central $Au + Au$ collisions.	9
1.8 Diagrammatic sketch of the geometry of a heavy-ion collisions. The interaction region (almond-shape region) is horizontally cut by the reaction plane (x, z). Figure was taken from [7].	11

<p>1.9 Left panel: The v_2 of various hadrons as a function of p_T in 10-40% central 200 GeV $Au + Au$ collisions. Right panel: The v_2/n_q of various hadrons as a function of $(m_T - m_0)/n_q$ in 10-40% central 200 GeV $Au + Au$ collisions. Figures were taken from [8]</p>	12
<p>1.10 Leading Order diagrams of heavy quark production.</p>	13
<p>1.11 Heavy quark fragmentation to D^0 and two main D^0 decay channels.</p>	14
<p>1.12 Top-left panel: $c\bar{c}$ production cross section as inferred from D^0 and D production in 200 GeV $p + p$ collisions compared with FONLL calculations. Figure was taken from [9]. Top-right panel: D^0 invariant yields at mid-rapidity ($y < 1$) vs. transverse momentum for different centralities in 200 GeV $Au + Au$ collisions [10]. Bottom-left panel: $D^0 R_{AA}$ in 0-10% central 200 GeV $Au + Au$ collisions, comparison to ALICE D meson result, and hadron from ALICE and π^0 from PHENIX [10]. Bottom-right panel: Charm production cross sections at mid-rapidity per nucleon nucleon collisions as a function of N_{coll} [11].</p>	16
<p>1.13 Left panel: NPE invariant yields at mid-rapidity ($y < 0.7$) vs. transverse momentum for different centralities in 200 GeV $Au + Au$ collisions, along with NPE result in $p + p$ collisions and FONLL calculation. Right panel: NPE R_{AA} in 0-5% central 200 GeV $Au + Au$ collisions, comparison to NPE result in $d + Au$ collisions. Figures were taken from [12].</p>	17
<p>1.14 Left panel: Jet flavor tomography level crossing pattern of nuclear modification factors as a function of p_T at $y = 0$ for π, D, B, e fragmentation from quenched g, u, c, b jets in 0-5% central 200 GeV $Au + Au$ collisions at RHIC. Figure was taken from [13]. Right panel: Relative contribution from B mesons to open heavy flavor hadron decayed electrons in 200 GeV $p + p$ collisions. Figure was taken from [14].</p>	18
<p>2.1 Relativistic Heavy Ion Collider Facility.</p>	19

2.2 Overview of STAR detector.	21
2.3 Schematic of the TPC.	22
2.4 Anode pad plane of one full TPC sector.	23
2.5 dE/dx distribution as a function of momentum for different particles. The theoretical curves are calculated from Bichsel functions.	24
2.6 Two side views of a MRPC module.	26
2.7 Left panel: $1/\beta$ distribution as a function of momentum for different particles. Right panel: $n\sigma_e$ distribution as a function of momentum after $1/\beta$ cut.	27
2.8 Schematic view of BEMC module. Left panel: Side view of a calorimeter module showing the projective nature of the towers along the η direction. Right panel: Side view of a module showing the mechanical assembly including the compression components and the rail mounting system.	28
2.9 Schematic illustration of the double layer SMD.	29
3.1 Number of events with a series of selections.	32
3.2 Left panel: Correlations between V_z^{TPC} and V_z^{VPD} from MB triggered events. Right panel: Difference of V_z^{VPD} and V_z^{TPC}	33
3.3 Left panel: $n\sigma_e$ distribution in $1.10 < p_T < 1.20$ GeV/ c bin of pure electrons. The Gaussian function was used to fit this distribution. The pink lines show the $n\sigma_e$ cuts of inclusive electrons. Right panel: Mean and sigma from the fitting of $n\sigma_e$ distribution for pure electrons as a function of p_T . The polynomial3/polynomial2 + polynomial0 were performed to fit them.	35
3.4 Left panel: m^2 distribution as a function of p_T for hadrons. Right panel: m^2 distribution of hadrons. The red lines show m^2 cuts used to select pure hadron samples.	36

3.5 $n\sigma_e$ distributions of pure π , K and p in $1.10 < p_T < 1.20$ GeV/ c bin. The function 3.1 was used to fit these distributions.	36
3.6 $n\sigma_e$ distribution distribution and its fitting in $1.50 < p_T < 1.60$ GeV/ c bin for identified particles. The black dotted lines show the $n\sigma_e$ cut of inclusive electron.	37
3.7 Raw dN/dp_T and purity distributions as a function of p_T for inclusive electrons.	37
3.8 Left panel: Invariant $M_{e^+e^-}$ distribution in $1.50 < p_T < 1.60$ GeV/ c bin for photonic electrons. Right panel: Raw dN/dp_T distribution of photonic electrons.	39
3.9 Two-dimensional Gaussian distribution whose parameters from the covariance matrix of Gaussian fitting of pure electron $n\sigma_e$ distribution and $n\sigma_e$ cut efficiency distribution in $1.10 < p_T < 1.20$ GeV/ c bin.	41
3.10 $n\sigma_e$ cut efficiency as a function of p_T	41
3.11 $n\sigma_e$ cut efficiency as a function of Gp_T and tagged electron p_T for partner electron.	42
3.12 Tagged electron distribution without and with weight, which is from partner electron $n\sigma_e$ cut efficiency as a function of Gp_T	42
3.13 Number of electron tracks matched to TOF and number of electron tracks in TPC passed the track quality and acceptance cuts.	43
3.14 TOF matching efficiency as a function of p_T	44
3.15 Left panel: $1/\beta$ distribution in $1.10 < p_T < 1.20$ GeV/ c bin. The Gaussian function was used to fit this distribution. The pink lines show the $1/\beta$ cuts. Right panel: TOF EPID efficiency as a function of p_T	45

3.16 Number of electron tracks with BEMC EPID cut ($0.3 < p/E < 1.5$), number of electron tracks matched to BEMC, number of electron tracks in TPC passed the track quality and acceptance cuts.	46
3.17 BEMC matching and EPID efficiency as a function of p_T	46
3.18 Top-left panel: Invariant yield distributions of π^0 and η mesons. The Tsallis functions were used to fit those distributions. Top-right panel: dN/dy as a function of y for π^0 and η mesons. Bottom-left panel: Direct γ invariant yield distribution. The power-law was used to fit this distribution. Bottom-right panel: Inclusive γ p_T spectrum along with those from different sources.	47
3.19 Left panel: Relative contributions from gamma conversion, π^0 and η Dalitz decays to photonic electrons as a function of p_T . Right panel: Combined reconstruction efficiency as a function of p_T , along with the individual efficiencies from γ conversion, π^0 and η Dalitz decays.	49
3.20 Left panel: TPC tracking efficiency as a function of p_T without p_T smearing effect. Right panel: NPE p_T spectrum. A function $p_0 * x * (e^{p_1*x} + x/p_2)^{p_3}$ was used to fit this distribution.	49
3.21 Left panel: TPC tracking efficiency as a function of p_T with p_T smearing effect. Right panel: All efficiencies as a function of p_T	49
3.22 Invariant yield distributions of inclusive and photonic electrons.	50
3.23 Invariant yield distributions of $\omega \rightarrow e$, $\phi \rightarrow e$ and $c \rightarrow e$. Right panel: Ratios of $\omega \rightarrow e$ and $\phi \rightarrow e$ than $c \rightarrow e$ as a function of p_T	51
3.24 Left panel: Invariant yields of K^+ , K^- and K_L^0 from MB 200 GeV $p+p$ collisions based on PYTHIA simulation, along with STAR published results of K^+ and K^- . Right panel: Invariant yields for K_{e3}^+ and K_{e3}^- from PYTHIA simulation after K^+ and K^- yield correction, along with combined one.	52

3.25	Left panel: Reconstruction efficiency of K_{e3}^{\pm} as a function of p_T , along with that of K_{e3}^+ and K_{e3}^- . Right panel: Invariant yield for K_{e3}^{\pm} from PYTHIA simulation with the K_{e3}^{\pm} reconstruction efficiency applied.	53
3.26	Left panel: Reconstruction efficiency of K_{e3}^{\pm} as a function of p_T in $0 < R_{xy} < 10$ cm bin. A function $p_0/(e - (p_T - p_1)/p_2 + 1) + p_3$ was used to fit this distribution. Right panel: Reconstruction efficiency of K_{e3}^{\pm} as a function of p_T and R_{xy}	53
3.27	Left panel: Invariant yield of K_{e3} as a function of p_T , along with that of K_{e3}^{\pm} and K_{e3}^0 . Right panel: Ratio of K_{e3} yield to NPE as a function of p_T	54
3.28	Left panel: NPE p_T spectrum without bin shift correction, along with two different function fittings. Right panel: Bin shift correction factors as a function of p_T from two different function fittings.	55
3.29	$nHitsFit$, $nHitsDedx$ and $Gdca$ for NPE, Gp_T and $nHitsFit$ for partner electron of photonic electrons, and M_{e+e-} for photonic electron distributions in $0.2 < p_T < 0.25$ GeV/c bin.	57
3.30	Relative uncertainties of $nHitsFit$, $nHitsDedx$ and $Gdca$ for NPE, Gp_T and $nHitsFit$ for partner electron of photonic electrons, and M_{e+e-} for photonic electrons as a function of p_T	58
3.31	Systematic uncertainties of purity, tagged electron $n\sigma_e$ cut efficiency and partner electron $n\sigma_e$ cut efficiency as a function of p_T	58
3.32	Systematic uncertainties of TOF EPID efficiency, BEMC matching and EPID efficiencies as a function of p_T	59
3.33	Systematic uncertainties of photonic electron reconstruction efficiency as a function of p_T	59
3.34	Systematic uncertainties of K_{e3} and hadron decayed electron contribution as a function of p_T	60

3.35	Total systematic uncertainties as a function of p_T .	60
3.36	Left panel: Correlation between V_z^{TPC} and V_z^{VPD} from HT1 events of lowmid-luminosity. Right panel: Difference of V_z^{VPD} and V_z^{TPC} from HT1 events of lowmid-luminosity.	62
3.37	Left panel: $n\sigma_e$ distribution in $2.50 < p_T < 3.00$ GeV/ c bin of pure electrons at 0-80% centrality for HT1 events of lowmid-luminosity. The Gaussian function was used to fit this distribution. The pink lines show the $n\sigma_e$ cut of inclusive electron. Middle panel: Mean and sigma from the fittings of $n\sigma_e$ distributions for pure electrons as a function of p_T at 0-80% centrality in different triggers of lowmid-luminosity. The polynomial0 were performed to fit them. Right panel: Means from Bischel function as a function of p_T for pure hadrons at 0-80% centrality of lowmid-luminosity.	64
3.38	$n\sigma_e$ distribution and its fitting result of multi-Gaussian function in $2.50 < p_T < 3.00$ GeV/ c bin for identified particles for HT1 events of lowmid-luminosity. The pink dotted lines show the $n\sigma_e$ cuts of inclusive electrons.	64
3.39	Raw dN/dp_T distributions of inclusive electrons in different centralities, triggers and luminosities.	65
3.40	Purity distributions of inclusive electrons in different centralities, triggers and luminosities.	65
3.41	$M_{e^+e^-}$ distribution at $2.50 < p_T < 3.00$ GeV/ c bin in 0-80% centrality for HT1 events of lowmid-luminosity.	66
3.42	Raw dN/dp_T distributions of photonic electrons in different centralities, triggers and luminosities.	67
3.43	$n\sigma_e$ cut efficiencies as a function of p_T in different centralities, triggers and luminosities.	67

3.44 BEMC matching efficiencies as a function of p_T in different centralities, triggers and luminosities.	68
3.45 TPC tracking efficiencies as a function of p_T in different centralities, triggers and luminosities.	68
3.46 BEMC (SMD) EPID efficiencies as a function of p_T in different centralities, triggers and luminosities.	69
3.47 Trigger efficiencies as a function of p_T in different centralities, triggers and luminosities.	69
3.48 Top-left panel: π^0 invariant yield distributions in different centralities. The functions of a power-law with an exponential were used to fit invariant yield distributions. Top-right panel: $dN/dy/ < 0.5N_{part} >$ as a function of N_{part} for π^0 . Bottom-left panel: η invariant yield distributions in different centralities from m_T scaling of the π^0 p_T -shape, along with that in 0-92% $Au + Au$ collisions from PHENIX published one. Bottom-right panel: Direct γ invariant yield distributions in different centralities in $Au + Au$ collisions along with that in $p + p$ collisions. The power-law was used to fit invariant yield in $p + p$ collisions.	70
3.49 Inclusive γ p_T spectra in different centralities, along with those from different sources.	71
3.50 Left panel: Relative contribution from γ conversion, π^0 and η Dalitz decays to phonic electrons as a function of p_T at 0-80% centrality in HT1 events of lowmid-luminosity. Right panel: Combined reconstruction efficiency as a function of p_T along with the individual efficiencies from γ conversion, π^0 and η Dalitz decays at 0-80% centrality in HT1 events of lowmid-luminosity.	72
3.51 Combined reconstruction efficiencies as a function of p_T in different centralities, triggers and luminosities.	72

3.52	Efficiencies as a function of p_T in different centralities, triggers and luminosities.	74
3.53	Equivalent number of MB events in different centralities, triggers and luminosities.	75
3.54	Invariant yields of inclusive and photonic electrons in different centralities, triggers and luminosities.	75
3.55	Invariant yields of NPE in different centralities, triggers and luminosities.	76
3.56	Combined invariant yields of NPE in different centralities.	77
3.57	Left panel: STAR preliminary J/Ψ invariant yields as a function of p_T in different centralities. Right panel: $dN/dy/ < 0.5N_{part} >$ as a function of N_{part} for J/Ψ	77
3.58	Left panel: J/Ψ invariant yields as a function of p_T in different centralities. Right panel: J/Ψ dN/dy as a function of y	78
3.59	Left panel: $J/\Psi \rightarrow e^+e^-$ invariant yields as a function of p_T in different centralities. Right panel: Ratios of $J/\Psi \rightarrow e^+e^-$ to NPE as a function of p_T in different centralities.	78
3.60	Left panel: NPE p_T spectra without bin shift correction in different centralities, along with two different function fittings. Right panel: Bin shift correction factors as a function of p_T from two different function fittings in different centralities.	79
3.61	Left panel: Systematic uncertainty of trigger efficiency as a function of p_T in 0-80% centrality. Right panel: Systematic uncertainty of J/Ψ decayed electron contribution as a function of p_T in 0-80% centrality.	80
3.62	Total systematic uncertainties as a function of p_T in different centralities. .	80

4.1 Top-left panel: Ratio of signal to background as a function of p_T . Top-right panel: Cross-section of NPE as a function of p_T . Bottom panel: Ratio of data to the pQCD calculation as a function of p_T	82
4.2 NPE invariant yields as a function of p_T in different centralities for Au+Au collisions at $\sqrt{s_{NN}} = 200$ GeV, and scaled STAR preliminary p+p [15]. Error bars are statistical errors, and boxes are point-by-point systematic uncertainties.	82
4.3 Signal to background ratios as a function of p_T in different centralities in Run14 and Run10 [16] for Au+Au collisions at $\sqrt{s_{NN}} = 200$ GeV.	83
4.4 NPE R_{AA} as a function of p_T in different centralities of Au+Au collisions at $\sqrt{s_{NN}} = 200$ GeV. Bars and Error boxes are statistical and systematic errors, respectively. Bands around each data point depict the uncertainties from the p+p baseline measurement.	83
4.5 NPE R_{AA} as a function of p_T for different centralities of Au+Au collisions at $\sqrt{s_{NN}} = 200$ GeV. Bars and Error boxes are statistical and systematic errors, respectively. Bands around each data point depict the uncertainties from the p+p baseline measurement.	85
5.1 Schematic view of the different layers of the HFT.	88
5.2 Track pointing resolution in the transverse plane as a function of particle momentum.	89
5.3 <i>Top</i> : DCA_{XY} distribution for inclusive electrons with a template fit including $B \rightarrow e$, $D \rightarrow e$, and background electrons. <i>Bottom</i> : Ratio of data to the fitted template.	90
5.4 Fraction of $B \rightarrow e$ to open heavy flavor hadron decayed electrons in 200 GeV $p + p$ and $Au + Au$ collisions.	91
5.5 $R_{AA}^{B \rightarrow e}$ and $R_{AA}^{D \rightarrow e}$ as a function of p_T	92

List of Tables

3.1 Cuts of selecting pure electron sample for tagged electron $n\sigma_e$ cut efficiency calculation.	40
3.2 Event selection criteria	61
3.3 Number of events after event selections.	61
3.4 Centrality definition, N_{coll} and N_{part}	62
3.5 Cuts of track candidate selections.	63
3.6 Cuts of the partner electrons and e^+e^- pairs for photonic electrons.	66
3.7 dN/dy of π^0 , R_π and dN/dy of η at mid-rapidity in different centralities.	71
3.8 dN/dy of J/Ψ at mid-rapidity in different centralities	78

Chapter 1 Introductions

1.1 Standard Model and Quantum Chromodynamics

In the 20th century, physics expanded the human understanding of natural phenomena along two main lines. The first line was to search for the great Cosmos by the use of various telescopes. The second one made use of various kinds of microscopy equipments to explore the Micro Cosmos: atoms and subatoms.

1.1.1. Standard Model

The accelerator particle microprobe as one kind of microscopy equipments was utilized to study the structure of nuclei and particles ($10^{-14} \sim 10^{-17} m$) and found the hundreds of microscopic particles. Most of them are not elementary particles, but they are formed by elementary particles through interactions. There are 6 quarks (*up*, *down* [17], *charm* [18], *strange* [19], *top* [20] and *bottom* [21]), 6 leptons (*e*, μ , τ and their corresponding neutrinos), 4 gauge vector bosons (*g*, γ , *Z* and *W*) and 1 *H* boson according to the Standard Model (SM) of particle physics [1], which is the theory classifying all known elementary particles and describing three of the four known fundamental interactions including the electromagnetic, weak, and strong interactions, however not including the gravitational interaction in the universe. The quarks and leptons are fermions. And the

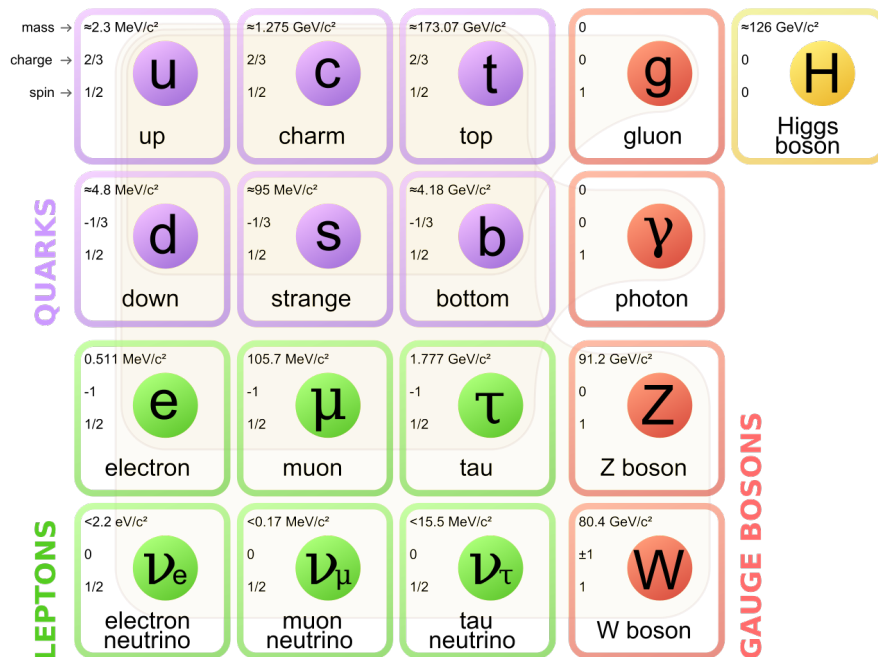


Fig. 1.1 Elementary particles in Standard Model.

quarks and leptons have the corresponding anti-particles. The positive and negative particles have the same mass, spin and isospin, and opposite charge, baryon number, lepton number, etc. The elementary particles in SM are shown in Fig. 1.1, along with their detailed properties such as mass, charge and spin.

The hadrons, which are composed of quarks, can be classified as mesons (1 quark and 1 anti-quark) and baryons (3 quarks). Since quarks have electric, weak and color charges, hadrons can involve in the electroweak and strong interactions. The leptons as elementary particles can exist freely. The electroneutral neutrinos carry weak charge, thus they can only take part in the weak interaction. The charged leptons have electric and weak charges and thereby they participate in the electromagnetic and weak interactions. The gauge bosons, so-called force carriers, are the propagators of the interactions. The force carriers of the electromagnetic, weak, and strong interactions are photon, gluon and Z^0/W^\pm , respectively. The Higgs boson [22] discovered at LHC in 2012 [23] is a scalar one and its participation make the electro-weak gauge field boson to gain mass.

1.1.2. Quantum Chromodynamics

Similar with the invariance of the charge U(1) local gauge transformation introduces the electromagnetic field to establish the Quantum ElectroDynamics (QED), the invariance of color SU(3) local gauge transformation introduces the color gluon field to develop a dynamic theory of strong interaction: Quantum ChromoDynamics (QCD) [24]. The SU(3) local gauge invariance requires that the mass of its gauge boson must be zero because the gauge boson with mass can destroy the Lagrangian invariance of the gauge field. Furthermore, the interactions between the quarks with color charges must be achieved through gluons with color charges.

1. Asymptotic freedom and Color confinement

In the case of QCD, two quarks with color charges exchange a virtual gluon. This virtual gluon excites the virtual $q\bar{q}$ pair in a vacuum, which is a Dirac sea (an infinite sea of particles and anti-particles with negative energy) in quantum field theory. As the same case of QED, the $q\bar{q}$ pair between two color charges plays a role of color screening, shown in the left panel of Fig. 1.2. The important difference between QCD and QED is that the QCD gauge boson is the gluon with color charge, which could have self-interaction through absorbing and scattering gluon. This results the “cloud”

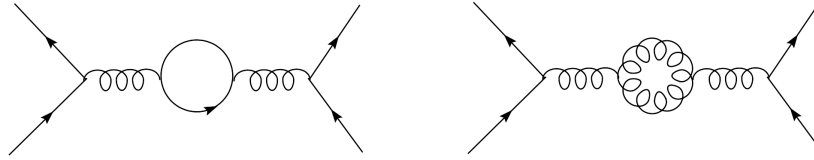


Fig. 1.2 First order Feynman diagrams showing screening and anti-screening between two color charges caused by vacuum polarization in QCD.

of color gluon, excited between the two color charges with interactions, can have an anti-screening effect on these two color charges (shown in the right panel of Fig. 1.2): at high momentum transfer or equivalently at short distance between the two color charges, the interactions of them become weak, so-called *asymptotic freedom* [25–28]; on the contrary, the interactions become strong so that these two color charges are unable to be separated, so-called *color confinement*.

According to Feynman rule, the circle diagrams of Fig. 1.2 are calculated and then renormalized, then the effective QCD coupling constant α_s [29] can be expressed as:

$$\alpha_s(Q^2) = \frac{1}{\beta_0 \ln(Q^2/\Lambda_{QCD}^2)} \quad (1.1)$$

where β_0 is the first coefficient of the β -function (renormalization neglects the higher orders), and Λ_{QCD} is one of the important QCD parameters. The α_s has to be determined from experiment. The world average α_s at common energy scale $Q = M_z$ is $\alpha_s(M_z) = 0.1184 \pm 0.0007$, and the QCD scale $\Lambda_{QCD} \sim 200$ MeV. Fig. 1.3 shows the coupling constant α_s at different energy scale. When $\beta_0 > 0$, $\alpha_s \rightarrow 0$ as $Q \rightarrow \infty$ (at short distance or with high momentum transfer), the strong force of the gluon-gluon self-coupling becomes smaller, which shows asymptotic freedom property. In this case, QCD Lagrangian can be calculated perturbatively (pQCD). In contrast, at large distance or low momentum transfer, the coupling constant becomes large and the QCD equation cannot be solved. The QCD kinematic equation is solved by other effective methods such as Lattice QCD [30], which is one of the theories that describes the interactions between quarks and gluons in non-perturbative region.

2. Deconfinement and Quark-gluon plasma

Due to color confinement, the quarks and gluons are confined into hadrons at normal conditions, no free quarks and/or colors can be observed. When two quarks are separated, the gluon field forms a string of color charge to bring the quarks together thereby prevents these two quarks separation. If two quarks have high enough energy and be-

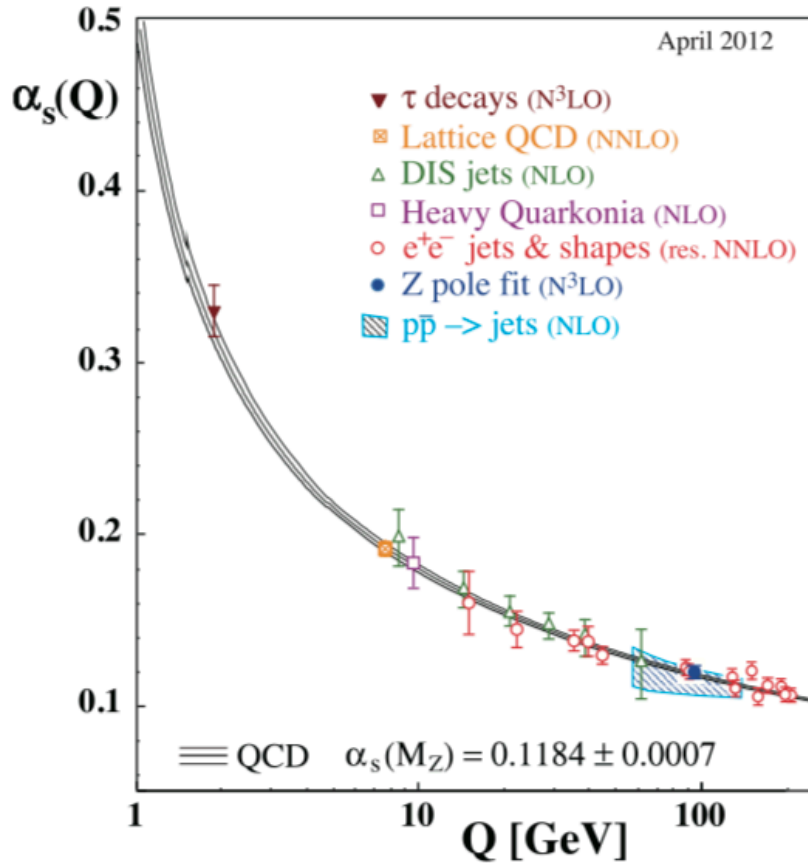


Fig. 1.3 QCD effective coupling constant α_s as a function of the respective energy scale Q [1].

come separated, it is more energetically favorable for new quark and antiquark pair is created from the vacuum to prevent the two quarks to separate further. Thus the production of high-energy quarks yields a color-neutral cluster-like, *jet*. The process is called hadronization.

But at extremely high temperature and energy density, the strong force among quarks and gluons may be greatly reduced. Quarks (anti-quarks) and gluons are no longer confined in hadrons, but become common free-colored quarks and gluons. This new state of matter is called Quark-Gluon Plasma (QGP) [31–34]. While this process from confinement to “free” is called deconfinement. Lattice QCD calculation predicts a phase transition from hadronic gas to QGP at an extremely high temperature $T_C \sim 170 \text{ MeV}$ and/or high energy density $\epsilon_C \sim 1 \text{ GeV}/f\text{m}^3$ [35, 36]. The study of this phase transition is one of the most important topics in the field of heavy ion collision physics. Fig. 1.4 shows the QCD phase diagram in the baryon chemical potential (μ_B), temperature (T) plane. A boundary divides the matter in the phase diagram into two parts: the hadronic gas dominated by the hadron degree of freedom at low temperature and chemical potential, where ordinary matter in nature could only exist, and the quark

gluon plasma dominated by the quark-gluon degree of freedom at high temperature and chemical potential. This boundary at high μ_B is a first-order phase transition line (solid line) [37, 38]. According to Lattice QCD calculation, when μ_B is very close to 0, the phase transition will be a rapid crossover (dotted line) to the hadronic phase for $T > T_c$. The transition to QGP changes from a crossover to a first order results in the existence of a critical point (circle) in the QCD phase diagram. Calculation expects that the critical point exists in the range $250 < \mu_B < 450$ MeV [39, 40].

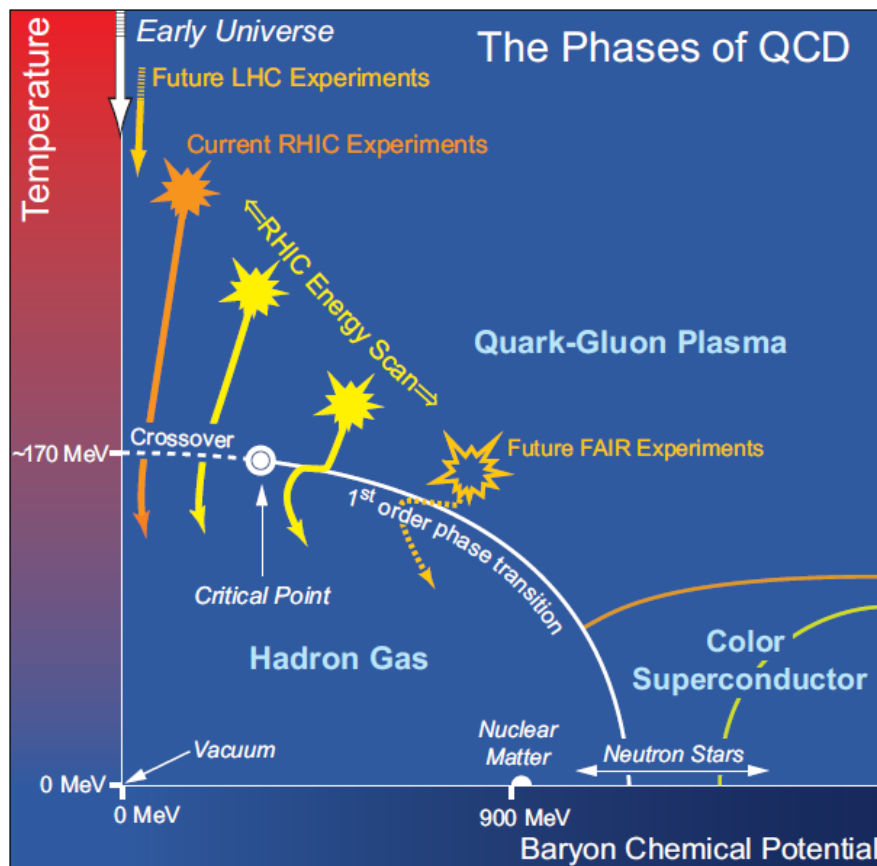


Fig. 1.4 QCD phase diagram, include the first order (solid line) and crossover (dotted line) phase transition, critical point (circle), and evolution of several colliders (arrow). Figure was taken from [2].

To explore the QCD phase diagram and to study QGP matter, the extreme environment (high temperature and density), at which the deconfined phase could be possible and the phase transition may occur as the system evolution, is achieved through accelerating and colliding heavy ions in laboratory.

1.2 Relativistic Heavy Ion collisions

The Relativistic Heavy Ion Collider (RHIC) [41] located in Brookhaven National Laboratory (BNL), New York (NY) was designed to mainly study the formation and properties of the hot, dense medium QGP via accelerating and colliding heavy ions to reach the extreme temperature and density conditions. And the RHIC Energy Scan is used to search for the critical point. Detailed information about RHIC can be found in Chapter 2.

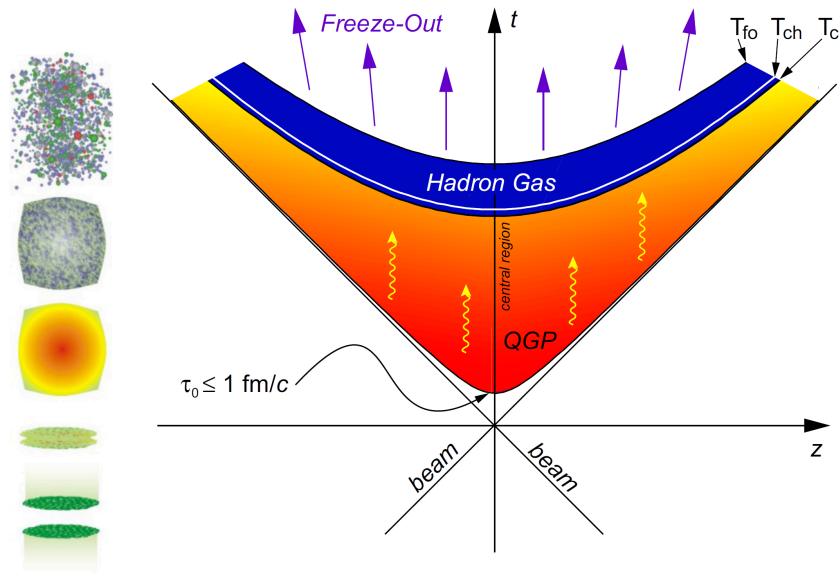


Fig. 1.5 Space-time evolution of a high-energy heavy-ion collisions. Figures were taken from [3, 4].

Fig. 1.5 depicts the process of space-time evolution and the material forms at each stage in Heavy-Ion Collisions (HIC). The two extremely relativistic heavy nuclei approach and collide. Most of the nucleons are blocked and then continue to flow. A large amount of energy is instantaneously deposited in a small volume that is larger than the nucleon and less than the heavy nucleus. A rapid heating ($T > T_c$) initial state with the energy density up to $700 \text{ MeV} \cdot \text{fm}^{-3}$, the low baryon density and the high gluon density (50 times than that in common cold nuclear matter) is produced ($t < \sim 1 \text{ fm}/c$). As the temperature of system rapidly rises, the partons (gluons, quarks and anti-quarks) undergo intense high-transverse momentum (p_T) collisions and heat exchanges. The system (local) quickly ($t \sim 1 \text{ fm}/c$) enters thermal equilibrium (thermalization). This stage is called pre-equilibrium, where high p_T jets, heavy quark pairs, direct photons, etc. are created due to high momentum transfers via the primary hard scatterings. Subsequently the system expands and forms a new matter state QGP with a longer stable

time ($t \sim (1 \sim 5 \text{ fm}/c)$). When the phase boundary reaches as the system continues to expand and cools down ($T < T_c$), the system begins to undergo hadronization through various channels. At this time, the system is a mixture of partons and hadrons and the types of hadrons transform into each other through inelastic collisions between hadrons. In the process from the formation of QGP to hadronization, the system can be described by the relativistic fluid mechanics. When the system reaches a certain temperature T_{ch} , the inelastic collisions tend to stop and the ratios of the final state hadrons are basically fixed [42]. By now the system reaches a chemical equilibrium. The T_{ch} is called chemical equilibrium temperature or chemical freeze-out temperature ($t \sim 10 \text{ fm}/c$). The system temperature decreases, hadrons exchange kinetic energy only through the elastic collisions. When the temperature drops to T_{fo} (kinetic freeze-out temperature), elastic collisions between hadrons also completely stop and the momenta of hadrons become fixed [5]. And then the hadrons freeze out from the system and enter spectrometer detector to be measured. Experimentally, the properties of QGP are studied through the the analysis of final state hadrons.

The geometry of high-energy HIC has a very important influence on collision dynamics. Since the de Broglie wavelength of a nucleon is much smaller than the size of the nucleus in HIC, the collision parameter b is used to describe the nucleus-nucleus collisions. According to the comparison between b and radius of the nucleus, there are three collision types: long distance collisions ($b > 2R_A$), peripheral collisions ($b < 2R_A$) and central collisions ($b \approx 0$). The size of the impact parameter, b , can be given by the the number of nucleon-nucleon collisions (N_{coll}) or the number of participating nucleons (N_{part}) (two body collisions) calculated by the Glauber model [43].

The most remarkable discoveries of RHIC are that the mass dependence of the p_T spectra of the particles and the elliptic flow at low p_T region, in which most of particles are dominantly produced, are successfully explained by using the hydrodynamic models [44, 45] of the relativistic fluid. The elliptic flow observations of hadrons can reflect the important information about QGP. At the same time, by measuring the nuclear modification factors of the high p_T hadrons, the properties of QGP can be given.

1.2.1. Transverse momentum spectrum, Energy loss and Jet quenching

The final state hadron p_T spectra in $p+p$, $p+A$ and $A+A$ collisions have been measured. The p_T spectrum is usually described by the invariant cross section. It has been found

that the single particle spectrum in the $p_T < 2$ GeV/ c range can be well described by the exponential distribution of $m_T/(m_T - m)$ ($m_T \equiv \sqrt{p_T^2 + m^2}$ and m is the particle mass).

$$E \frac{d^3\sigma}{d^3p} = \frac{1}{2\pi m_T} \frac{d^2\sigma}{dm_T dp_y} \approx \exp(-m_T/T). \quad (1.2)$$

This phenomenon is called the $m_T/(m_T - m)$ -scaling [46]. In $p+p$ and $p+A$ collisions,

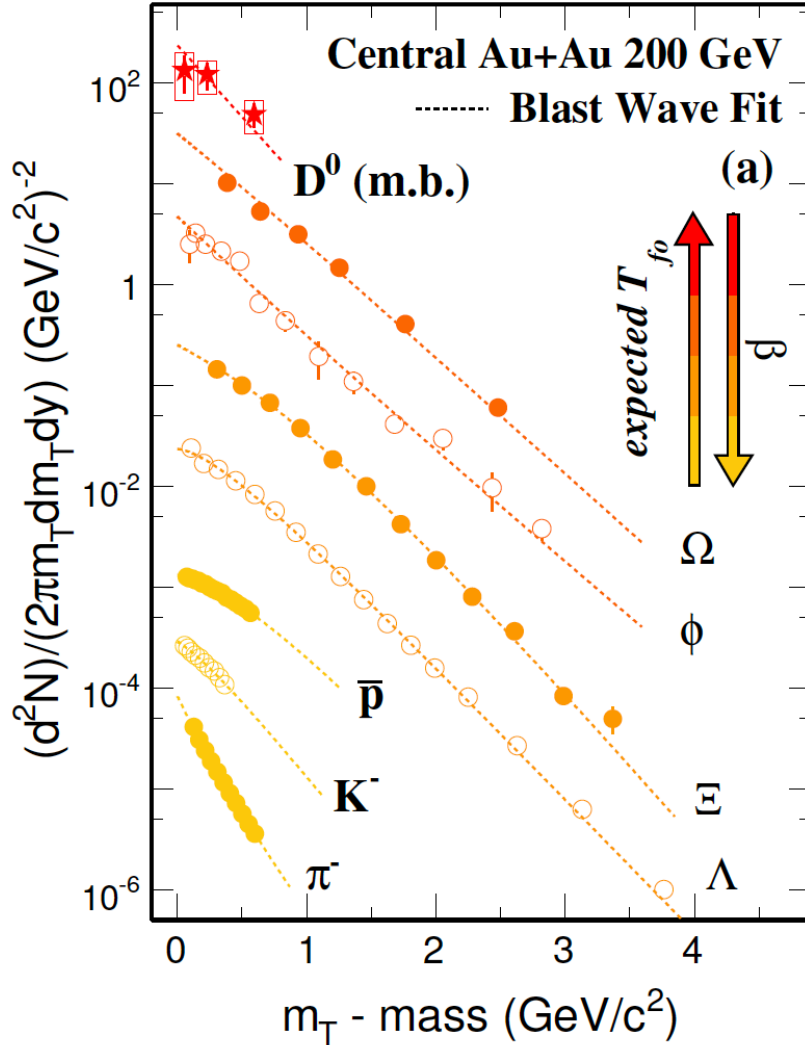


Fig. 1.6 m_T spectra for light hadrons (π , K , p), Λ , Ξ and multi-strange hadrons (Φ , Ω) in 200 GeV central $Au + Au$ collisions, and charmed hadron (D^0) in 200 GeV minimum bias $Au + Au$ collisions, along with the Blast Wave fit results [5] shown in curves. Figure was taken from [6].

the temperature parameter T of the different kinds of particles (such as π , K , p) is equal ($T \sim 150$ MeV). There is a collective radial flow, which is caused by the interactions between hadrons and the system expansion, in $A + A$ collisions compared in $p + p$ and $p + A$ collisions. Superimposing on the thermal emission of the hadrons, the collective

radial flow produces a correction term that depends on hadron mass for the transverse mass distribution of the hadrons in $A + A$ collisions. The transverse mass distribution becomes:

$$\frac{dN}{m_T dm_T} \sim m_T \int_0^{R_f} r dr \tau_f K_1 \left(\frac{m_T \cosh \alpha}{T} \right) I_0 \left(\frac{p_T \sinh \alpha}{T} \right), \quad (1.3)$$

where K_n (I_n) is Bessel function of the second (first) kind and α is transverse rapidity. Comparing this model with the measured spectra of the various particles, many detailed information about the thermalization mechanism, the freeze-out temperature T and radial velocity v_r of the nucleus-nucleus collisions are obtained. In particular, the radial velocity information will help us have a profound understanding of the origin of hydrodynamic mechanics. Fig. 1.6 shows the m_T spectra for light hadrons (π , K , p), Λ , Ξ and multi-strange hadrons (Φ , Ω) in 200 GeV central $Au + Au$ collisions [47–50], and charmed hadron (D^0) [51] in 200 GeV minimum bias $Au + Au$ collisions.

The high p_T hadron yields will be suppressed due to energy loss through interactions with the QCD medium created in HIC. So the measurements of the suppression of high p_T hadron yields can provide the properties of the medium. Experimentally, the nuclear modification factor R_{AB} is widely used to quantify the suppression. It is obtained by taking the ratio of the hadron yield in $A + B$ collisions to that in $p + p$ collisions normalized by N_{coll} [52, 53]:

$$R_{AB} = \frac{1}{N_{coll}} \frac{d^2 N_{AB}/dp_T/dy}{d^2 N_{pp}/dp_T/dy}. \quad (1.4)$$

The left panel of Fig. 1.7 shows the RHIC-STAR measured $R_{AB}(p_T)$ as a function of p_T

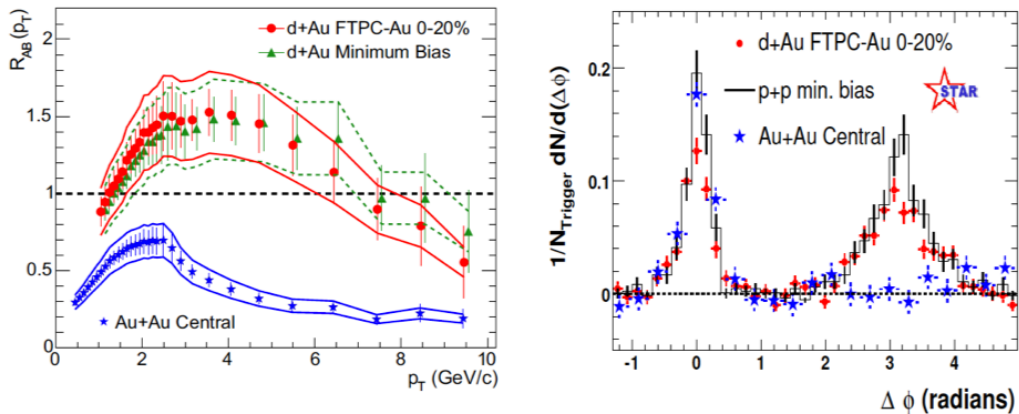


Fig. 1.7 Left panel: $R_{AB}(p_T)$ as a function of p_T for minimum bias and central $d + Au$ collisions and central $Au + Au$ collisions. The bands show the normalization uncertainties. Right panel: Two particle azimuthal angle correlation distributions in $p + p$, central $d + Au$ and central $Au + Au$ collisions.

for minimum bias and central $d + Au$ collisions and central $Au + Au$ collisions [54]. As we can see, the suppression of high p_T hadron yields and enhancement of intermediate p_T hadron yields are observed in $Au + Au$ collisions and $d + Au$ collisions, respectively. The production of particles depends on the hard processes at high p_T region. They are expected to scale with N_{coll} , and thus the R_{AA} should be equal to 1 as the p_T increases if there is the absence of nuclear effects such as shadowing [55–58], the Cronin effect [59–62] etc. For $d + Au$ collisions, the random walk of the intermediate p_T partons enhances the production of intermediate p_T hadrons due to the multiple initial elastic collisions compared in $p + p$ collisions. This effect is called Cronin effect. For $Au + Au$ collisions, the suppression of high p_T hadron yields is as an evidence for the energy loss of the energetic partons through their interactions with the medium.

On the other hand, energy loss in the medium also can be studied by using the di-hadron azimuthal angle correlations. Partons fragment into the cone shaped hadron-jet along the initial direction of motion. For hadrons in the jet, the hadrons with the highest p_T maybe follow the original parton motion direction. Assuming that the high p_T hadrons represents the hard-scattered partons, an angular correlation of hadrons with parton direction can be defined. The right panel of Fig. 1.7 shows the two particle azimuthal angle correlation distribution in central $Au + Au$ collisions comparing those in $p + p$ and $d + Au$ collisions [54]. In addition, the angle correlation have subtracted the contribution from anisotropic flow. The enhanced correlations at near-side ($\Delta\phi \sim 0$) are observed in $d + Au$ and $Au + Au$ collisions and show the similar distribution in $p + p$ collisions. However, the correlation on away-side ($\Delta\phi \sim \pi$) in $Au + Au$ collisions shows the complete disappearance and the typical two jets are formed in $p + p$ and $p + Au$ collisions. These results indicate that the disappearance of back-to-back jet is caused by its energy loss through the interactions with hot-dense matter created in central $Au + Au$ collision. Because the same phenomenon should be observed in $p + Au$ collisions, if it does not depend on the matter produced in $Au + Au$ collision but the initial state effect.

1.2.2. Anisotropic flow

The anisotropy of the spatial azimuth of the final state momentum is sensitive to the early evolution of the system. In non-central heavy-ion collisions, the shape of the overlapping regions of collision nuclei is amygdaloid (shown in Fig. 1.8), and the particles are mainly produced and emitted in this region, which corresponds to the anisotropy of spatial coordinates. Through the re-scattering of each component, the anisotropy of coordinate space is transformed into the one of momentum space. The system expands

rapidly after the initial interactions, and the anisotropy of the coordinate space is greatest in the initial stage of the collision. But as the system expands, the anisotropy gradually disappears. Therefore, this anisotropy can reflect the information of the early stage of collisions.

The initial space anisotropy can be roughly characterized by the initial almond-like geometric eccentricity:

$$\epsilon = \frac{\langle y^2 - x^2 \rangle}{\langle y^2 + x^2 \rangle}, \quad (1.5)$$

where (x, y) is the coordinate in the plane orthogonal to the beam axis z , and (x, z) is reaction plane.

Experimentally, the final particle azimuth angle distribution in momentum space can be described by the Fourier expansion of the reaction plane:

$$E \frac{d^3 N}{d^3 p} = \frac{d^2 N}{2\pi p_T dp_T dy} \left(1 + \sum_{n=1}^{\infty} 2v_n \cos[n(\phi - \Psi_r)] \right), \quad (1.6)$$

where ϕ is the azimuth angle of particle, and Ψ_r is the azimuth angle of reaction plane.

The Fourier coefficients, which represent anisotropy parameters, can be extracted as:

$$v_n = \langle \cos[n(\phi - \Psi_r)] \rangle, \quad (1.7)$$

where the first two coefficients are the directed flow $v_1 = \langle \cos\phi \rangle$ and elliptic flow $v_2 = \langle \cos 2\phi \rangle$.

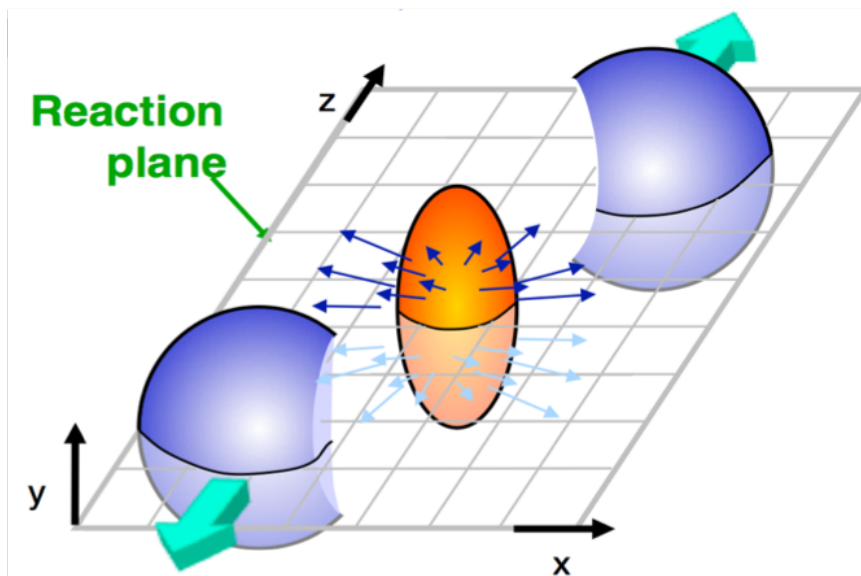


Fig. 1.8 Diagrammatic sketch of the geometry of a heavy-ion collisions. The interaction region (almond-shape region) is horizontally cut by the reaction plane (x, z) . Figure was taken from [7]

The left panel of Fig. 1.9 shows the measured v_2 for various hadrons in 10-40% $Au + Au$ collisions. In low p_T region, the elliptic flow v_2 increases with the p_T and the obvious particle mass ordering is observed, which shows hydrodynamical behavior [44, 45]. The lighter particles have the larger elliptic flow. In high p_T region, the elliptic flow shows the saturation effect, which suggests that presence of hard scattering region. The right panel of Fig. 1.9 shows v_2/n_q as a function of scaled transverse kinetic energy $(m_T - m_0)/n_q$ (n_q is the number of constituent quarks in the hadron). The elliptic flow of hadrons scaled the number of constituent quarks falls to the same curve, which may reflect the elliptic flow of the partons. This feature is called the Number-of-quark (NQ) scaling and the natural result of the quark coalescence/combination model [63, 64], in which mesons and baryons are hadronized by coalescing two and three co-moving quarks, respectively.

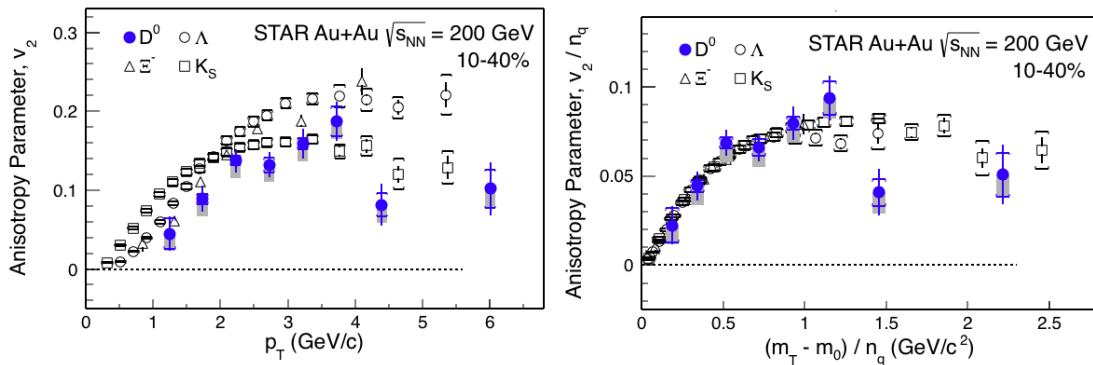


Fig. 1.9 Left panel: The v_2 of various hadrons as a function of p_T in 10-40% central 200 GeV $Au + Au$ collisions. Right panel: The v_2/n_q of various hadrons as a function of $(m_T - m_0)/n_q$ in 10-40% central 200 GeV $Au + Au$ collisions. Figures were taken from [8]

From the above elliptical flow experimental result, we have realized that the matter created in RHIC HIC is the collective flow which is very close to the ideal fluid. This collective flow is on the parton-level. Furthermore, the phenomenon of jet quenching predicates that the corresponding matter is very hot-dense. A series of experimental results can't be explained by the model of hadrons. It signifies that RHIC has created a strongly coupled quark-gluon plasma (sQGP), or which is vividly referred to as “quark soup”.

1.3 Open heavy flavor production in HIC

1.3.1. Heavy quarks as probes of sQGP

Heavy quarks, that are, charm and bottom. Their masses, $m_c \approx 1.3 \text{ GeV}/c^2$ and $m_b \approx 4.2 \text{ GeV}/c^2$ [1], are larger than $\Lambda_{QCD} \sim 200 \text{ MeV}$ and $T_{QGP} > 2T_c (\sim 170 \text{ MeV})$. Due to $m_{c,b} \gg \Lambda_{QCD}$, a large amount of energy and momentum transfer are needed to produce heavy quarks [65]. Such high energy densities are primarily found in hard scatterings of partons in the nucleons of the heavy ions or during the early phase of the QGP at the early stage of HIC. Meanwhile because of $m_{c,b} \gg T_{QGP}$, heavy quarks are produced before the creation of QGP and their production during the QGP phase is turned out to be insignificant at RHIC energies [66, 67]. Therefore, heavy quarks are dominantly produced in hard scatterings before the creation of QGP at early stages of high-energy HIC due to their large masses. These heavy quarks experience all the stages of QGP evolution and their kinematics carry information about their interaction with the medium. So heavy quarks are an excellent probe for studying the properties of the QGP. Furthermore, heavy quark masses are external to QCD, which implies that their masses are not modified by the QGP created at RHIC and the LHC [68]. So heavy quarks are also a clean probe to study properties of the QGP. Fig. 1.10 shows the leading order diagrams of heavy quark production. Besides, the running coupling of the strong interaction α_s is small and nearly constant due to high momentum transfer of heavy quark production. Thus, heavy quark production can be described by pQCD ($p_T > m_{c,b}$) (shown in Fig. 1.12 and 1.13). And because of the heavy quarks are from hard scatterings of partons [69], they should be scaled with N_{coll} shown in the bottom-right panel of Fig. 1.12.

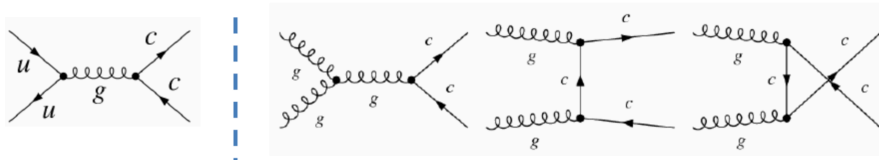


Fig. 1.10 Leading Order diagrams of heavy quark production.

1.3.2. Experimental results

Measurements of heavy quarks can improve our understanding of parton interactions with the QGP and its properties. The heavy quark production in $p+p$ collisions provides a baseline to similar measurements in heavy-ion collisions and is expected to be well

described by pQCD calculations. Thus measurements of heavy quark production in both $p + p$ and $Au + Au$ collisions are crucial. In experiments, heavy quark production can be studied via two methods: direct reconstruction through hadronic decay channels and indirect measurement through semi-leptonic decay channels. Fig. 1.11 shows one sample of heavy quark fragmentation to hadrons and two main decay channels of heavy quark hadrons.

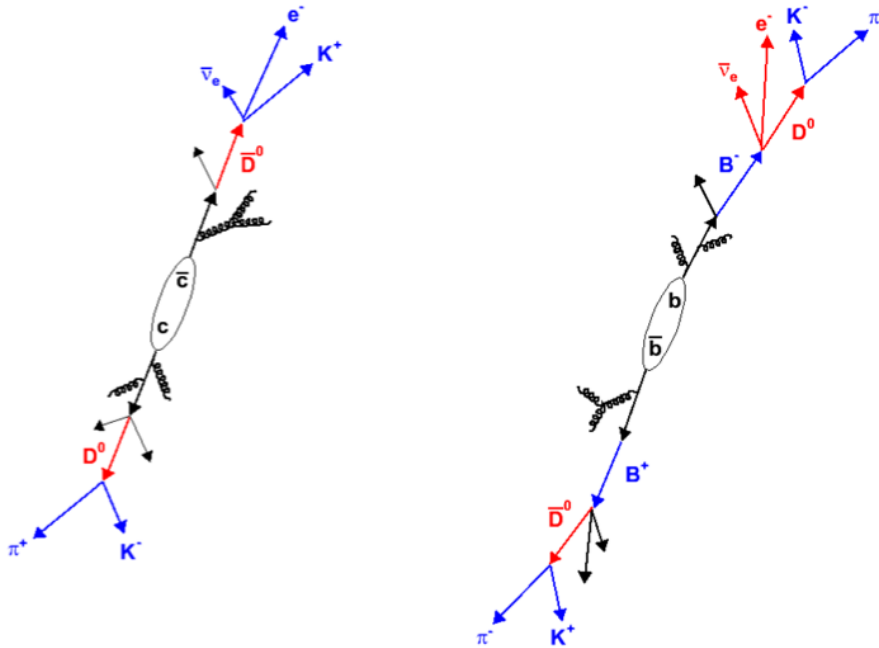


Fig. 1.11 Heavy quark fragmentation to D^0 and two main D^0 decay channels.

For charm hadron production, they can be fully reconstructed via the hadronic decay channel using topological cuts. But there is a large combinatorial background when all particles from the collision vertex are included, which is caused by the secondary weak-decay vertices (where the heavy flavor hadron decays) and the collision vertex couldn't be distinguished due to the very short decay length of open heavy flavor hadrons and limited track pointing resolution of detector. This background is particularly large in HIC. As the installation of STAR secondary vertex tracker, Heavy Flavor Tracker (HFT), the combinatorial background is rejected using the topological cuts enabled by the HFT. So the charm hadrons signal significance is largely improved. The STAR D^0 invariant yields with HFT at mid-rapidity ($|y| < 1$) as a function of p_T in different centralities in 200 GeV $Au + Au$ collisions are shown in the top-right panel of Fig. 1.12. Meanwhile the top-left panel shows the STAR $c\bar{c}$ production cross-section in 200 GeV $p + p$ collisions [9]. As seen, the result agrees with fixed-order next-to-leading logarithm (FONLL) pQCD calculations [70, 71] and measurements of charm cross-section from different channels are consistent in a wide p_T range. The bottom-left panel of

Fig. 1.12 shows the extracted $D^0 R_{AA}$ in 0-10% central 200 GeV $Au + Au$ collisions. The strong suppression of $D^0 R_{AA}$ at high p_T is observed, while in the intermediate range, D^0 meson seems to have less suppression. For bottom hadron production, they are only indirectly measured through electrons, J/Ψ , and D^0 decay channels due to low production rate and reconstruction efficiency.

Non-photonic Electrons (NPE) are “single” electrons/positrons from open heavy flavor semi-leptonic decay channels (produced with (anti)neutrinos in weak decays). NPE can be used as proxies for studying heavy quarks. Although, one does not have direct access to heavy quark hadron kinematics through NPE, the higher branching ratios and ability to trigger on high p_T electrons make NPE a very good tool to study heavy quark production in different collision systems and at different centralities. The left panel of Fig. 1.13 shows the STAR published NPE invariant yields as a function of p_T at different centralities in 200 GeV $Au + Au$ collisions, along with that in 200 GeV $p + p$ collisions and FONLL calculations. And the right panel shows NPE R_{AA} in 0-5% central 200 GeV $Au + Au$ collisions, comparing with STAR charged hadrons result and that in $d + Au$ collisions. And the measurement of high p_T NPE production shows a strong suppression in the R_{AA} .

For the NPE R_{AA} , the previous STAR results at high p_T have very large uncertainties and there is no measurement at low p_T . Recently, a large sample of data are produced in $p + p$ and $Au + Au$ collisions at STAR, the motivation of this dissertation is to present the first measurement of low p_T NPE in 200 GeV $p + p$ collisions and make precise NPE measurement in $Au + Au$ collisions, and thereby a comprehensive set of studies with heavy quark hadrons decayed electrons will be initiated. As seen from Fig. 1.12, the missing of the first two and last two data points for the $D^0 R_{AA}$ is due to a lack of the measurement in $p + p$ collisions. Comparing with the open heavy flavor hadron production (D^0 result), the measurement of NPE cannot fully reveal the parent hadron kinematics, but it can enrich the measurement of the p_T integrated spectra and R_{AA} to very low and high p_T for heavy quark production due to its higher branch ratio. This is very important to quantitatively understand the QGP created at RHIC and provide the constraints to theoretical models thereby comprehend the heavy quark production mechanism and how the behavior of heavy quark hadrons decayed electrons reflects heavy quarks. Furthermore, the theory predicts the heavy quarks lose less energy than light quarks through soft gluon radiation (caused by propagation of a fast parton (quark) through QCD medium) due to the “dead cone” effect [72]: gluon radiation is mass suppressed at angles smaller than the ratio of the quark mass M to its energy E

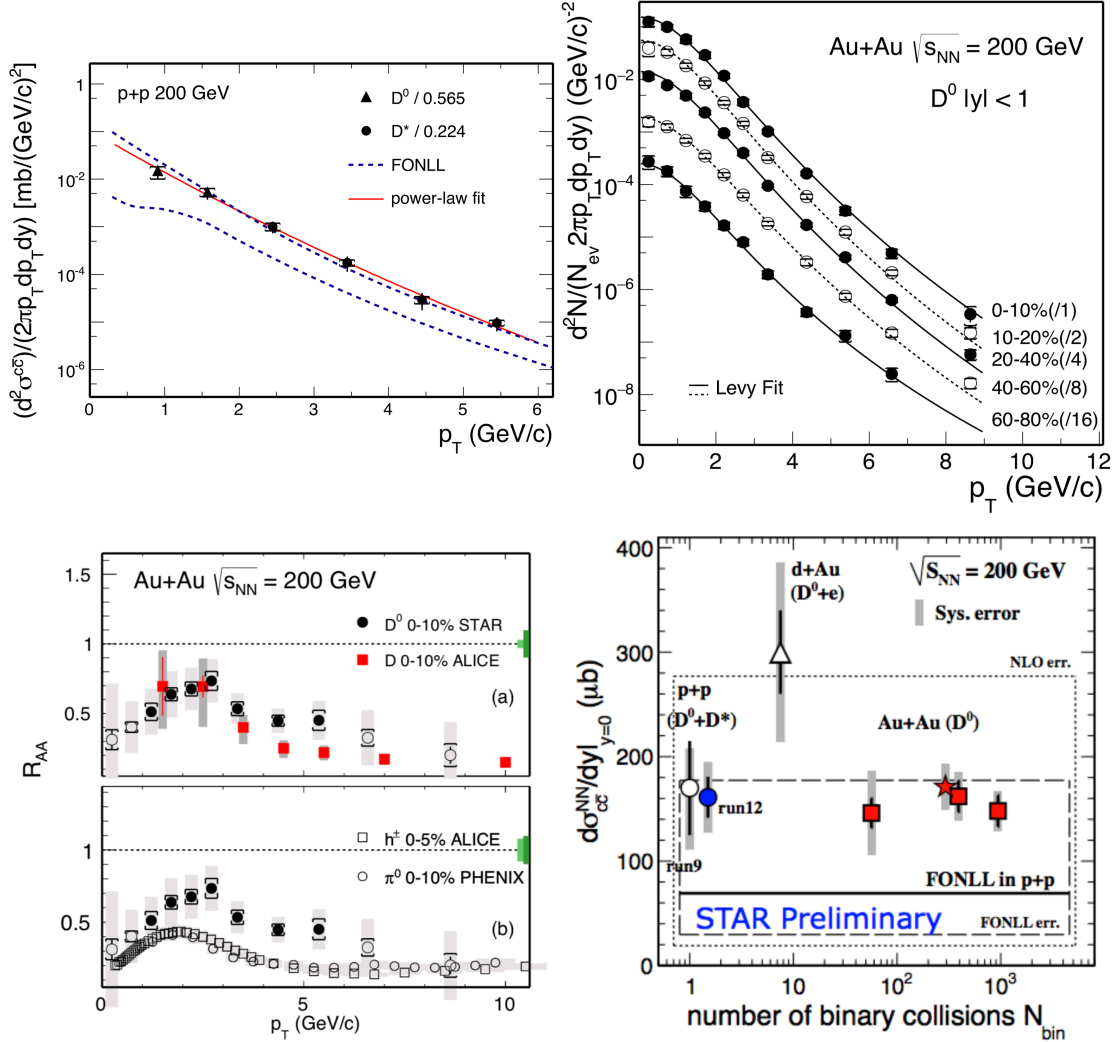


Fig. 1.12 Top-left panel: $c\bar{c}$ production cross section as inferred from D^0 and D production in 200 GeV $p+p$ collisions compared with FONLL calculations. Figure was taken from [9]. Top-right panel: D^0 invariant yields at mid-rapidity ($|y| < 1$) vs. transverse momentum for different centralities in 200 GeV $Au + Au$ collisions [10]. Bottom-left panel: D^0 R_{AA} in 0-10% central 200 GeV $Au + Au$ collisions, comparison to ALICE D meson result, and hadron from ALICE and π^0 from PHENIX [10]. Bottom-right panel: Charm production cross sections at mid-rapidity per nucleon nucleon collisions as a function of N_{coll} [11].

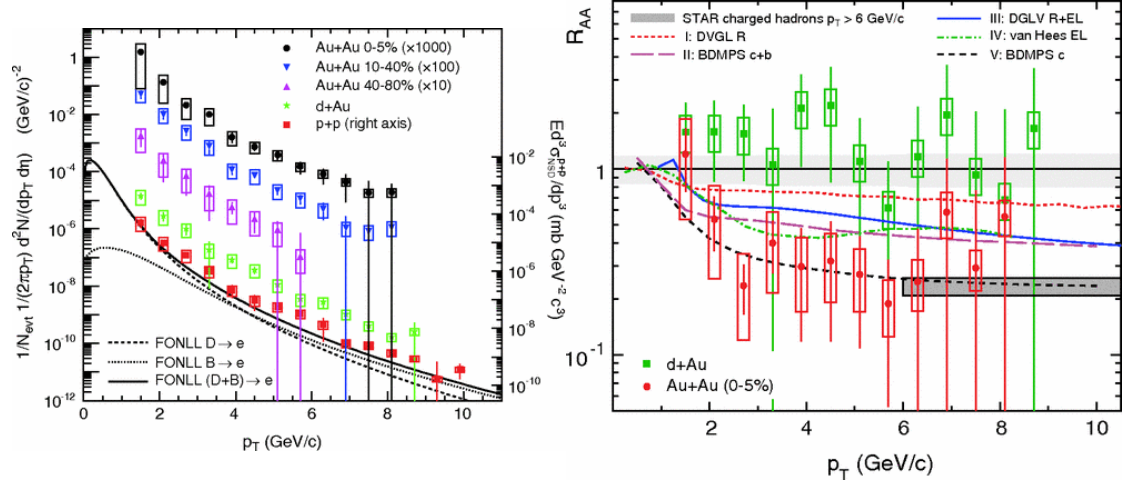


Fig. 1.13 Left panel: NPE invariant yields at mid-rapidity ($|y| < 0.7$) vs. transverse momentum for different centralities in 200 GeV $Au + Au$ collisions, along with NPE result in $p + p$ collisions and FONLL calculation. Right panel: NPE R_{AA} in 0-5% central 200 GeV $Au + Au$ collisions, comparison to NPE result in $d + Au$ collisions. Figures were taken from [12].

$\left(\frac{dP(\text{heavy quark})}{d\theta^2}\right) = \left(1 + \frac{M}{E} \frac{1}{\theta^2}\right)^{-2} \frac{dP(\text{light quark})}{d\theta^2}$. This means that there is a mass hierarchy of the parton energy loss for radiative energy loss ($\Delta E_g > \Delta E_{u,d,s} > \Delta E_c > \Delta E_b$). However, the suppression of the D^0 and NPE R_{AA} show similar suppression comparing that of light hadrons at high p_T ($p_T > 6$ GeV/c) reaffirming significant energy loss for charm quarks inside the sQGP medium. So how about bottom quark production? From CUJET calculations for central 200 GeV $Au + Au$ collisions [13] shown in the left panel of Fig. 1.14, the charm and bottom quarks can be well separated at RHIC. But as mentioned above, the bottom quark hadron can only be indirectly studied via electrons, J/Ψ , and D^0 decay channels at RHIC due to very small branching ratios of its hadronic decay channels. For electron channel, the bottom quark contribution to NPE production in 200 GeV $p+p$ collisions has been obtained using azimuthal correlations between non-photonic electrons and hadrons (h, D^0) [14], which is shown in the right panel of Fig. 1.14. Combining with the measurement in 200 GeV $Au + Au$ collisions making use of the precise measurement of displaced vertices from HFT, the R_{AA} of electrons from bottom and charm quark hadron decays will be obtained. The R_{AA} measurements of J/Ψ and D^0 from bottom quark hadron decays have model dependence due to in absence of their yield measurements in $p + p$ collisions [73]. The measured R_{AA} in this dissertation will provide the inclusive ones for the separate R_{AA} measurements of charm and bottom quark hadron decayed electrons. This will be discussed in Chapter 5.

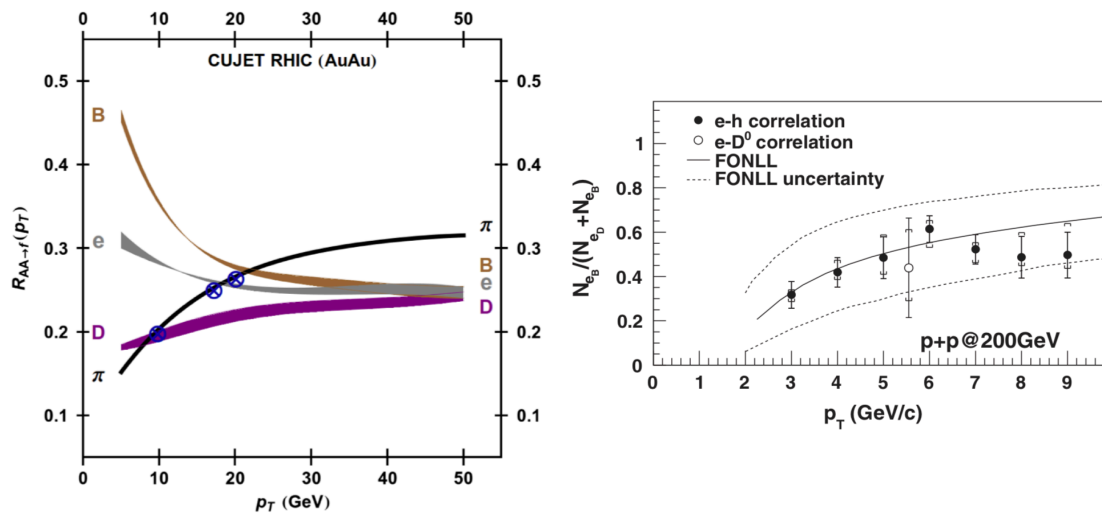


Fig. 1.14 Left panel: Jet flavor tomography level crossing pattern of nuclear modification factors as a function of p_T at $y = 0$ for π , D , B , e fragmentation from quenched g , u , c , b jets in 0-5% central 200 GeV $Au + Au$ collisions at RHIC. Figure was taken from [13]. Right panel: Relative contribution from B mesons to open heavy flavor hadron decayed electrons in 200 GeV $p + p$ collisions. Figure was taken from [14].

Chapter 2 Experimental Setup

2.1 The Relativistic Heavy Ion Collider

RHIC has been operated since year 2000 and is made up of two concentric storage rings with 3.8 km circumference, blue ring with clockwise direction and yellow ring with counter-clockwise one. RHIC is the world's only machine which can collide spin-polarized proton beams to investigate spin physics. For the heavy-ion beams, the center-of-mass collision energy can reach 100 GeV per nucleon and the top energy is up to 250 GeV for the polarized proton beams. The initial designed average luminosity is $2 \times 10^{26} \text{ cm}^{-2}\text{s}^{-1}$ for $Au + Au$ collisions and $1.4 \times 10^{31} \text{ cm}^{-2}\text{s}^{-1}$ for $p + p$ collisions [74]. After updating on the facilities, there is $50 \times 10^{26} \text{ cm}^{-2}\text{s}^{-1}$ for $Au + Au$ collisions (Run 2014) and $3.3 \times 10^{31} \text{ cm}^{-2}\text{s}^{-1}$ for $p + p$ collisions (Run 2012). The detailed information can be found at [75].

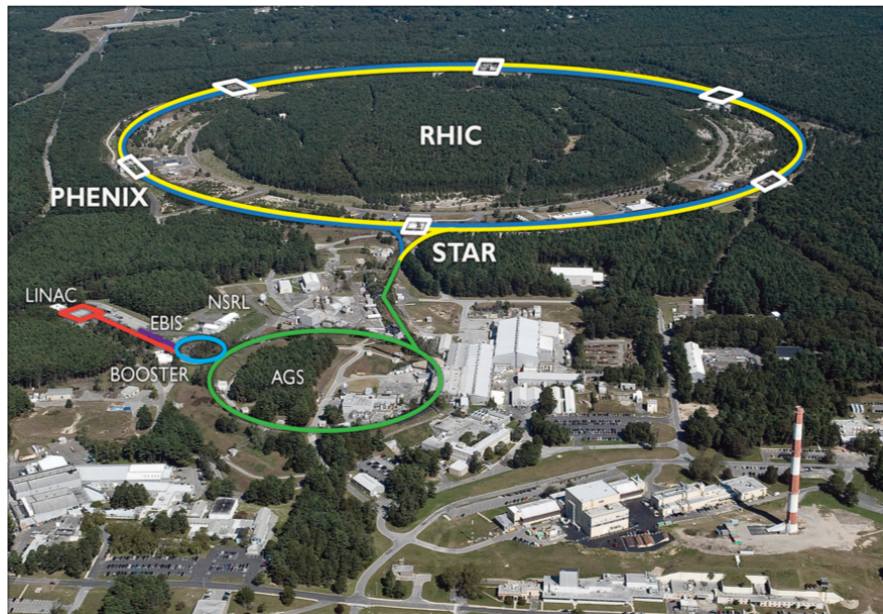


Fig. 2.1 Relativistic Heavy Ion Collider Facility.

Fig. 2.1 shows the RHIC facility with two ring tunnels and the accessorial accelerators including the Electron Beam Ion Source (EBIS), the Booster Synchrotron and the Alternating Gradient Synchrotron (AGS), which can initially accelerate particles and strip electrons from them. Au ions with the charge state of +32 and the energy of 2 MeV/u produced by EBIS [76] are carried to the Booster, and then accelerated to 95 MeV/u and stripped electrons to the charge state of +77 at the exit. Then the ions are delivered to the AGS, where they are re-bunched to four bunches, accelerated to 10.8

GeV/u and stripped to the charge state of +79. The beams from AGS are transferred to RHIC, in which they are accelerated to the maximal energy 100 GeV/u and collide at six intersection points. For proton beams, they are injected from the 200 MeV Linac into the Booster, further followed by the AGS and finally transferred to RHIC.

Right now, one of the six intersection points are in operation. They is STAR [77] located at 6 o'clock on the tunnel (PHENIX [78] at 8 o'clock has been stopped operation in 2016). In the following sections, there is the detailed description of STAR.

2.2 The Solenoidal Tracker at RHIC

The Solenoidal Tracker at RHIC (STAR) detector specializes in tracking the thousands of particles produced by each ion collision at RHIC. Weighing 1,200 tons and as large as a house, STAR is a massive detector. The STAR is one of two large experiments at RHIC. It is used to research the strongly interacting matter behavior at high energy density and to search for the signatures of the formation of QGP produced by heavy-ion collisions at RHIC. In order to achieve these goals, STAR was designed to mainly measure the production of hadrons at a large solid angle. The detector systems are characterized by high accuracy tracking, momentum analysis and good Particle Identification (PID) [79]. It has a large azimuthal symmetric acceptance ($0 < \phi < 2\pi$) and pseudorapidity range $|\eta| < 1.8$. Fig. 2.2 illustrates the STAR complex with the subsystems.

The HFT [80], which is close to the beam pipe, was installed at STAR and participated in data taking from 2014 to 2016. It is composed of three sub-detectors: the silicon PiXeL detector (PXL), the Intermediate Silicon Tracker (IST) and the Silicon Strip Detector (SSD). It provides an excellent track pointing resolution for precise measurements of displaced vertices. Its resolution is less than 30 μm for charged particles with $p_T > 1.5 \text{ GeV}/c$. Therefore, the HFT is used to identify particles from charm and bottom hadron decays by taking advantage of their different decay lengths. From inside to outside, surrounding the HFT, there are the Time Projection Chamber (TPC) [81], the Time Of Flight (TOF) detector [82], the Barrel Electromagnetic Calorimeter (BEMC) [83], the STAR magnet [84], and the Muon Telescope Detector (MTD) [85]. The STAR magnet system, which is a cylindrical in geometry with a length of 6.85 m and inner and outer diameter of 5.27 m and 7.32 m respectively, was designed as a room temperature solenoidal magnet. It can provide a near uniform field paralleling the beam direction and having the operating range from 0.25 T to 0.5 T for the measurement of charged

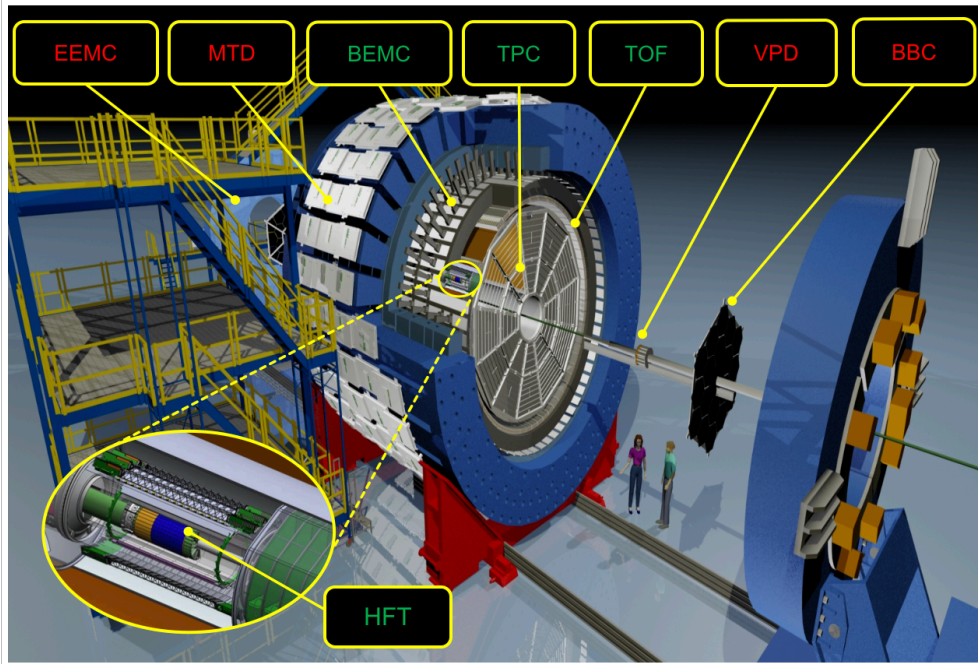


Fig. 2.2 Overview of STAR detector.

particle momentum. The MTD, covering $|\eta| < 0.5$ in pseudorapidity and $\sim 45\%$ in azimuth, was installed in 2014. It was designed to measure the transverse momentum distributions of quarkonia via detecting high p_T muon.

Due to the RHIC crossing rate is ~ 10 MHz [86] and the slow detectors, which provide PID and the momentum based on our physics conclusions, can only operate at rates of ~ 2100 - 2200 Hz. The STAR trigger was designed to be a pipeline system on the strength of information collected by faster detectors in order to provide case selection information for these slower detectors. The fast detectors include the Vertex Position Detector (VPD) [87], the Beam-Beam Counter (BBC) [88] and the Zero Degree Calorimeter (ZDC) [89]. All of these three detectors were installed at the East and West of the collision area. The VPD is used to select minimum bias collisions, to measure the position of primary vertex along the beam pipe and to provide “start time” measurement for other fast detectors such as TOF and MTD due to its precise timing information. Each VPD detector wrapping the beam pipe is set at 5.7 m away from the center of the STAR and covers a pseudo-rapidity range of $4.24 < |\eta| < 5.1$. The BBC covering $3.4 < |\eta| < 5.0$ is located in a distance of 3.75 m from the center of STAR. Each BBC is made up of 18 hexagonal scintillator tiles, at least one of which firing in both East BBC and West BBC form a prompt coincidence corresponding to a BBC trigger. It provides a minimum bias trigger for $p + p$ collisions. With the information of BBC, the relative luminosity is also measured. The ZDC located in the forward < 4 mrad is 18 m away

from the collision points, outside of the STAR magnet along the beam line. So the ZDC can only detect the outgoing neutrons as a hadronic calorimeter. It is mainly used to as a minimal bias selection and monitor beam luminosity for heavy-ion collisions.

In our analysis, the mainly utilized detectors are TPC, TOF and BEMC. These sub-detectors are described in the following sections.

2.2.1. The Time Projection Chamber

The TPC [81] as the primary tracking device is the “heart” of the STAR detector. It, covering full azimuth within pseudorapidity range of $|\eta| < 1.8$, provides tracking, momentum determination and PID via measuring ionization energy loss (dE/dx). The TPC can measure and identify the charged particles over a momentum range of $100 \text{ MeV}/c \sim 30 \text{ GeV}/c$ and $100 \text{ MeV}/c \sim 1 \text{ GeV}/c$, respectively.

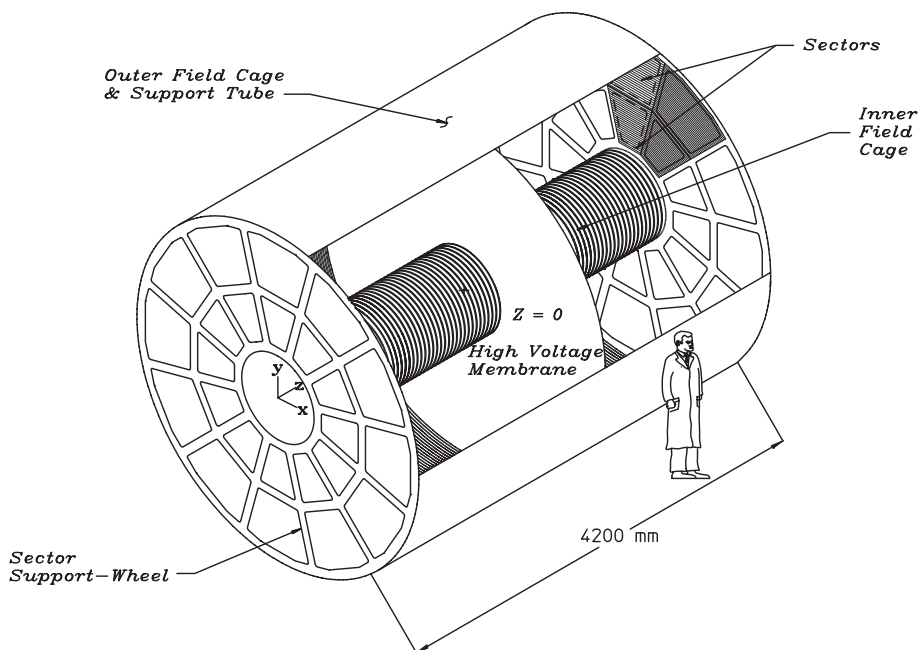


Fig. 2.3 Schematic of the TPC.

The schematic of TPC structure is shown in Fig. 2.3. The TPC, sited in the STAR solenoid magnet, has the length of 4.2 m along the beam line, the inner and outer diameter of 1 m and 4 m. It is an empty volume, filled with P10 gas (10% CH_4 + 90% Ar), divided into two working parts by the central high-voltage (28 kV) membrane electrode. An axial drift field is formed by two internal and external uniform field electrodes between the membrane electrode and the entrance window (ground potential) located at

readout area at the both ends of TPC. The electron has a fast drift velocity $\sim 5.45 \text{ cm}/\mu\text{s}$ in the P10 gas at the 130 V/cm drift field and 0.5 T magnetic field. The readout system [90] of the TPC is based on the Multi-Wire Proportional Chamber (MWPC) with readout pads. The readout planes around the circle at each end of TPC have 12 sub-sectors with total 136608 readout pads. Each sector is also divided into inner ($2.85 \text{ mm} \times 11.5 \text{ mm}$) and outer ($6.02 \text{ mm} \times 19.5 \text{ mm}$) sub-sectors. The anode voltage and gas gain are 1170 V and 3773 for inner sub-sectors, 1390 V and 1230 for outer sub-sectors. Fig. 2.4 shows the anode pad plane of one full TPC sector.

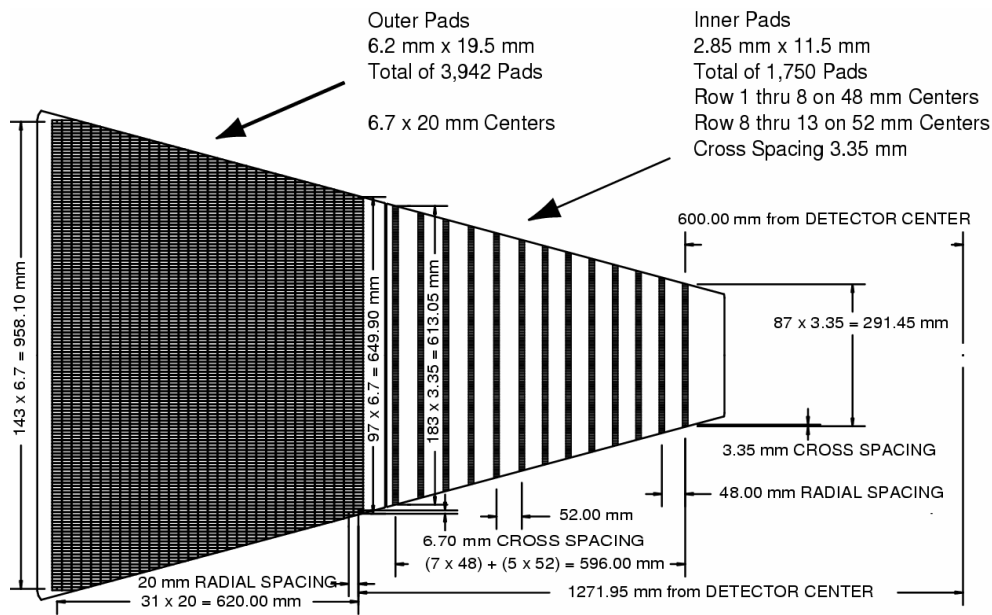


Fig. 2.4 Anode pad plane of one full TPC sector.

The primary charged particles release electrons from the TPC gas due to energy loss, when they pass through the TPC. These secondary electrons are drifted towards the end cap of the TPC and then amplified by the avalanching in MWPC. The signal is sensed on several readout pads. Then it is amplified and shaped by the front-end electronic circuit. Finally it is digitized and transmitted to STAR Data Acquisition (DAQ) system via a set of optical fibers. At the DAQ stage, the track of the primary particle through the TPC is determined by looking for the spatial coordinates of the secondary electrons ionization cluster along the track. The x-y coordinate position of each ionization cluster can be reconstructed with the gravity method of charge using three readout pads, while the z coordinate is measured by the average drift velocity and the time of secondary electron clusters from the original position to anode wire in the end cap. After associating the clusters along the track, it is fitted by helical trajectory. Then the track is extrapolated to the other detectors, maybe combined with any other available

points from other detectors and refitted by application of a Kalman filter routine [91]. The resulted track from there on is called a global track. Using the all global tracks belong to the same event, the primary vertex is then reconstructed. Using the primary vertex as additional point, a refit on a global track, whose distance of closest approach (dca) is less the 3 cm, is preformed by a constrained Kalman fit then the track is named as a primary track. As expected, the resolution decreases as the square root of the number of tracks used in the calculation and can reach 350 μm with more than 1000 tracks. In $p+p$ collisions, the momentum resolution of primary track is approximately $\Delta p_T/p_T \sim 1\% + 0.5\%p_T$.

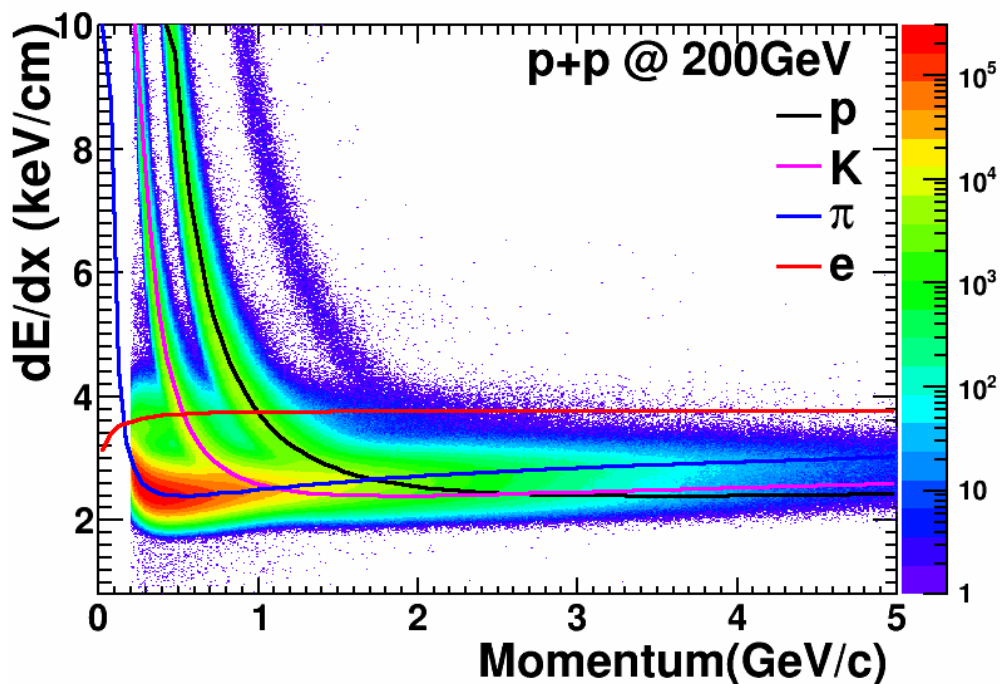


Fig. 2.5 dE/dx distribution as a function of momentum for different particles. The theoretical curves are calculated from Bichsel functions.

The TPC can not only provide the tracking and momentum, but also distinguish the charged particles via dE/dx , which is determined from the deposit charge collected on up to 45 pad rows. It is impossible for accurately measuring the average dE/dx because of the length used to measure the energy loss of particles is too short to average out ionizations. Thus, the most probable dE/dx is applied by removing the highest 30% of the measured clusters. Fig. 2.5 shows the dE/dx as a function of momentum for different charged particles. The theoretical curves of dE/dx for charged particles described by the Bichsel functions [92, 93] are also shown. TPC can make π/K separation up to ~ 0.7 GeV/ c and identify proton/meson up to ~ 1.1 GeV/ c . In actual analysis, the $n\sigma_X$

($X = \pi, K, p, e, \text{etc.}$) instead of dE/dx is used and defined as the measured dE/dx with respect to the expected dE/dx value:

$$n\sigma_X = \frac{\ln \frac{(dE/dx)^{\text{mea}}}{dE/dx_X^{\text{th}}}}{R_{dE/dx}}, \quad (2.1)$$

where the superscripts “mea” and “th” are measured and theoretical values, respectively, and $R_{dE/dx}$ is the dE/dx resolution.

The capability of the particle identification can be greatly improved and extended to the higher p_T area by combining TPC with other detectors. From dE/dx distribution, we can see that it is difficult for low- p_T electron identification if only used TPC because the electron band crosses several hadron bands. Thus the TOF need to be applied to reject the hadrons at low p_T . For high- p_T electron identification, the TPC can provide powerful hadron rejection for electron candidates due to the electron dE/dx band is above all of the three hadron bands. But the electron yield is very poor. Therefore, the high-tower trigger (HT) from BEMC is used to enhance the high p_T electrons, and the ratio of momentum to energy measurements (p/E) and shower shape from BEMC are utilized to identify the electrons. The information of TOF and BEMC will be shown in next section 2.2.2 and 2.2.3.

2.2.2. The Time Of Flight detector

The TOF covers $|\eta| < 1$ within full azimuth and provides PID capability through measured time-of-flight. Its intrinsic resolution is < 80 ps and detecting efficiency is more than 95%. It is based on Multi-Resistive Gap Chamber (MRPC) [94] technique. The TOF is made up with 120 trays (60 trays at $\eta > 0$ and $\eta < 0$, respectively), and each tray consists of 32 MRPC modules and covers 6 degrees in azimuthal direction and 1 unit in pseudorapidity direction. Fig. 2.6 shows the two side views of a MRPC module appropriate for STAR. Each MRPC module consists of 7 resistive plates including 5 inner glass (0.54 mm thickness) and 2 outer glass (1.1 mm thickness) with graphite electrodes on the outer surface, and each plate has a gas gap of $220 \mu\text{m}$. And there are 6 readout pads with the size of $6.1 \times 3.4 \text{ cm}^2$ on each MRPC module. The entire module has an effective area of $20.0 \times 6.2 \text{ cm}^2$. A strong electric field is generated in each gas gap after high voltages are applied to these electrodes. When charged particles pass through these layers of glass, they produce a primary ionization along their track in the gas. The strong electric field will cause them to produce the Townsend amplification avalanche. Because the electrodes and glass plates are both resistive, they are transparent to the charge induction from avalanches in the gaps. Therefore, the sensing signal

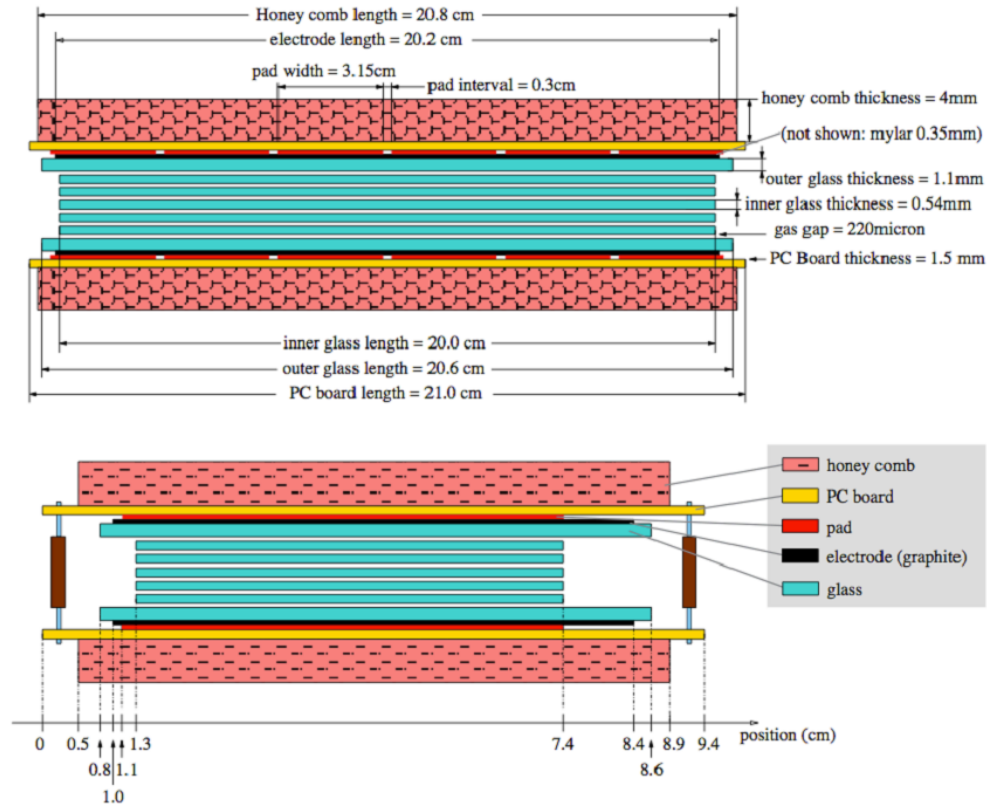


Fig. 2.6 Two side views of a MRPC module.

on the readout pad outside the electrode is the superposition of the avalanche signal in all gas gaps.

The TOF can give the flight time ($\Delta t = t_2 - t_1$) of a particle by measuring the “stop time” (t_2) combining with the “start time” (t_1) measured by VPD. Then using the the information from TPC (momentum (p) and path length (L)), the inverse velocity ($1/\beta$) can be calculated:

$$\frac{1}{\beta} = c \frac{\Delta t}{L} = \frac{\sqrt{p^2 + m^2 c^2}}{p}, \quad (2.2)$$

The mass (m) of the particle can be subsequently calculated:

$$m = \frac{p}{c} \sqrt{\frac{1}{\beta^2} - 1}. \quad (2.3)$$

The left panel of Fig. 2.7 shows the $1/\beta$ distribution as a function of momentum. As we can see, the TOF can provide extra information for PID. It not only extend π/K separation from $0.7 \text{ GeV}/c$ to $1.6 \text{ GeV}/c$ and proton/ (π, K) separation from $1.1 \text{ GeV}/c$ to $3 \text{ GeV}/c$, but also is significantly useful for electron identification at low momentum. Due to the small mass of electron, via applying a $1/\beta$ closed to 1 cut, the electrons can be identified with TPC $n\sigma_e$ distribution, which is shown in the right panel of Fig. 2.7.

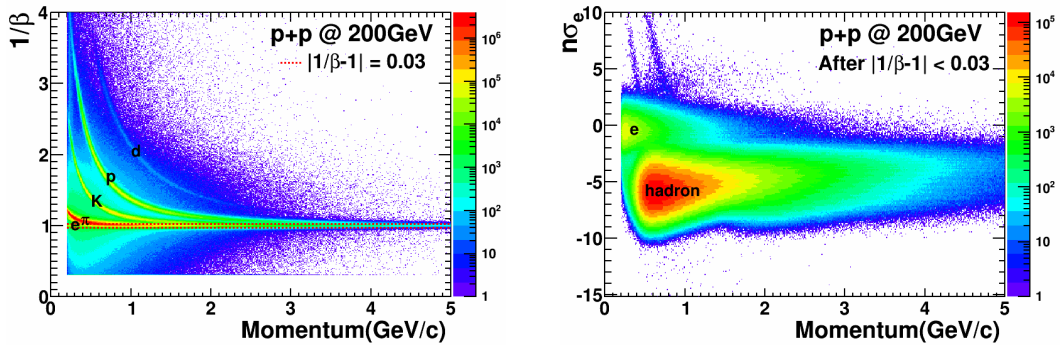


Fig. 2.7 Left panel: $1/\beta$ distribution as a function of momentum for different particles. Right panel: $n\sigma_e$ distribution as a function of momentum after $1/\beta$ cut.

2.2.3. The Barrel Electromagnetic Calorimeter

The BEMC, covering $|\eta| < 1$ and full azimuth, can trigger on and identify high- p_T electrons via p/E . Its front surface is at a radius of 220 cm and parallel to the beam direction. There are a total of 120 calorimeter modules (60 in ϕ direction and 2 in the η), each covering 6 degrees in the ϕ direction and 1 unit in η . Each module is approximately 26 cm wide, 293 cm long, and effective thickness 23.5 cm. The supporting structure is approximately 6.6 cm thick (including 1.9 cm in front of the detector). Furthermore, each module is divided into 40 towers (2 in the ϕ direction by 20 in η) with each tower subtending 0.05 in $\Delta\phi$ by 0.05 in $\Delta\eta$. The entire BEMC is divided into 4800 towers, each of which is projected and points back to the center of the TPC. The left panel of Fig. 2.8 shows a side view of a module demonstrating the projective nature of the towers along the η direction and the right one shows a side view of a module showing the mechanical assembly including the compression components and the rail mounting system.

The BEMC is a sampling calorimeter using lead and plastic scintillator. The core of each module is made up of the lead scintillator stack and shower maximum detector located at about 5 radiation lengths from the front of the stack. There are 20 lead layers with 5 mm thickness, 19 scintillator layers with 5 mm and 2 scintillator layers with 6 mm used for the preshower detector. The total depth of BEMC has approximate 20 radiation lengths ($20 X_0$) at $\eta = 0$. Its intrinsic energy resolution is $\sigma_E/E \approx 1.5\% \oplus 14\%/\sqrt{E}$ [GeV]. For electrons, they will deposit 95% energy due to the electromagnetic shower when pass the BEMC. However there is a little energy deposition for hadrons. So the p/E ratio should be peak at unity for electrons while that of hadrons should have a broad distribution and it has some possibility to be very large for that of the non-showering hadrons. The electrons can be identified with hadrons via p/E cut selection.

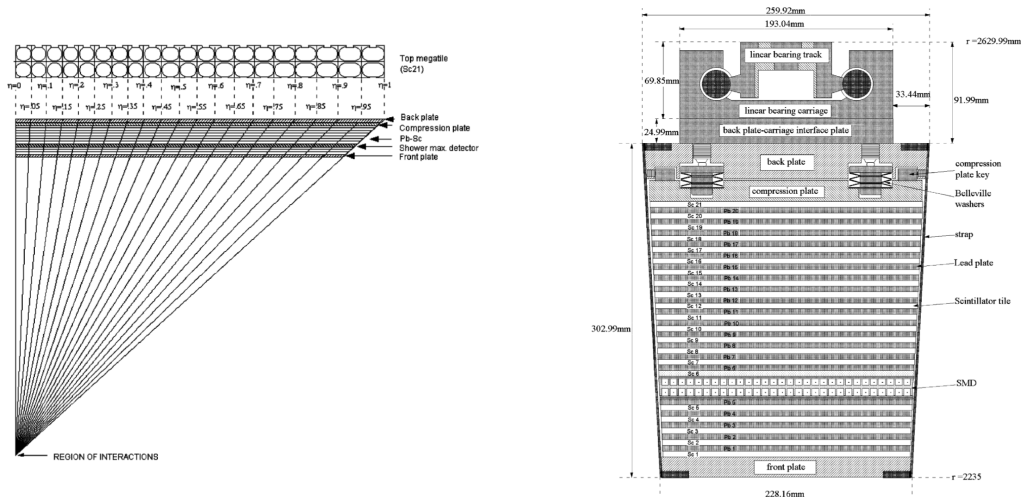


Fig. 2.8 Schematic view of BEMC module. Left panel: Side view of a calorimeter module showing the projective nature of the towers along the η direction. Right panel: Side view of a module showing the mechanical assembly including the compression components and the rail mounting system.

Despite the BEMC provides precise energy measurement for isolated electromagnetic showers, it has not enough good spatial resolution. The Shower Maximum Detector (SMD) is embedded in $\approx 5.6 X_0$ depth of BEMC at $\eta = 0$ and used to provide the high spatial resolution for π^0 reconstruction, direct gamma and electron identification via giving the information on shower position and shape. The SMD was designed as a double-layer detector. Fig. 2.9 shows the schematic illustration of the double layer SMD. The double sided aluminum extrusion provides the ground channels for two independent plane of proportional wires. Two dimensional image of the shower shown in Fig. 2.9 is allowed to be reconstructed due to the independent PC board cathode plane with the strip etched in the ϕ direction and η direction, respectively.

The SMD has an approximately linear response versus energy in the energy range from 0.5 to 5 GeV. And comparing the ionization at the front plane of the SMD, there is about 10% lower about that in the back plane. The energy resolution on the front plane is about $\sigma_E/E \approx 12\% \oplus 86\%/\sqrt{E}$ [GeV], and that on the back plane is reduced by 3-4%. The position resolutions in the front and back planes of SMD are given approximately by $\sigma_{front} (mm) = 2.4 mm + 5.6 mm/\sqrt{E}$ [GeV] and $\sigma_{back} (mm) = 3.2 mm + 5.8 mm/\sqrt{E}$ [GeV]. The electromagnetic showers have the maximum spatial extent at the depth of $\approx 5.6 X_0$ for electrons but hadron showers are usually not fully developed at this depth due to the nuclear interaction length of hadrons is large more than radiation length of electrons. Therefore, the number of SMD hits produced

by hadrons is usually less than those produced by electrons. Applying SMD hits cut can be used for further hadron projection. In addition, the distance between the position of shower center provided by SMD and the track projection position on SMD from TPC can also be used to reject hadrons on account of the wider distribution for hadrons than for electrons.

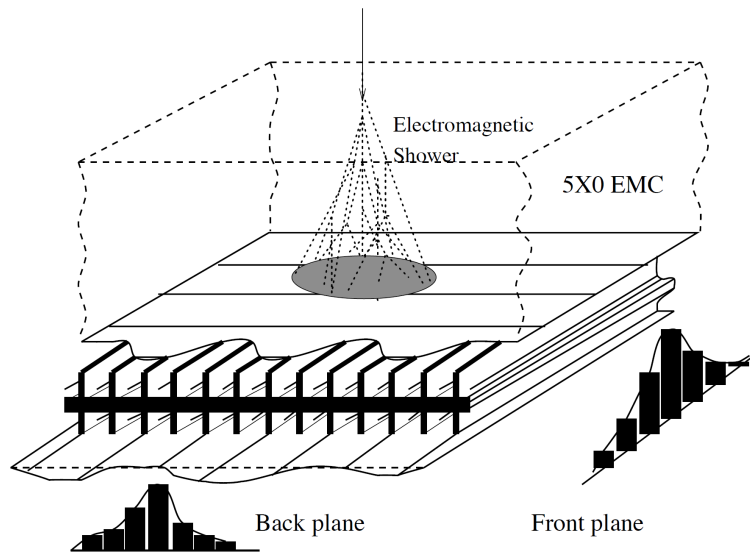


Fig. 2.9 Schematic illustration of the double layer SMD.

Chapter 3 Non-photonic Electron Analysis

Heavy quark production can be studied via measuring the electrons from semi-leptonic decays of heavy flavor hadrons, also known as NPE. Although, one does not have direct access to heavy quark kinematics through NPE, the higher branching ratios make NPE a very good tool to study heavy quark production. In this chapter, the details of NPE analysis techniques from 200 GeV Run 2012 $p + p$ and Run 2014 $Au + Au$ collisions will be presented.

3.1 Run 2012 200 GeV $p + p$ Collision Analysis

3.1.1. Analysis principle

All identified electrons in one event are called inclusive electrons, and they consist primarily of three components:

- “non-photonic” electrons from open heavy-flavor decays.
- “photonic” background from Dalitz decays of light neutral mesons and gamma conversion. Mainly:
 - gamma conversion: $\gamma \rightarrow e^+e^-$ in the material of STAR detector.
 - π^0 Dalitz decay: $\pi^0 \rightarrow e^+e^-\gamma$ (1.174 ± 0.035)%.
 - η Dalitz decay: $\eta \rightarrow e^+e^-\gamma$ (0.69 ± 0.04)%.
 - Direct gamma.
- “non-photonic” background:
 - Heavy quarkonia contribution (J/Ψ).
 - Di-electron decays of vector mesons (ω, ϕ, \dots), dominant contribution to low p_T .
 - Single electrons background sources, $K \rightarrow e\pi\nu$ (K_{e3}).

In this analysis, we are particularly interested in NPE. The NPE raw yield is extracted using the equation $N_{NPE} = N_{INCE} * purity - N_{PHE}/\epsilon_{PHE}$, where N_{INCE} is the raw yield of INCLUSIVE Electron (INCE) candidates, purity the fraction of real electrons in

the inclusive electron candidates, N_{PHE} the raw yield of Photonic Electron (PHE) candidates obtained via selecting the invariant mass of e^+e^- pairs, and ϵ_{PHE} the photonic electron reconstruction efficiency. Then the final yield of NPE is obtained after that the NPE raw yield is corrected by the detector acceptance and efficiency.

3.1.2. Dataset and Event selection

The analysis was based on the Run12 $p + p$ Minimum Bias (MB) triggered sample at low p_T collected in RHIC. The MB trigger was defined as a coincidence in both sides of VPD and an online vertex cut was applied to select the collisions happening in the center of the detector. There was total of ~ 700 M VpdMB events, which were the statistics for number of events satisfying the VpdMB trigger ID 370001 and 370011, in year 2012 200 GeV $p + p$ collisions. The data production library version was P12id.

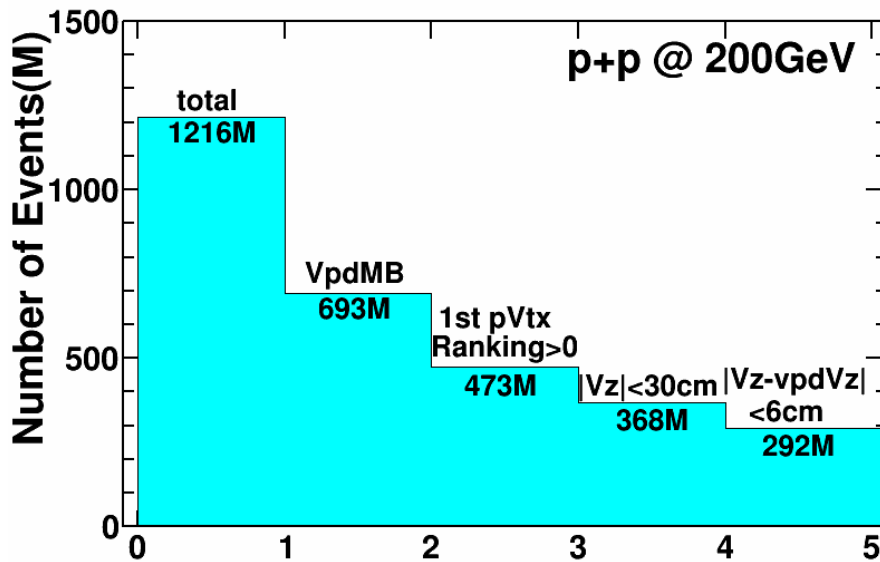


Fig. 3.1 Number of events with a series of selections.

Events used in this analysis were selected by the event selection criteria shown in Fig. 3.1. To insure the TPC performance, events were required to have a valid reconstructed collision vertex within 30 cm of the TPC center along the beam pipe (z direction). Due to high luminosity, a large fraction of pile-up events, which is caused by collisions originating from non-triggered bunch crossings, was collected. These pile-up events will result in additional tracks recorded in the TPC, except those from the triggered events. Thus the strict cuts were applied to suppress pile-up events. The V_z position of the reconstructed primary vertex from TPC tracks, which combined with the one from offline VPD data with good time, can provide a useful constraint to select the

real events that fired the trigger. Because of a good reconstructed V_z^{TPC} should be close to the V_z^{VPD} . By applying a vertex difference cut (6 cm), most of those pile-up vertices far away from the real vertex can be removed. The strong correlation and difference distribution between the V_z position from the TPC and the VPD are shown in Fig. 3.2.

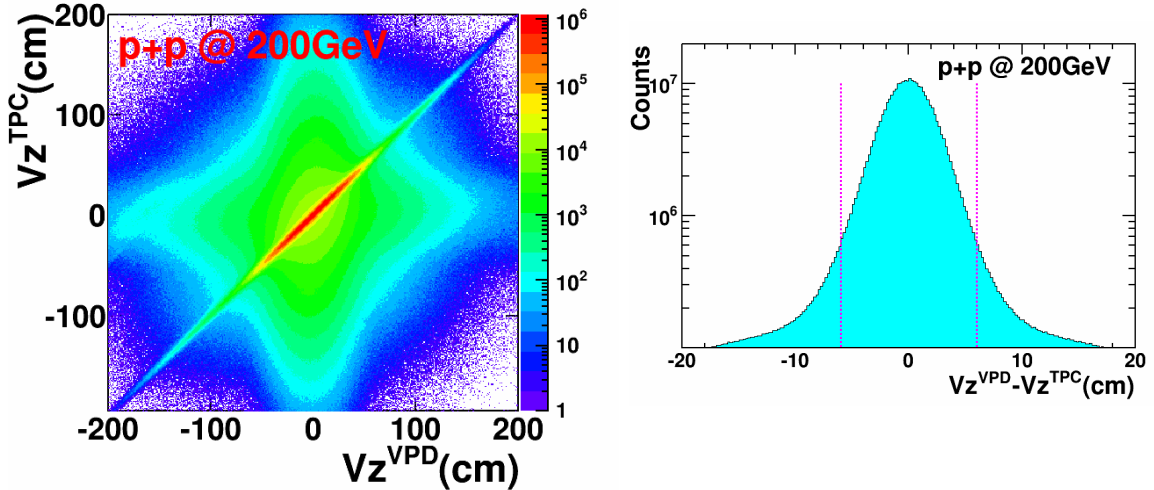


Fig. 3.2 Left panel: Correlations between V_z^{TPC} and V_z^{VPD} from MB triggered events. Right panel: Difference of V_z^{VPD} and V_z^{TPC} .

3.1.3. Track selection and Electron identification

In this analysis, three main detectors of STAR, the TPC, the TOF detector and the BEMC were used to reconstruct charged tracks and perform PID. All of these three detectors cover the full azimuth within pseudo-rapidity range of $|\eta| < 1$. The TPC provides tracking, momentum determination and PID via measuring dE/dx . The TOF provides PID capability through measured time-of-flight. The BEMC can trigger on and identify high- p_T electrons using p/E . As mentioned electron identification method in Chapter 2, electrons were identified using the TPC combined with the TOF at low p_T ($p_T < 1.5$ GeV/ c) and with the BEMC at high p_T ($p_T > 1.5$ GeV/ c) in this analysis. The detailed track selection and electron identification cuts will be presented in next section.

3.1.4. NPE raw yield extraction

1. Inclusive electrons and purity

For our inclusive electrons, identification was carried with TPC combined with TOF and BEMC. The main cuts for the track candidates and electron selections are listed

below:

Track quality cuts from TPC:

- Primary track.
- $nHitsFit \geq 20$: require TPC track fit points at least 20 out of 45 to ensure good tracking quality and momentum resolution.
- $0.52 < nHitsFit/nMax < 1.2$: reject splitting tracks.
- $nHitsDedx \geq 15$: ensure dE/dx resolution is good.
- $DCA < 1.0$ cm: the distance-of-closest-approach of the track to the primary vertex, make sure primary track for electron selection.
- $p_T > 0.2$ GeV/c, $|\eta| < 0.7$: ensure track reconstructed with good detector response within TPC acceptance.

Electron identification using TOF ($p_T < 1.5$ GeV/c) and BEMC ($p_T > 1.5$ GeV/c) information:

$p_T < 1.5$ GeV/c

- $TofMatchFlag > 0 \ \&\& \ \beta > 0$: require TOF matching.
- $|Y_{local}| < 1.8$ cm: TOF local pad position cut to remove edge effect.
- $|1/\beta - 1| < 0.03$: reject soft hadrons and ensure electron statistics within 2.5σ ($1/\beta$ distribution width for electron is 0.012 in Run12 $p + p$ collisions).
- $-1.0 < n\sigma_e < 3.0$: electron identification using dE/dx .

$p_T > 1.5$ GeV/c

- Tower energy $E > 0$: require BEMC matching.
- $0.3 < p/E < 1.5$: reject hadrons and ensure electron statistics [95].
- $-1.0 < n\sigma_e < 3.0$.

After applying the above cuts except $-1.0 < n\sigma_e < 3.0$, the $n\sigma_e$ distributions of identified particles in different p_T bins were obtained. The purity of inclusive electrons was got by using parameter functions to fit these $n\sigma_e$ distributions, including three steps.

Firstly we need to obtain the mean and sigma of the $n\sigma_e$ distribution in each p_T bin for pure electrons, which can be got through photonic electrons. Due to talking about

photonic electrons, the detailed information about how to get them will be explained in the next section. The Gaussian function was used to fit the $n\sigma_e$ distribution of pure electrons in each p_T bin and get the required parameters. The $n\sigma_e$ distribution and Gaussian fit of pure electrons in $1.10 < p_T < 1.20$ GeV/c bin, mean and sigma from fitting results as a function of p_T are exhibited in Fig. 3.3.

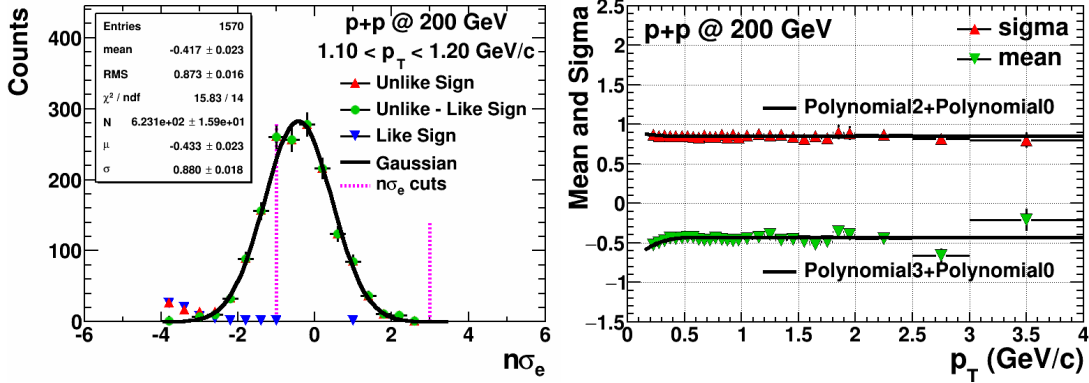


Fig. 3.3 Left panel: $n\sigma_e$ distribution in $1.10 < p_T < 1.20$ GeV/c bin of pure electrons. The Gaussian function was used to fit this distribution. The pink lines show the $n\sigma_e$ cuts of inclusive electrons. Right panel: Mean and sigma from the fitting of $n\sigma_e$ distribution for pure electrons as a function of p_T . The polynomial3/polynomial2 + polynomial0 were performed to fit them.

Secondly the mean and sigma of the $n\sigma_e$ distributions for pure hadrons (π, K, p) need to be obtained. From the right panel of Fig. 2.7, we can still see the slow hadron bands in $n\sigma_e$ vs. momentum distribution after the TOF cut. So pure hadron samples can be selected via applying a very tight m^2 ($m^2 = p^2(1/\beta^2 - 1)$) cut provided by TOF and $|n\sigma_h| < 4$ ($h = \pi, K, p$). The 2-D scattering plot of m^2 vs. p_T for hadrons is shown in the left panel of Fig. 3.4 while the right panel shows the m^2 distribution of hadrons, in which the red lines indicate m^2 cuts used to select pure hadron samples. The fittings were made to the $n\sigma_e$ distributions of pure hadron sample in each p_T bin. From the distribution of dE/dx vs. momentum, we can see hadrons have the steep shape at low p_T . After projected to dE/dx axis, the hadron $n\sigma_e$ distributions are not Gaussian. There will be a tail into the electron region. To describe the tail better, we used the new function

$$f(x) = C * \exp\left\{-0.5 * \left(\frac{x - \mu}{\sigma}\right)^2 - \exp\left(-\frac{x - \mu}{\sigma} * \eta\right)\right\} \quad (3.1)$$

instead, where η is a parameter, which can control the hadron tail. The initialization parameters of the mean were obtained from the B70M version of Bichsel function, which

was shown in dE/dx distribution of Fig. 2.5. The $n\sigma_e$ distributions and fitting results of pure π , K and p in $1.10 < p_T < 1.20$ GeV/ c bin are displayed in Fig. 3.5.

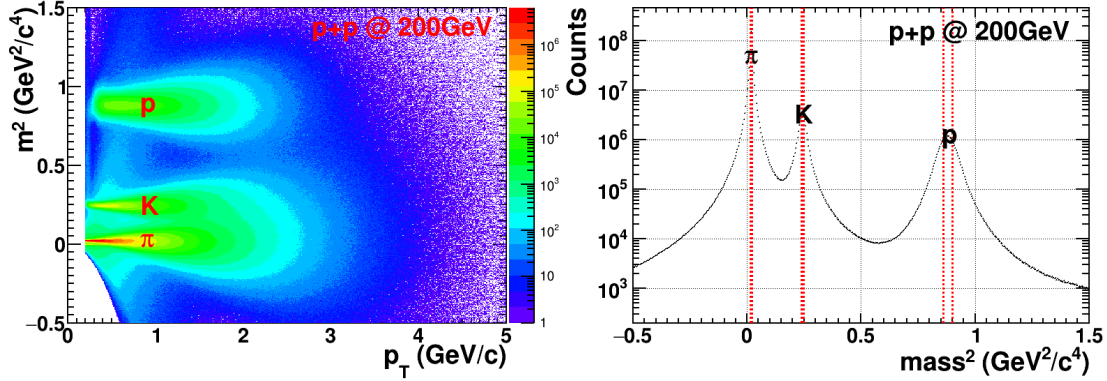


Fig. 3.4 Left panel: m^2 distribution as a function of p_T for hadrons. Right panel: m^2 distribution of hadrons. The red lines show m^2 cuts used to select pure hadron samples.

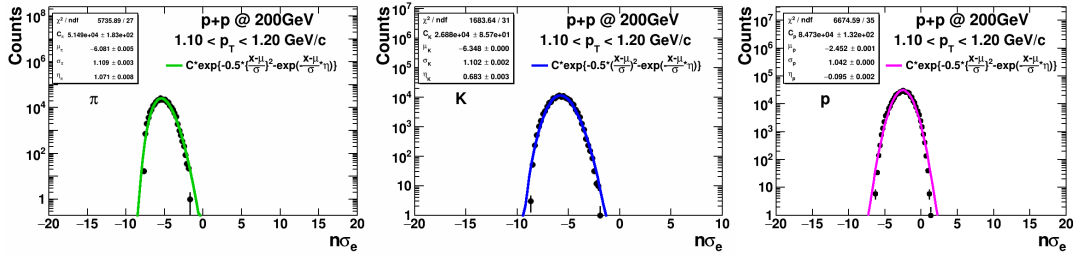


Fig. 3.5 $n\sigma_e$ distributions of pure π , K and p in $1.10 < p_T < 1.20$ GeV/ c bin. The function 3.1 was used to fit these distributions.

Thirdly, using the mean, sigma, eta and their standard deviations from the fittings of $n\sigma_e$ distributions of pure particles, function 3.1 for hadrons and Gaussian function for electrons were used to parameterize the $n\sigma_e$ distributions of identified particles. From the fitting results, we found they were not reliable in overlap p_T bins, where the electron band crosses with the hadron bands. Exponential functions were used to extrapolate the hadron yields into the overlap region. With fixing hadron yields from extrapolated value, we refitted the $n\sigma_e$ distributions at overlapped p_T bins. The final fitting of the $n\sigma_e$ distribution in each p_T bin was obtained and that in $1.50 < p_T < 1.60$ GeV/ c bin is shown in Fig. 3.6.

From the integral calculation of identified particle $n\sigma_e$ distribution at the $n\sigma_e$ cut range of inclusive electrons in each p_T bin, the raw yield of inclusive electrons was obtained. The left panel of Fig. 3.7 shows the raw dN/dp_T distribution of inclusive electrons. Using the fitting function of $n\sigma_e$ distribution of identified particles in each p_T bin, the purity was obtained by taking the ratio of the raw yield of real electrons (red

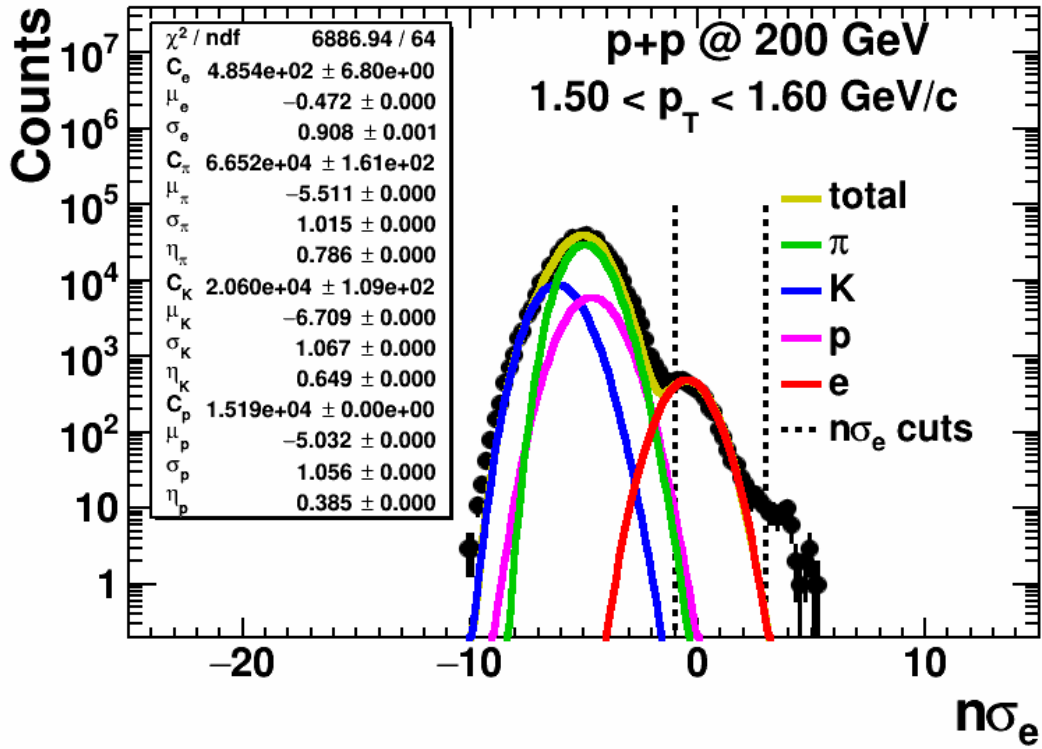


Fig. 3.6 $n\sigma_e$ distribution and its fitting in $1.50 < p_T < 1.60$ GeV/c bin for identified particles. The black dotted lines show the $n\sigma_e$ cut of inclusive electron.

curve) to that of inclusive electrons (yellow curve) at the same $n\sigma_e$ cut range. The right panel of Fig. 3.7 shows the purity of inclusive electrons as a function of p_T . The purity was worse at the overlap region due to hadron contamination.

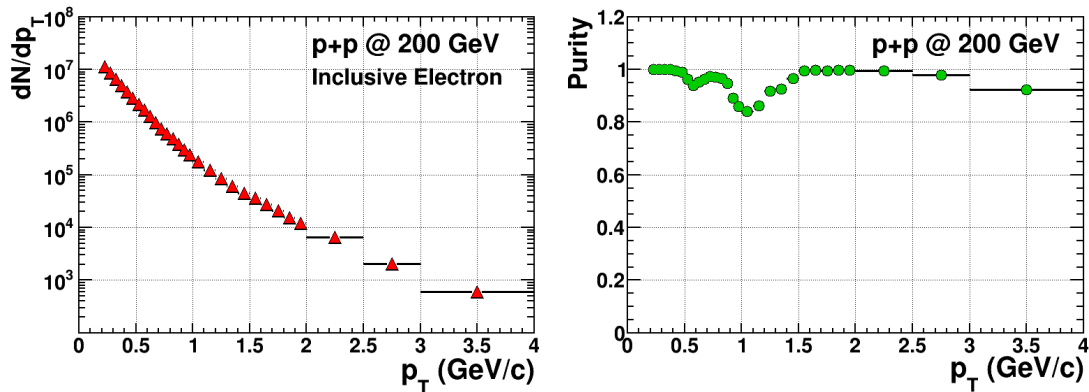


Fig. 3.7 Raw dN/dp_T and purity distributions as a function of p_T for inclusive electrons.

2. Photonic electron cocktail

From the previous measurement [96] and the estimation from the STAR environment, electrons from gamma conversion, π^0 and η Dalitz decays are dominate in the pho-

tonic electrons. Due to a lot of materials in STAR detector, the photonic background electrons mainly come from gamma conversion, especially at low p_T (< 1 GeV/c). In STAR, due to the large acceptance of TPC, photonic background electrons from gamma conversion etc. were experimentally reconstructed making use of topological method according to the previous STAR measurements [97]. That is the photonic electrons were obtained via selecting the invariant mass of e^+e^- pairs. The e^+e^- invariant mass was reconstructed from a tagged electron (positron) from “TPC + TOF/BEMC” combined with other partner positron (electron) reconstructed in the TPC in the same event. The tagged and partner electrons (positrons) need to be requested from global tracks when we searched for e^+e^- pairs. There is the characteristic feature of low invariant mass for the e^+e^- invariant mass from photonic background. So the small value of the invariant mass of e^+e^- pairs was chosen. The cuts of identification for photonic electrons are as follow:

Tagged electron:

- same cuts with inclusive electrons.

Partner electron:

- Global track.
- $Gp_T > 0.3$ GeV/c.
- $nHitsFit \geq 20$.
- $0.52 \leq nHitsFit/nMax \leq 1.2$.
- $-0.5 < n\sigma_e < 3.0$.

e^+e^- pair cuts:

- $M_{e^+e^-} < 0.15$ GeV/c².
- $pairDca < 1.0$ cm: the distance of closest approach between tagged and partner electron helices, to ensure partner track is attached to tagged one.

After these cuts, the distribution of the photonic electron invariant mass in each p_T bin was obtained. But there is the randomly combinatorial background in photonic electron signal. The like-sign method (e^+e^+ , e^-e^-) [98] was used to subtract randomly combinatorial background in this analysis. The left panel of Fig. 3.8 shows the $M_{e^+e^-}$

distribution in $1.50 < p_T < 1.60$ GeV/c bin of photonic electrons. The integral calculation to the distribution of the photonic electron invariant mass with the subtracted combinatorial background in each p_T bin at the range of $M_{e^+e^-}$ cut was used to get the photonic electron raw yield. The raw dN/dp_T of photonic electrons is shown in the right panel of Fig. 3.8.

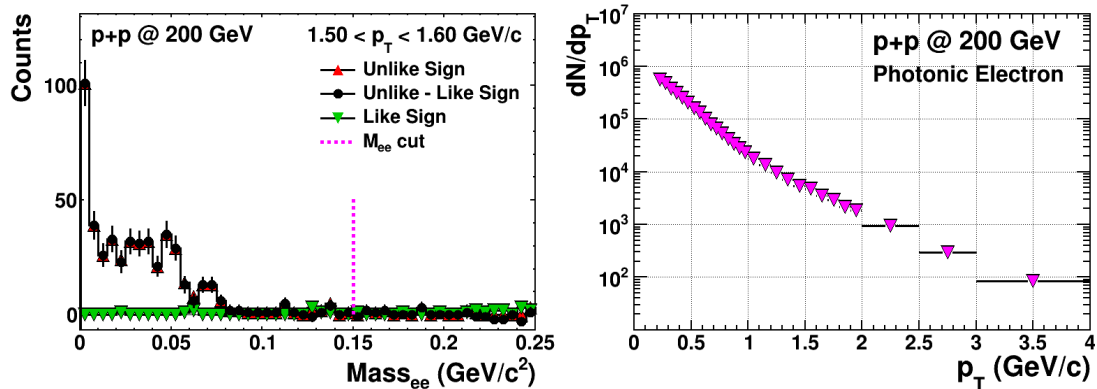


Fig. 3.8 Left panel: Invariant $M_{e^+e^-}$ distribution in $1.50 < p_T < 1.60$ GeV/c bin for photonic electrons. Right panel: Raw dN/dp_T distribution of photonic electrons.

3.1.5. Efficiency and Acceptance

The final yield of NPE need to be corrected for the detector acceptance and efficiency. Because of during the extraction of raw yields for the inclusive electrons and photonic electrons, a part of them were lost attributed to tracking reconstruction, detector acceptance and cut efficiency etc:

- $n\sigma_e$ cut efficiency.
- TOF matching efficiency: track from TPC with good TOF hits matched, TOF acceptance.
- TOF EPID efficiency.
- BEMC matching efficiency: track from TPC with good BEMC hits matched, BEMC acceptance.
- BEMC EPID efficiency.
- Photonic electron reconstruction efficiency.
- TPC tracking efficiency: TPC tracking reconstruction efficiency, TPC acceptance.

The efficiencies must be calculated using the pure electron sample. The $n\sigma_e$ cut efficiency, TOF matching efficiency, TOF EPID efficiency, BEMC matching efficiency and BEMC EPID efficiency were determined from real data. In data, pure electron sample was obtained by photonic electrons with the very small $M_{e^+e^-}$ value: $M_{e^+e^-} < 0.05 \text{ GeV}/c^2$. Certainly, for the efficiency calculation of a cut, a pure electron sample without using this cut in question must be needed. The photonic electron reconstruction efficiency and TPC tracking efficiency were from embedding simulation. It is based on GEANT3 simulation to rebuild full STAR geometry with correct material budget and detectors response. Then the Monte-Carlo (MC) data is embedded in a representative sample of real data and their tracks pass through the full STAR geometry and are reconstructed and calibrated as the ones used in the real data. The embedding was performed using production P12id and library SL12d_embed. Flat p_T spectra, η and ϕ distributions for the Monte-Carlo gamma, π^0 , η and e^+/e^- embedding were used to increase statistics of higher p_T electrons and reduce CPU time.

Table 3.1 Cuts of selecting pure electron sample for tagged electron $n\sigma_e$ cut efficiency calculation.

Tagged electron cuts	Partner electron cuts	Pair cuts
$p_T > 0.2 \text{ GeV}/c$		
$ \eta < 0.7$		
$nHitsFit \geq 20$		
$0.52 < nHitsFit/nMax < 1.2$	$Gp_T > 0.3 \text{ GeV}/c$	
$nHitsDedx \geq 15$	$nHitsFit \geq 20$	$M_{e^+e^-} < 0.05 \text{ GeV}/c^2$
$Gdca < 1.0 \text{ cm}$	$0.52 \leq nHitsFit/nMax \leq 1.2$	$pairDca < 1.0 \text{ cm}$
$TofMatchFlag > 0$	$-0.5 < n\sigma_e < 3.0$	
$\beta > 0$		
$ Y_{local} < 1.8 \text{ cm}$		
$ 1/\beta - 1 < 0.03$		
$-4.0 < n\sigma_e < 3.5$		

1. $n\sigma_e$ cut efficiency

Due to embedding can not reproduce the dE/dx very well. We got the $n\sigma_e$ cut efficiency from data. The obtained $n\sigma_e$ distribution of pure electrons in each p_T bin from data,

which in $1.10 < p_T < 1.20$ GeV/c bin is shown in the left panel of Fig. 3.3, can be used to calculate $n\sigma_e$ cut efficiency:

$$\epsilon = \frac{N \text{ with } n\sigma_e \text{ cut}}{N \text{ without } n\sigma_e \text{ cut}}. \quad (3.2)$$

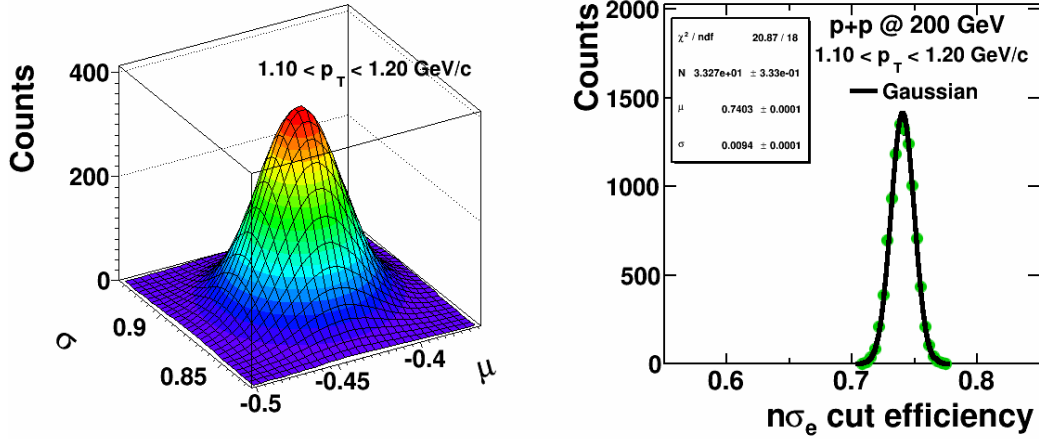


Fig. 3.9 Two-dimensional Gaussian distribution whose parameters from the covariance matrix of Gaussian fitting of pure electron $n\sigma_e$ distribution and $n\sigma_e$ cut efficiency distribution in $1.10 < p_T < 1.20$ GeV/c bin.

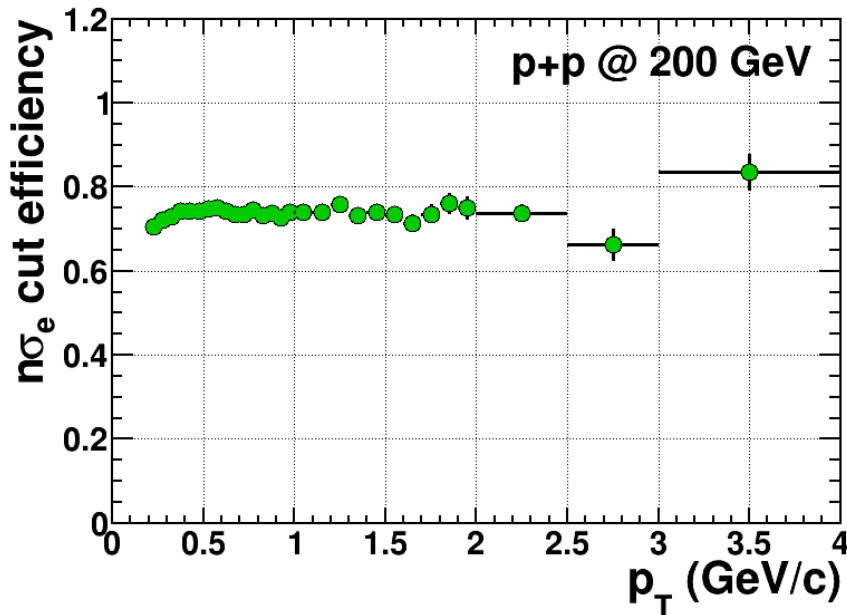


Fig. 3.10 $n\sigma_e$ cut efficiency as a function of p_T .

(1) **Tagged electron $n\sigma_e$ cut efficiency** The cuts of selecting pure electron sample used to calculate tagged electron $n\sigma_e$ cut efficiency are shown in Table 3.1. The Gaussian function was made to fit $n\sigma_e$ distribution in each p_T bin in order to calculate covariance matrix, which includes five parameters: mean and its deviation, sigma and its deviation, and their correlation coefficient. Then we sampled the two-dimensional Gaussian distribution with five parameters just mentioned 10000 times, calculated $n\sigma_e$ cut efficiency according to formula 3.2 and thereby obtained $n\sigma_e$ cut efficiency distributions in different p_T bins. The cut efficiency distribution was fitted by Gaussian function and then the mean was treated as $n\sigma_e$ cut efficiency and the sigma as systematic uncertainty. Fig. 3.9 shows the the two-dimensional Gaussian distribution and $n\sigma_e$ cut efficiency distribution in $1.10 < p_T < 1.20$ GeV/c bin. The $n\sigma_e$ cut efficiency as a function of p_T is shown in Fig. 3.10.

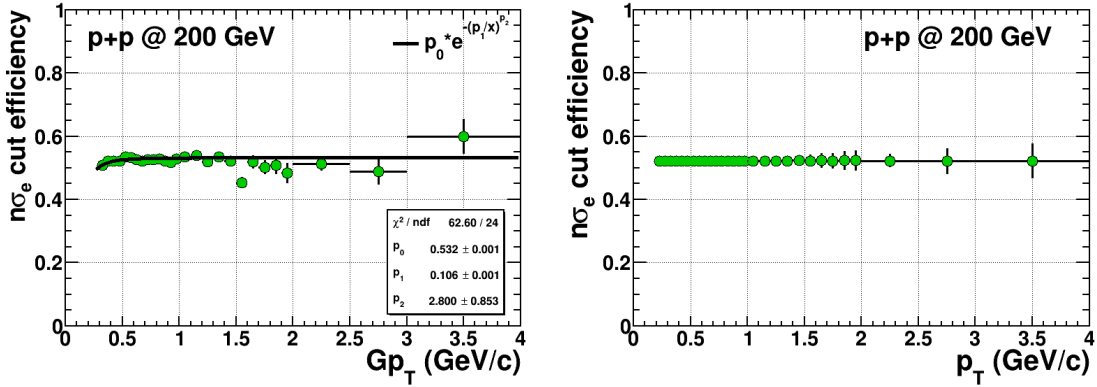


Fig. 3.11 $n\sigma_e$ cut efficiency as a function of Gp_T and tagged electron p_T for partner electron.

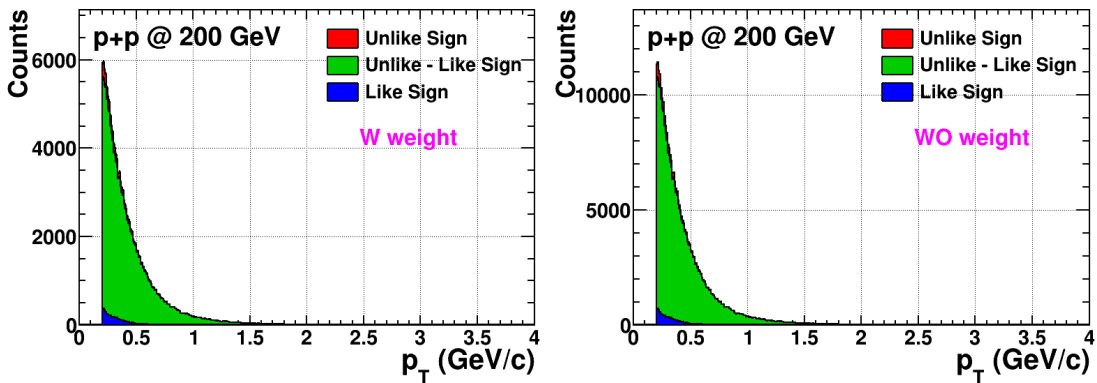


Fig. 3.12 Tagged electron distribution without and with weight, which is from partner electron $n\sigma_e$ cut efficiency as a function of Gp_T .

(2) **Partner electron $n\sigma_e$ cut efficiency** As mentioned in the section of photonic electron cocktail, we used the global tracks when reconstructed the invari-

ant mass of e^+e^- pairs. So the cuts of partner electrons are relative to global tracks. We used the same method as calculating tagged electron $n\sigma_e$ cut efficiency to get partner electron $n\sigma_e$ cut efficiency. The left panel of Fig. 3.11 shows $n\sigma_e$ cut efficiency as a function of partner electron Gp_T . However, when subtracting the photonic electrons (tagged electrons) from inclusive electrons, the tagged electron cuts are relative to primary tracks. So in order to apple-to-apple efficiency correction of photonic electrons, we must use the partner electron $n\sigma_e$ cut efficiency as a function of tagged electron p_T . The $n\sigma_e$ cut efficiency of partner electrons as a function of tagged electron p_T can be calculated as:

$$\epsilon = \frac{N_{\text{tagged electron with wt.}}}{N_{\text{tagged electron without wt.}}} \quad (3.3)$$

where wt. is from the fitting function of $n\sigma_e$ cut efficiency as a function of Gp_T of partner electrons paired with tagged electrons. The tagged electron distribution with and without weight, and partner electron $n\sigma_e$ cut efficiency as a function of tagged electron p_T are shown in Fig. 3.12 and the right panel of Fig. 3.11, respectively. The weight difference from the counts and fitting of $n\sigma_e$ cut efficiency as a function of Gp_T was as the systematic uncertainty of partner electron $n\sigma_e$ cut efficiency.

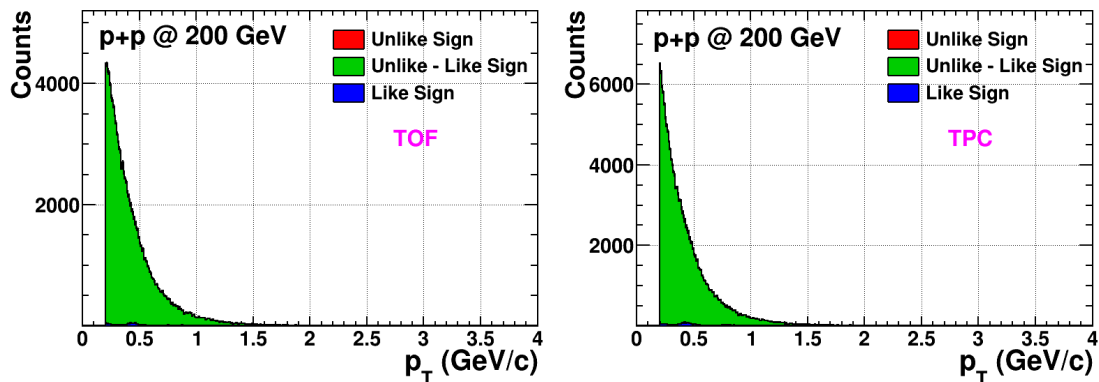


Fig. 3.13 Number of electron tracks matched to TOF and number of electron tracks in TPC passed the track quality and acceptance cuts.

2. TOF Matching and EPID efficiencies

The TOF matching efficiency was obtained by taking the ratio of the number of tracks matched to TOF and the number of tracks in TPC passed the track quality and acceptance cuts using pure electron sample. A track matched to a TOF hit requires:

- The track projected to TOF has a hit in corresponding TOF cell.

- The distance of track hit position in TOF and TOF cell center in local Y direction is less than 1.8 cm.

The TOF matching efficiency was defined as:

$$\epsilon = \frac{N_{\text{matched}}(TofMatchFlag > 0 \&\& \beta > 0 \&\& |Y_{\text{local}}| < 1.8 \text{ cm})}{N_{TPC}}. \quad (3.4)$$

Fig. 3.13 shows the number of electron tracks matched to TOF and number of electron tracks in TPC passed the track quality and acceptance cuts used to calculate TOF matching efficiency. Meanwhile the TOF matching efficiency as a function of p_T is shown in Fig. 3.14.

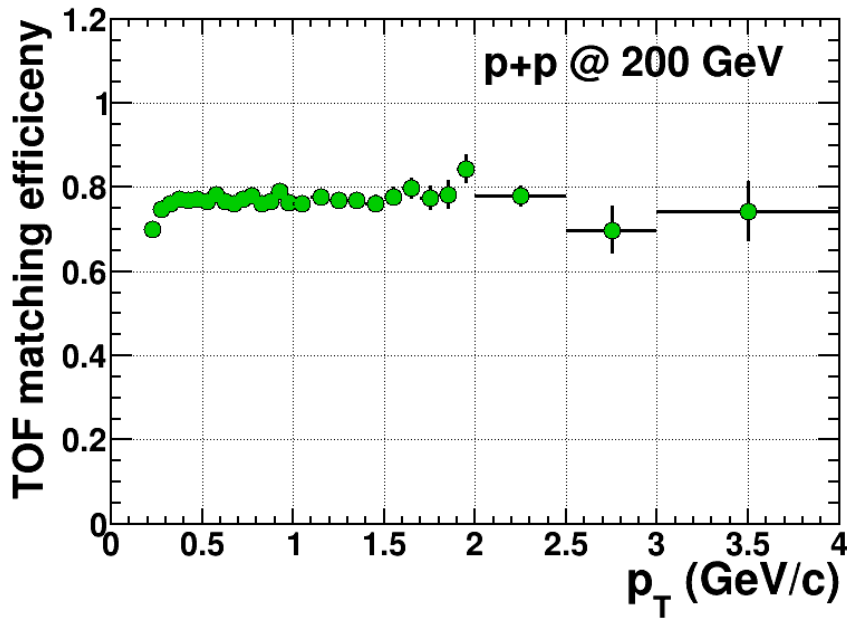


Fig. 3.14 TOF matching efficiency as a function of p_T .

The TOF EPID efficiency was calculated using $1/\beta$ distribution of pure electrons in each p_T bin:

$$\epsilon = \frac{N \text{ with } 1/\beta \text{ cut}}{N \text{ without } 1/\beta \text{ cut}}. \quad (3.5)$$

The $1/\beta$ distribution of electrons in $1.10 < p_T < 1.20$ GeV/c bin is shown in the left panel of Fig. 3.15. The Gaussian function was made to fit this distribution in order to get mean and sigma. Then the parameterized mean and sigma were used to calculate the TOF EPID efficiency. The right panel of Fig. 3.15 shows the TOF EPID efficiency as a function of p_T .

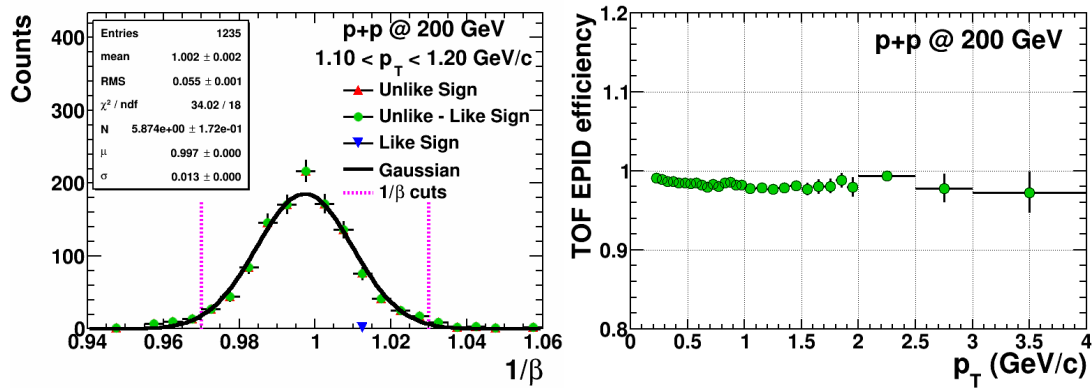


Fig. 3.15 Left panel: $1/\beta$ distribution in $1.10 < p_T < 1.20$ GeV/c bin. The Gaussian function was used to fit this distribution. The pink lines show the $1/\beta$ cuts. Right panel: TOF EPID efficiency as a function of p_T .

3. BEMC Matching and EPID efficiencies

The BEMC matching efficiency was obtained by taking the ratio of the number of tracks matched to BEMC and the number of tracks in TPC passed the track quality and acceptance cuts using pure electron sample. A track matched to a BEMC hit requires:

- The track passing BEMC has energy deposition in BEMC tower.

The BEMC matching efficiency was defined as:

$$\epsilon = \frac{N_{\text{matched}}(E > 0)}{N_{\text{TPC}}}. \quad (3.6)$$

Electron candidates in the TPC are projected to the BEMC and matched to an energy cluster to determine their momentum-to-energy ratio p/E . The BEMC EPID efficiency was obtained by taking the ratio of the number of tracks with BEMC EPID cut and the number of tracks matched to BEMC passed the track quality and acceptance cuts using pure electron sample. The BEMC EPID efficiency was defined as:

$$\epsilon = \frac{N(0.3 < p/E < 1.5)}{N_{\text{matched}}(E > 0)}. \quad (3.7)$$

Fig. 3.16 shows the number of electron tracks with BEMC EPID cut, number of electron tracks matched to BEMC, number of electron tracks in TPC. And the BEMC matching and EPID efficiencies as function of p_T are shown in Fig. 3.17.

4. Photonic electron reconstruction efficiency

The photonic electrons are from γ conversion, π^0 and η Dalitz decays. So the photonic electron reconstruction efficiency is a combined one of individual efficiency from γ

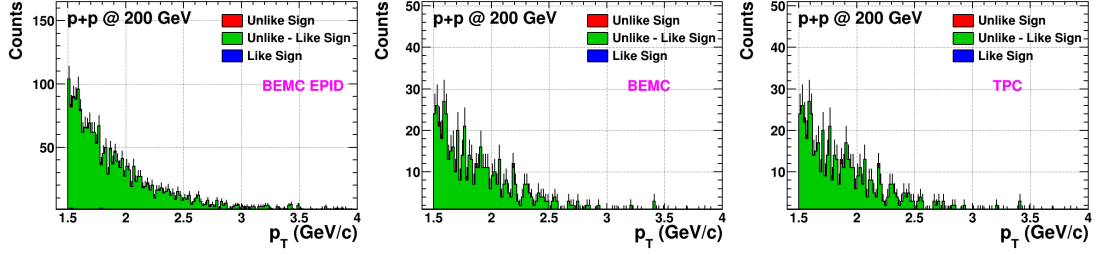


Fig. 3.16 Number of electron tracks with BEMC EPID cut ($0.3 < p/E < 1.5$), number of electron tracks matched to BEMC, number of electron tracks in TPC passed the track quality and acceptance cuts.

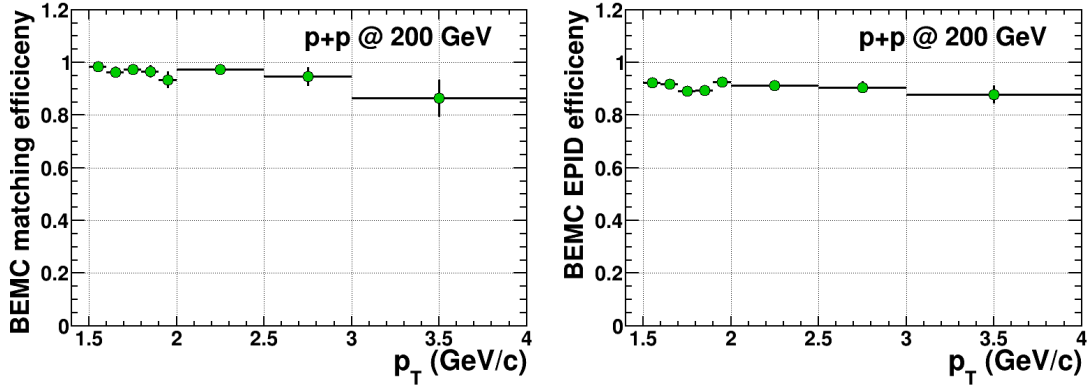


Fig. 3.17 BEMC matching and EPID efficiency as a function of p_T .

conversion, π^0 and η Dalitz decays. The photonic electron reconstruction efficiency can be calculated as:

$$\epsilon_{combined} = \sum_i \epsilon_i * RC_i(i = \gamma, \pi^0, \eta), \quad (3.8)$$

where RC_i is their individual relative contribution from γ conversion, π^0 and η Dalitz decays to photonic electrons, ϵ_i is their individual photonic electron reconstruction efficiency. In the next two subsections, the detailed information about RC_i and ϵ_i calculations will be introduced, respectively.

(1) **Efficiency** Using the γ conversion, π^0 and η Dalitz decay embedding data, the photonic electron reconstruction efficiency can be calculated as:

$$\epsilon_i = \frac{N_{rc}(tagged\ electron\ cuts + partner\ electron\ cuts + pair\ cuts)}{N_{rc}(tagged\ electron\ cuts)}. \quad (3.9)$$

But the input p_T shapes for MC photonic sources in embedding are flat. So the original γ , π^0 and η meson p_T spectra need be used to weight input p_T in embedding when calculating the reconstruction efficiency. The published invariant yields of π^0 ($(\pi^+ + \pi^-)/2$) [99–101] and η mesons [102] along with the fitting of Tsallis function

are shown in the top-left panel of Fig. 3.18. They were used to weight the embedded parents π^0 and η mesons. For inclusive γ p_T spectrum, it was extracted via decaying π^0 and η mesons into γ through PYTHIA. The following algorithm was used in the PYTHIA decaying process:

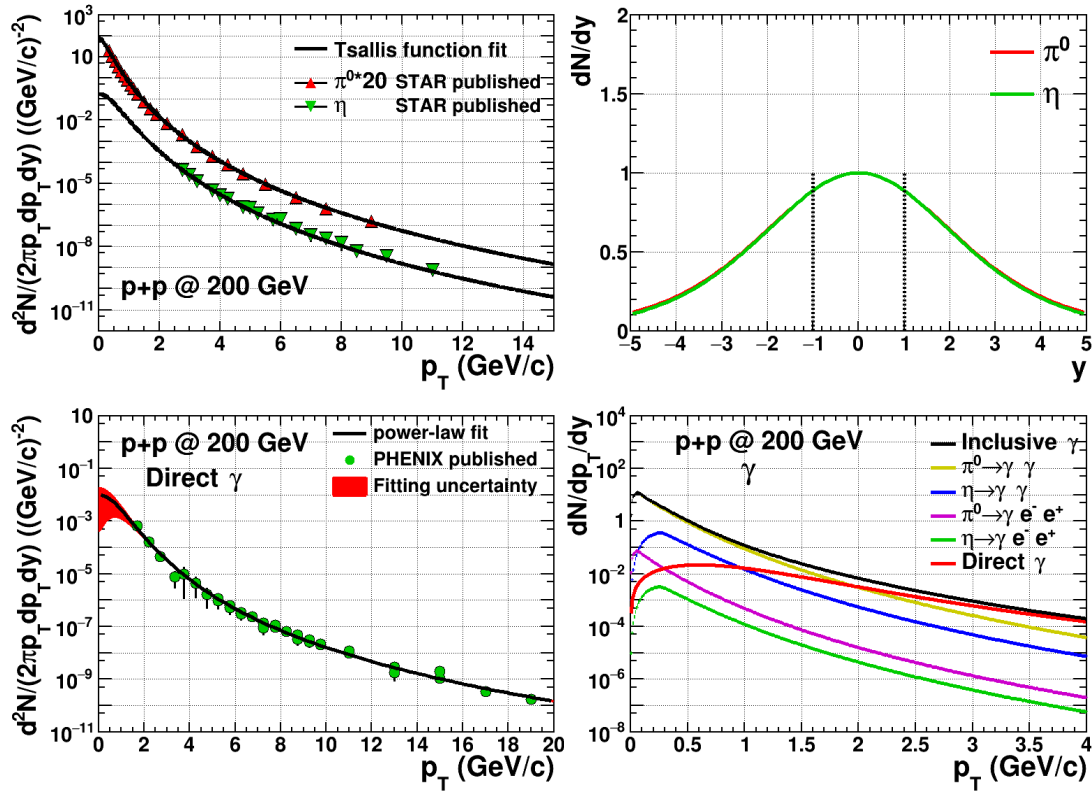


Fig. 3.18 Top-left panel: Invariant yield distributions of π^0 and η mesons. The Tsallis functions were used to fit those distributions. Top-right panel: dN/dy as a function of y for π^0 and η mesons. Bottom-left panel: Direct γ invariant yield distribution. The power-law was used to fit this distribution. Bottom-right panel: Inclusive γ p_T spectrum along with those from different sources.

- Generate Monte-Carlo π^0/η meson with ϕ sampled from uniform distribution in $0 \sim 6.28$ range and with $(p_T, \text{rapidity}(y))$ sampled from measured or calculated π^0/η dN/dp_T and dN/dy vs. y of π^0/η (shown in the top-right panel of Fig. 3.18).
- Simulate $\pi^0/\eta \rightarrow e^+ e^- \gamma/\gamma\gamma$ for generated mesons using PYTHIA decay routine.
- Fill η of generated γ in histogram $hGammaEta$.
- Fill p_T of generated γ within the desired $\Delta\eta$ acceptance in histogram $hGammaPt$.
- Integral of π^0/η dN/dy gives N .

- Normalize integral of histogram $hGammaEta$ to $N/2N$ (Dalitz decay/Two gamma decay).
- Integral of $hGammaEta$ in the desired $\Delta\eta$ gives ΔN .
- Normalize integral of $hGammaPt$ to ΔN .
- Divide $hGammaPt$ by $\Delta\eta$ to get $dN/dp_T d\eta$ of γ from π^0/η .

Following the above process, the γ spectra from π^0 and η meson decays were obtained. In addition, the direct γ contribution to inclusive γ need to be considered, which is from PHENIX $p + p$ results fitted by the power-law function [103–105]. The invariant yield of direct γ is shown in the bottom-left panel of Fig. 3.18. The inclusive γ p_T spectrum was obtained by summing π^0 and η mesons decayed and direct ones, which are shown in the bottom-right panel of Fig. 3.18. The obtained $d^2N/dp_T/dy$ distribution of γ was directly used to weight the embedded parents γ . The obtained reconstruction efficiencies as a function of p_T for γ conversion, π^0 and η Dalitz decays are shown in the right panel of Fig. 3.19.

(2) **Relative contribution** Now we need to consider relative contributions from γ conversion, π^0 and η Dalitz decays to photonic electrons. The electron tracks passed the tagged electron cuts from γ conversion, π^0 and η Dalitz decay embedding sample were recorded and normalized by the dN/dy of inclusive γ , dN/dy and branch ratio of π^0 and η mesons, respectively. The relative contributions were obtained by taking the ratio of these electrons from different sources to their summing one. The left panel of Fig. 3.19 shows the relative contributions as a function of p_T from different sources.

The combined reconstruction efficiency was obtained using formula 3.8. The right panel of Fig. 3.19 shows the combined reconstruction efficiency as a function of p_T .

5. TPC tracking efficiency

Using the electron/positron embedding data, the TPC tracking efficiency can be calculated as:

$$\epsilon = \frac{N_{rc}(nHitsFit \geq 20, 0.52 < nHitsFit/nMax < 1.2, nHitsDedx \geq 15, Gdca < 1.0 \text{ cm})}{N_{mc}}. \quad (3.10)$$

But due to the momentum resolution and energy loss are different in embedding and

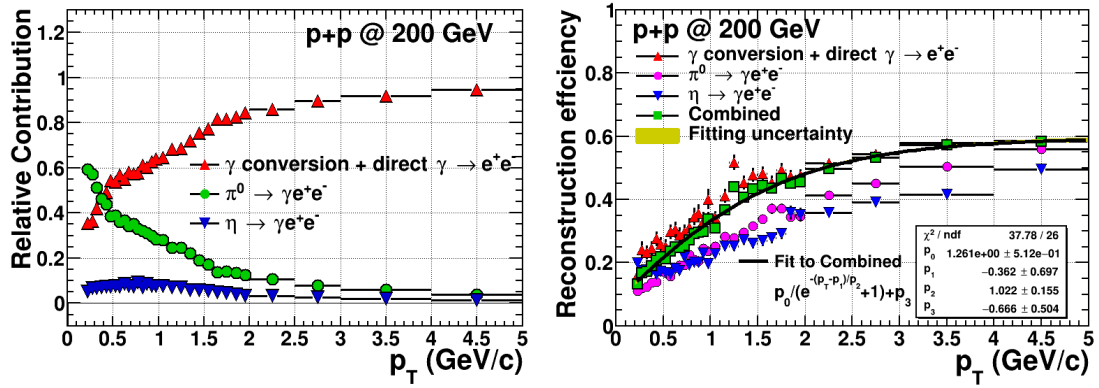


Fig. 3.19 Left panel: Relative contributions from gamma conversion, π^0 and η Dalitz decays to photonic electrons as a function of p_T . Right panel: Combined reconstruction efficiency as a function of p_T , along with the individual efficiencies from γ conversion, π^0 and η Dalitz decays.

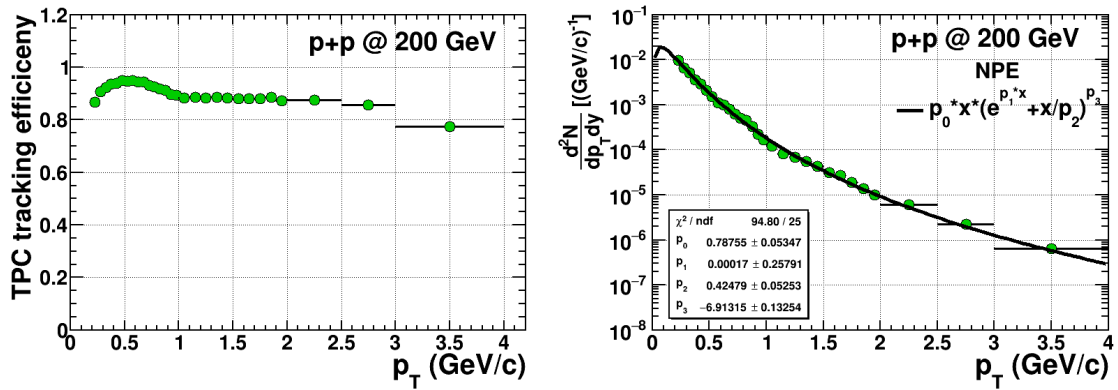


Fig. 3.20 Left panel: TPC tracking efficiency as a function of p_T without p_T smearing effect. Right panel: NPE p_T spectrum. A function $p_0 * x * (e^{p_1 * x} + x/p_2)^{p_3}$ was used to fit this distribution.

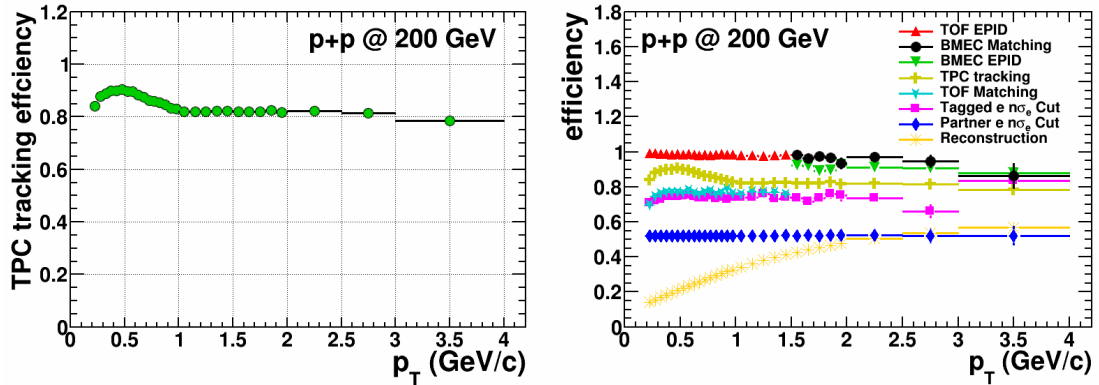


Fig. 3.21 Left panel: TPC tracking efficiency as a function of p_T with p_T smearing effect. Right panel: All efficiencies as a function of p_T .

data. We need consider the real momentum resolution to embedding. The σ_{p_T}/p_T distribution, which was obtained from the embedding sample, was used to measure momentum resolution. It was assumed to follow:

$$(\sigma_{p_T}/p_T)^2 = (a \times p_T)^2 + \left(\frac{b}{\beta}\right)^2 \quad \left(\beta = \frac{p}{E} \frac{p_T}{\sqrt{p_T^2 + m^2}}\right). \quad (3.11)$$

Then we tuned the parameters (a, b) to get the best matching to the J/Ψ mass distribution of data [106]. The final σ_{p_T}/p_T distribution was used to get the real reconstructed p_T in embedding. Similarly, the momentum resolution also have been considered when we calculated the reconstruction efficiency of photonic electron and K_{e3} (section 3.1.6).

Furthermore, to correct TPC tracking efficiency for p_T smearing effect, we used the iteration method to get the TPC tracking efficiency. Firstly, the TPC tracking efficiency without p_T smearing effect was obtained and is shown in the left panel of Fig. 3.20. Then after all efficiency correction, the p_T spectrum of NPE was obtained and fitted by function $p_0 * x * (e^{p_1*x} + x/p_2)^{p_3}$, which was used for next iteration and is shown in the right panel of Fig. 3.20. With sufficient iteration, the parameters of this fit function was invariant and the final TPC track efficiency was obtained, which is shown in the left panel of Fig. 3.21. All efficiencies as a function of p_T used to correct the NPE raw yield are shown in the right panel of Fig. 3.21.

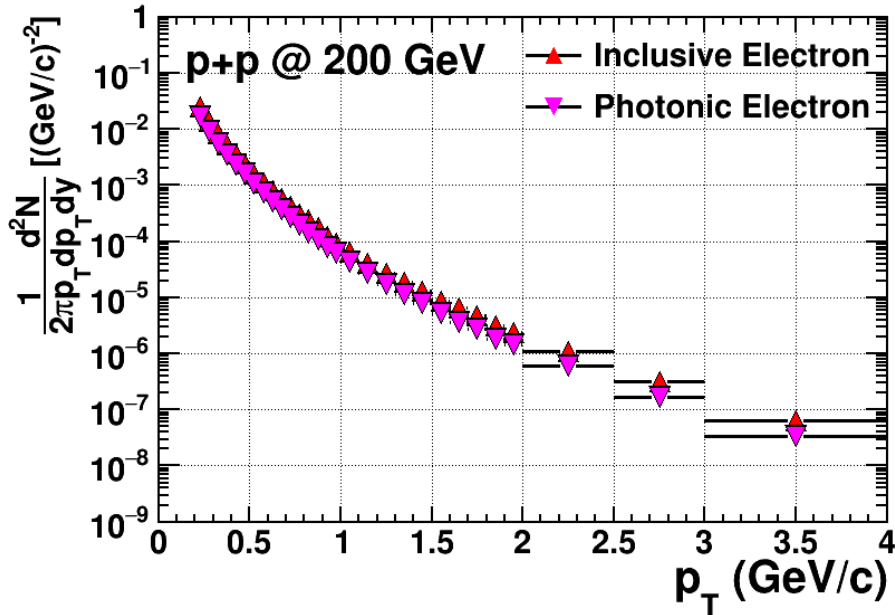


Fig. 3.22 Invariant yield distributions of inclusive and photonic electrons.

3.1.6. Background subtraction

After all efficiency correction, the invariant yields of inclusive and photonic electrons were obtained and are shown in the Fig. 3.22. As mentioned in section 3.1.1, in order to obtain the signal of “non-photonic” electrons from heavy-flavor decays, the “non-photonic” background must be subtracted.

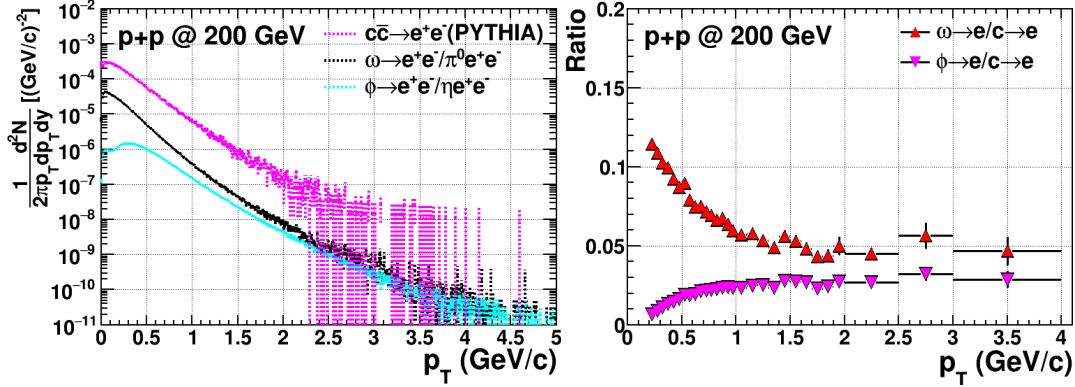


Fig. 3.23 Invariant yield distributions of $\omega \rightarrow e$, $\phi \rightarrow e$ and $c \rightarrow e$. **Right panel: Ratios of $\omega \rightarrow e$ and $\phi \rightarrow e$ than $c \rightarrow e$ as a function of p_T .**

1. Di-electron decays of vector mesons

In this section, we will discuss the di-electron decays of vector mesons and mainly consider ω and ϕ contribution. The same method as di-electron cocktail studying [107] was used. The algorithm is at the below:

- Get $M_{e^+e^-}$ spectra and invariant yields of $\omega \rightarrow e^+e^-/\pi^0 e^+e^-$ and $\phi \rightarrow e^+e^-/\eta e^+e^-$ from simulation:
 - Use the Tsallis function fittings from measured invariant yields of ω and ϕ as input to a detector simulation.
 - The particles are decayed into di-electrons with the appropriate branch ratio by using the formula:

$$\frac{dN}{dM_{e^+e^-}} \propto \sqrt{1 - \frac{4m_e^2}{M_{e^+e^-}^2}} \left(1 + \frac{2m_e^2}{M_{e^+e^-}^2}\right) \frac{1}{M_{e^+e^-}} \left(1 - \frac{M_{e^+e^-}^2}{M_h^2}\right)^3 |F(M_{e^+e^-})|^2. \quad (3.12)$$

- Get $M_{e^+e^-}$ spectrum and invariant yield of $c\bar{c}$ (charm and anti-charm quark) $\rightarrow e^+e^-$ using PYTHIA6.416.
- Require $|y_{e^+e^-}| < 1$, $|\eta_e| < 0.7$, $p_T(e) > 0.2$ GeV/c and $M_{e^+e^-} > 0.15$ GeV/c.
- Normalize $M_{e^+e^-}$ spectra (only checked our result with the published one [107]) and invariant yields using the dN/dy and branch ratio of ω , ϕ and c .

The invariant yields of $\omega \rightarrow e$, $\phi \rightarrow e$ and $c \rightarrow e$ from simulation are shown in the left panel of Fig. 3.23. According to the invariant yields, the ratios of electrons from ω and ϕ decays than charm quark hadrons decay to electrons were obtained, which are shown in the right panel of Fig. 3.23.

2. K_{e3} contribution

The K_{e3} is from K^\pm and K_L^0 decays:

- K^\pm ($c_\tau = 3.711 m$) $\rightarrow e^\pm \pi^0 \nu_e$ (5.07 ± 0.04)%
- K_L^0 ($c_\tau = 15.34 m$) $\rightarrow e^\pm \pi^\mp \nu_e$ (40.55 ± 0.11)%

The K_{e3} was studied based on MB 200 GeV $p + p$ collisions PYTHIA simulation. Meanwhile the electron/positron tracks were selected within STAR acceptance. The tune preset in PYTHIA is “320” [108]. The c_τ of K_S^0 is 2.6844 cm, but its branch ratio is only $(7.04 \pm 0.08) \times 10^{-4}$. So its contribution is neglected in PYTHIA.

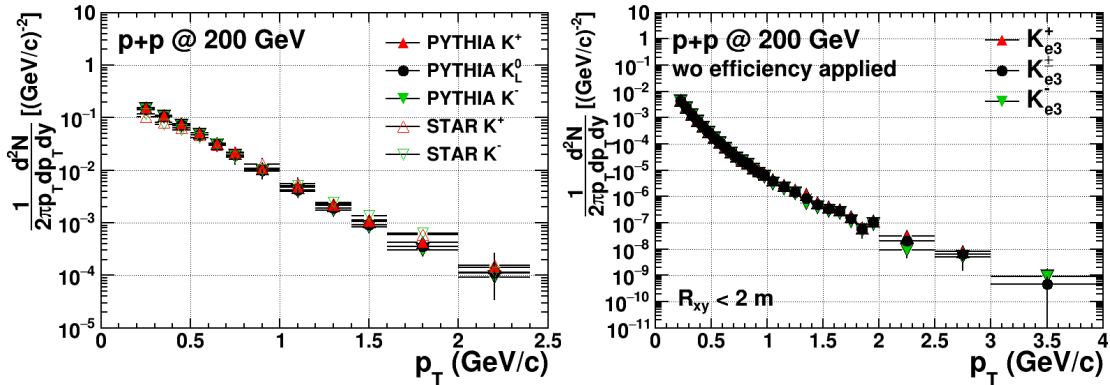


Fig. 3.24 Left panel: Invariant yields of K^+ , K^- and K_L^0 from MB 200 GeV $p + p$ collisions based on PYTHIA simulation, along with STAR published results of K^+ and K^- . Right panel: Invariant yields for K_{e3}^+ and K_{e3}^- from PYTHIA simulation after K^+ and K^- yield correction, along with combined one.

The left panel of Fig. 3.24 shows the invariant yields of K^+ , K^- and K_L^0 from MB 200 GeV $p + p$ collisions based on PYTHIA simulation, comparing with STAR published results [109]. As we can see there is some difference between them. So we took their ratios as a weight to correct the invariant yields of K_{e3}^+ , K_{e3}^- and K_{e3}^0 from PYTHIA simulation. The right panel of Fig. 3.24 shows the invariant yields of K_{e3}^+ and K_{e3}^- from PYTHIA simulation after K^+ and K^- yield correction, along with the K_{e3}^\pm one. The TPC tracking efficiency is different between NPE and K_{e3} because of their different decay length. For K_{e3} , the TPC tracking efficiency is called the reconstruction

efficiency, which was obtained from K_{e3}^+ and K_{e3}^- embedding using the same method as NPE TPC tracking efficiency calculation. The left panel of Fig. 3.25 shows the reconstruction efficiency of K_{e3}^\pm fitted by a function $p_0/(e^{-(p_T-p_1)/p_2}+1)+p_3$. Utilizing the invariant yields of K_{e3}^\pm and its reconstruction efficiency, we can get the yield of K_{e3}^\pm , which is shown in the right panel of Fig. 3.25, was used to subtract K_{e3}^\pm contribution from the NPE invariant yield before TPC tracking efficiency correction. This method is called the direct one.

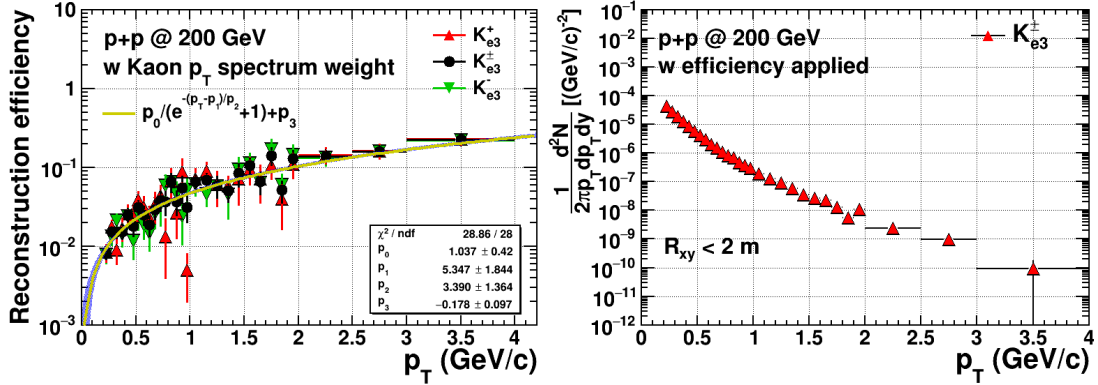


Fig. 3.25 Left panel: Reconstruction efficiency of K_{e3}^\pm as a function of p_T , along with that of K_{e3}^+ and K_{e3}^- . Right panel: Invariant yield for K_{e3}^\pm from PYTHIA simulation with the K_{e3}^\pm reconstruction efficiency applied.

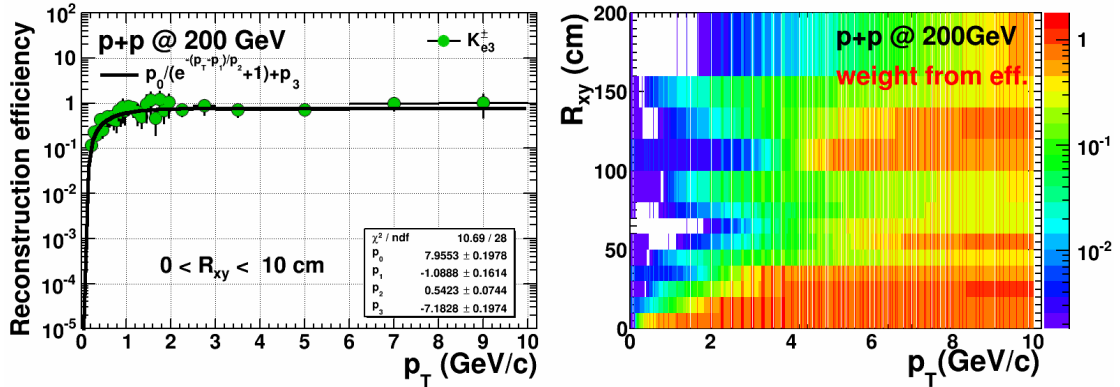


Fig. 3.26 Left panel: Reconstruction efficiency of K_{e3}^\pm as a function of p_T in $0 < R_{xy} < 10 \text{ cm}$ bin. A function $p_0/(e^{-(p_T-p_1)/p_2}+1)+p_3$ was used to fit this distribution. Right panel: Reconstruction efficiency of K_{e3}^\pm as a function of p_T and R_{xy} .

For the K_{e3}^0 contribution, we used the indirect method to get it due to there is not K_{e3}^0 embedding. The reconstruction efficiencies of K_{e3}^\pm in different TPC radius R_{xy} were obtained from embedding, one of which is shown in the left panel of Fig. 3.26. The reconstruction efficiency of K_{e3}^\pm as a function of p_T and R_{xy} , shown in the right panel of Fig. 3.26, was taken as the weight to correct the K_{e3}^0 from PYTHIA simulation. To

validate the method, the same procedure was used to K_{e3}^+ and K_{e3}^- . Then we found the result from these two methods is consistent with each other. The final invariant yield of K_{e3} as a function of p_T , along with that of K_{e3}^\pm and K_{e3}^0 , is shown in the left panel of Fig. 3.27. And the ratio of K_{e3} yield to NPE is shown in the right of Fig. 3.27. As we can see, the contribution is very small.

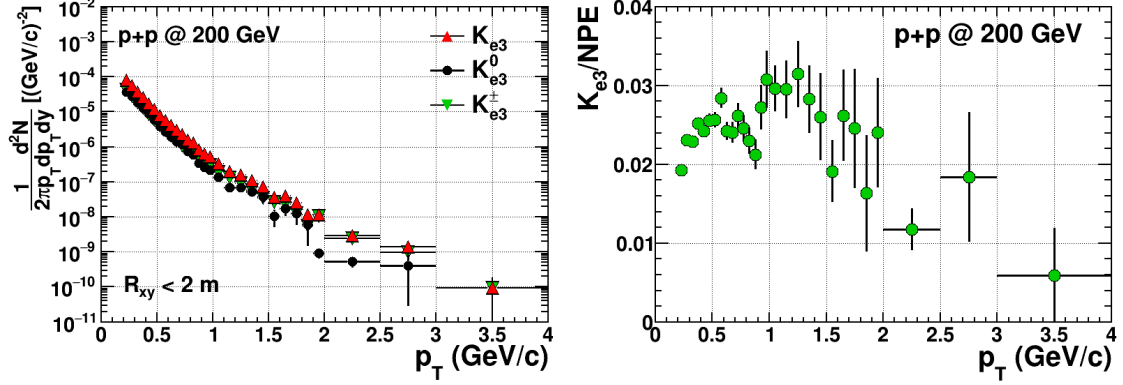


Fig. 3.27 Left panel: Invariant yield of K_{e3} as a function of p_T , along with that of K_{e3}^\pm and K_{e3}^0 . Right panel: Ratio of K_{e3} yield to NPE as a function of p_T .

3.1.7. Trigger/Vertex bias correction

In our analysis, the event selections required a VPD coincidence and a valid primary vertex finding. So the measured NPE cross-section should be calculated as:

$$\begin{aligned}
 E \frac{d^3\sigma}{d^3p} &= \frac{1}{L} \frac{1}{2\pi p_T dp_T dy} \frac{N_{NPE}^{raw}}{\epsilon_{NPE}^{track_level} \epsilon_{NPE}^{VPD_coincidence} \epsilon_{NPE}^{GoodVetex}} \\
 &= \frac{\sigma_{NSD}}{\frac{N_{MB}^{VPD_coincidence\&\&GoodVetex}}{\epsilon_{MB}^{VPD_coincidence} \epsilon_{MB}^{GoodVetex}}} \frac{1}{2\pi p_T dp_T dy} \frac{N_{NPE}^{raw}}{\epsilon_{NPE}^{track_level} \epsilon_{NPE}^{VPD_coincidence} \epsilon_{NPE}^{GoodVetex}} \\
 &= \frac{\sigma_{NSD}}{N_{MB}^{VPD_coincidence\&\&GoodVetex}} \frac{1}{2\pi p_T dp_T dy} \frac{N_{NPE}^{raw}}{\epsilon_{NPE}^{track_level}} \frac{\epsilon_{MB}^{VPD_coincidence} \epsilon_{MB}^{GoodVetex}}{\epsilon_{NPE}^{VPD_coincidence} \epsilon_{NPE}^{GoodVetex}} \\
 &= \frac{\sigma_{NSD}}{N_{MB}^{VPD_coincidence\&\&GoodVetex}} \frac{1}{2\pi p_T dp_T dy} \frac{N_{NPE}^{raw}}{\epsilon_{NPE}^{track_level}} f_{trigger/vetex_bias},
 \end{aligned} \tag{3.13}$$

where L is the luminosity and σ_{NSD} is the non-singly diffractive (NSD) cross section, which is obtained by $\sigma_{inel}^{pp}/R_\sigma$. The pp inelastic cross section $\sigma_{inel}^{pp} = 42 \text{ mb}$ [110] and the factor $R_\sigma = 1.4$. Due to the VPD coincidence and valid primary vertex finding are both different between NPE event and MB event. This causes the trigger/vertex bias (last fraction of the above formula) of NPE event because we used MB data to study NPE cross-section. Because of the VPD limited acceptance, NPE event has more tracks at the mid-rapidity than MB event. Thus the VPD coincidence efficiency of NPE event

is lower than that of MB event caused by the corresponding forward tracks of NPE event are less. Meanwhile because at least one electron track in NPE event is required to reconstructed primary vertex track. The vertex finding efficiency of NPE event is higher than that of MB event. In this analysis, trigger bias correction factor was taken from [107], the number is 64% with 8% systematic uncertainty.

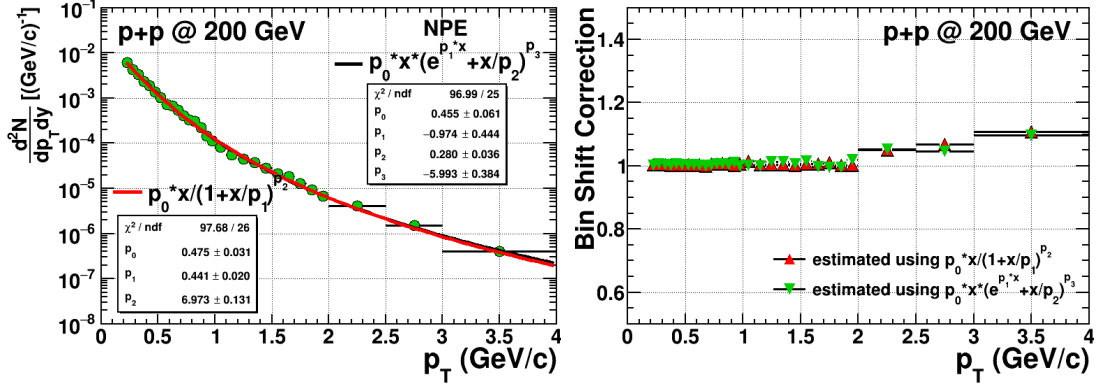


Fig. 3.28 Left panel: NPE p_T spectrum without bin shift correction, along with two different function fittings. Right panel: Bin shift correction factors as a function of p_T from two different function fittings.

3.1.8. Bin shift correction

Due to poor statistics at the higher p_T , the wide bins were used to measure the p_T spectrum. Because of the p_T spectrum is not flat instead of having a variation in rate, the bin center value is not the real data point which is in barycentre position. So we need consider the bin shift correction. Instead of bin center value shift, the bin content shift was used to correct p_T spectrum. The specific process is at the below:

- Use function to fit NPE p_T spectrum (shown in the left panel of Fig. 3.28).
- Randomly sample this function and then fill in histogram with the same bin width as in data.
- Normalize the function into 1.0.
- Scale the histogram by $1/n_{sample}/bin_width$.

The correction factor was calculated as:

$$corr = N_{histogram}/N_{function}, \quad (3.14)$$

which is shown in the right panel of Fig. 3.28. The systematic uncertainty was estimated using two different function fittings. Then NPE cross-section need to be divided by this correction factor.

3.1.9. Systematic uncertainties

The systematic uncertainties for NPE have four primary sources: cuts, electron purity extraction, efficiency and non-phonotic background subtraction.

1. Cuts

If cuts are changed, it effects not only on the raw yield of NPE but also on the TPC tracking and photonic electron reconstruction efficiency. Fig. 3.29 shows the $nHitsFit$, $nHitsDedx$ and $Gdca$ distributions for NPE, Gp_T and $nHitsFit$ distributions for partner electrons of photonic electrons, and M_{e+e-} distribution for photonic electrons in $0.20 < p_T < 0.25$ GeV/c bin from embedding and data. As we can see, there is some discrepancy about these distributions in embedding and data. So the lost (gain) fraction from $cut1$ to $cut2$ in embedding is different from data. Then the difference between embedding and data was taken as the systematic uncertainty. We studied these distributions in p_T volume.

The dA was defined the unit area under these distributions and the total integrated area of these distributions was A . Then taking the $nHitsFit$ cut as example, the TPC tracking efficiency under the different $nHitsFit$ cuts can be calculated as:

$$Ef f_{nHitsFit_cut1}^{emb.} = \frac{\int_{nHitsFit_cut1}^{nHitsFit_max} dA}{A}; Ef f_{nHitsFit_cut2}^{emb.} = \frac{\int_{nHitsFit_cut2}^{nHitsFit_max} dA}{A}. \quad (3.15)$$

Thus the relative uncertainty was:

$$\sigma_{nHitsFit} = \frac{\int_{nHitsFit_cut1}^{nHitsFit_max} dA_{data} / Ef f_{nHitsFit_cut1}^{emb.}}{\int_{nHitsFit_cut2}^{nHitsFit_max} dA_{data} / Ef f_{nHitsFit_cut2}^{emb.}}. \quad (3.16)$$

The relative uncertainty was applied to the NPE spectrum to extract the systematic uncertainty of $nHitsFit$ cut. The relative uncertainties of other distributions mentioned at the beginning of this section were estimated in the same way. Fig. 3.30 shows their respective relative uncertainties as a function of p_T . For the $nHitsFit$, $nHitsDedx$ and $Gdca$ distributions of NPE, they couldn't be obtained in data. The distributions were obtained from pure electron sample via selecting photonic electrons. But the $nHitsFit$, $nHitsDedx$ and $Gdca$ distributions strongly depend on where the conversion point is.

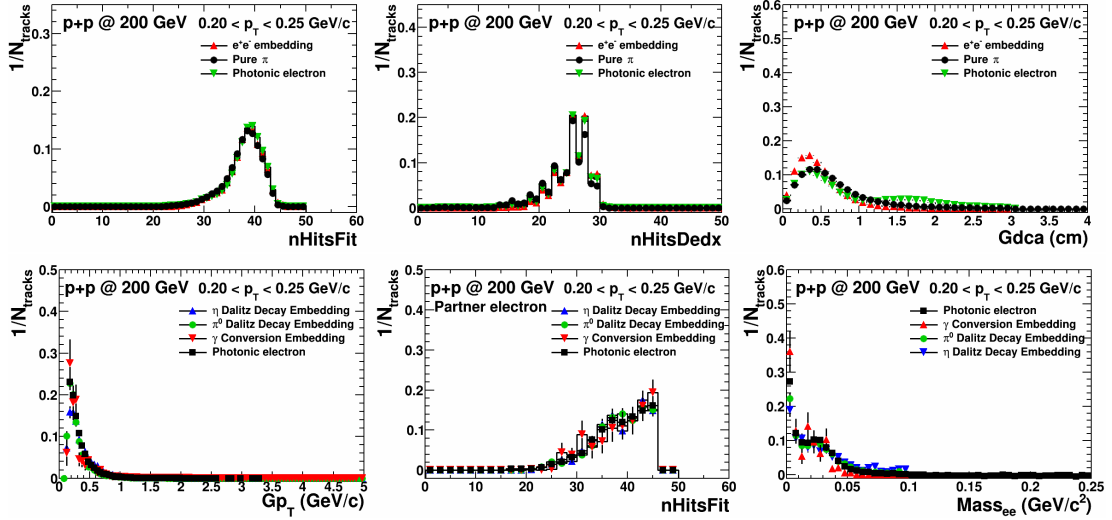


Fig. 3.29 $nHitsFit$, $nHitsDedx$ and $Gdca$ for NPE, G_{p_T} and $nHitsFit$ for partner electron of photonic electrons, and $M_{e^+e^-}$ for photonic electron distributions in $0.2 < p_T < 0.25$ GeV/c bin.

So systematic uncertainties need include the difference of their relative uncertainties from pure electron sample and pure pion sample, which was identified via track quality, $n\sigma_\pi$ and $n\sigma_\pi^{TOF}$ cuts. The $n\sigma_\pi^{TOF}$ was defined as:

$$\sigma_\pi^{TOF} = \left(\frac{1}{\beta} - \sqrt{m_\pi^2/p^2 + 1} \right) / \sigma, \quad (3.17)$$

where σ is a constant as a function of momentum. In addition, a thing worth noticing is that the relative uncertainties in relation to photonic electrons need to be corrected by the ratio of photonic electrons to NPE when they were considered as the systematic uncertainties of NPE spectrum.

2. Electron purity extraction

When we extracted the purity of inclusive electrons, the mean, sigma, eta with one time their standard deviations as constraint were used to fit $n\sigma_e$ distributions of identified particles in different p_T bins. To estimate the systematic uncertainty of the purity, we calculated the purity via fitting $n\sigma_e$ distributions under the constraint with two times standard deviations. The difference between these two results was taken as the systematic uncertainty shown in the left panel of Fig. 3.31.

3. Efficiency

The primary sources of uncertainties from efficiency will be described in the following.

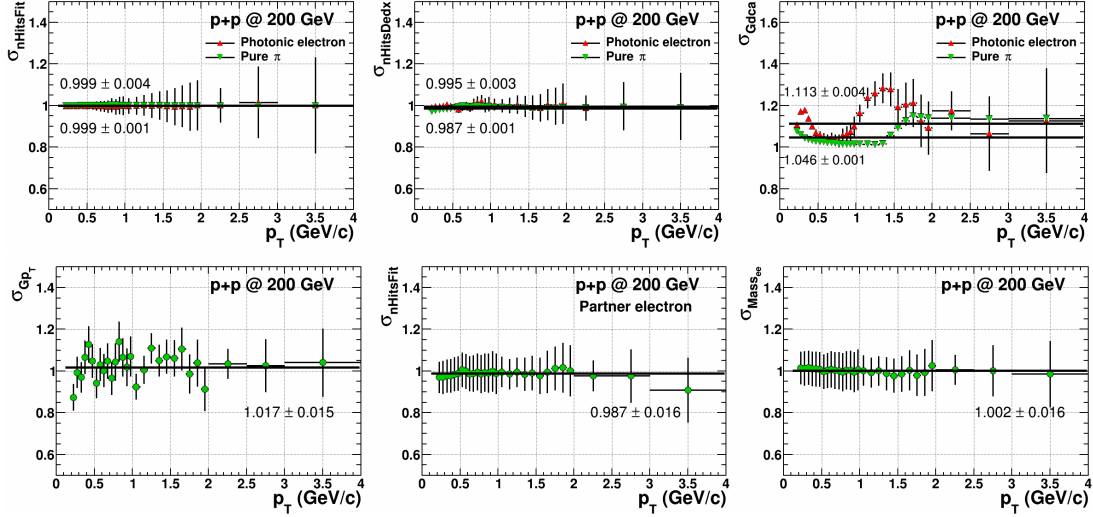


Fig. 3.30 Relative uncertainties of $nHitsFit$, $nHitsDedx$ and $Gdca$ for NPE, Gp_T and $nHitsFit$ for partner electron of photonic electrons, and M_{e+e-} for photonic electrons as a function of p_T .

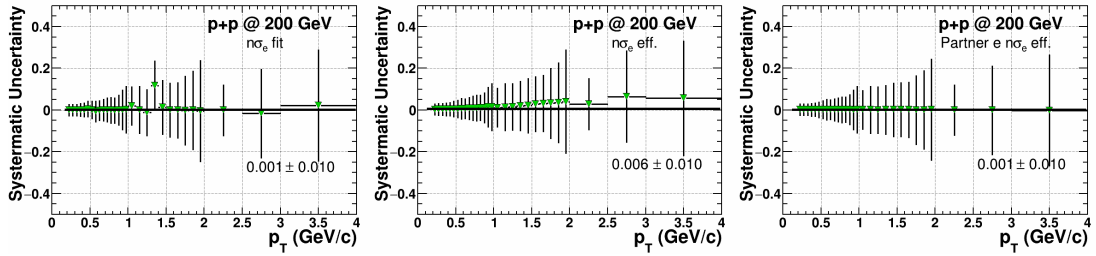


Fig. 3.31 Systematic uncertainties of purity, tagged electron $n\sigma_e$ cut efficiency and partner electron $n\sigma_e$ cut efficiency as a function of p_T .

For the systematic uncertainties associated with tagged and partner electron $n\sigma_e$ cut efficiency vs. p_T , they have been explained in the calculation of $n\sigma_e$ cut efficiency. The systematic uncertainties of them are shown in the middle and right of Fig. 3.31.

The fraction of electrons with $|1/\beta - 1| < 0.03$ determined the TOF EPID efficiency. This has been done by a Gaussian function to fit the pure electron $1/\beta$ distribution in order to remove non-Gaussian component from hadron contamination contribution to the tails of this distribution. The efficiency also can be estimated by counting the entries at $|1/\beta - 1| < 0.03$ in the $1/\beta$ distribution of pure electrons in each p_T bin. The difference between them was taken as the systematic uncertainty of TOF EPID efficiency, which is shown in the left panel of Fig. 3.32.

The BEMC matching and EPID efficiencies were calculated using pure electron sample from data. So the data uncertainty was taken as their systematic uncertainties, which is shown in the right panel of Fig. 3.32.

When we got the inclusive gamma spectrum, the direct gamma was fitted by the

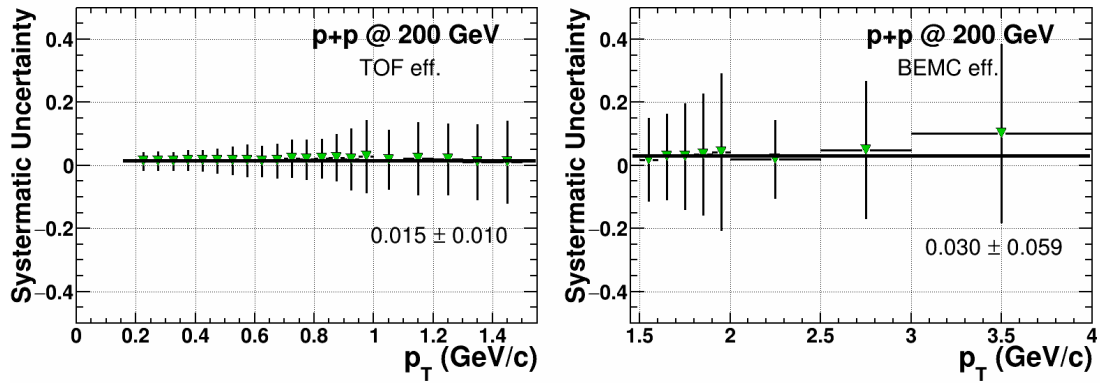


Fig. 3.32 Systematic uncertainties of TOF EPID efficiency, BEMC matching and EPID efficiencies as a function of p_T .

power-law function. This fitting uncertainty was as a part of the systematic uncertainties of photonic electron reconstruction efficiency. In addition, the final efficiency used to correct NPE spectrum was also from the fitting of the combined photonic electron reconstruction efficiency. This fitting uncertainty has a contribution to the systematic uncertainties of photonic electron reconstruction efficiency. Fig. 3.33 shows the systematic uncertainties of photonic electron reconstruction efficiency as a function of p_T .

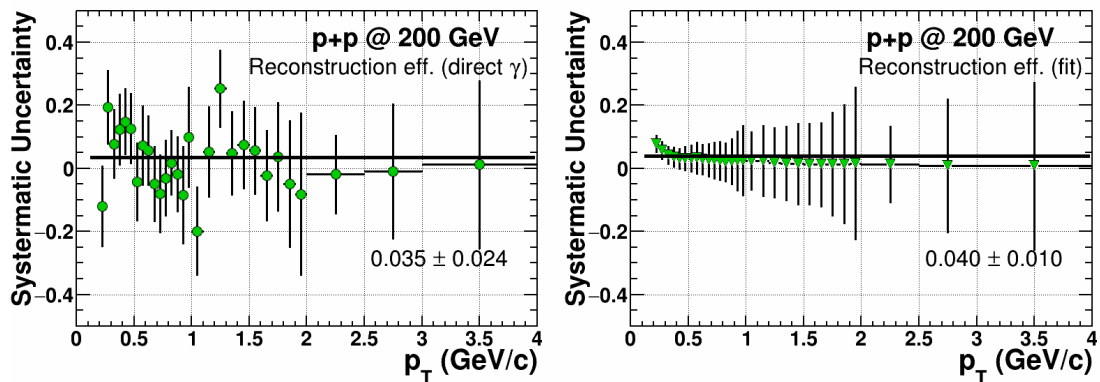


Fig. 3.33 Systematic uncertainties of photonic electron reconstruction efficiency as a function of p_T .

4. Background from hadron decays

The fitting uncertainties of the ratio of K^\pm yield from STAR to that from PYTHIA and K_{e3}^\pm reconstruction efficiency were considered as the systematic uncertainty of K_{e3} , which is shown in the left panel of Fig. 3.34.

The systematic uncertainties of $\omega \rightarrow e$ and $\phi \rightarrow e$ background contribution were

caused by the dN/dy uncertainties of ω and $c\bar{c}$, and are shown in the middle and right panel of Fig. 3.34.

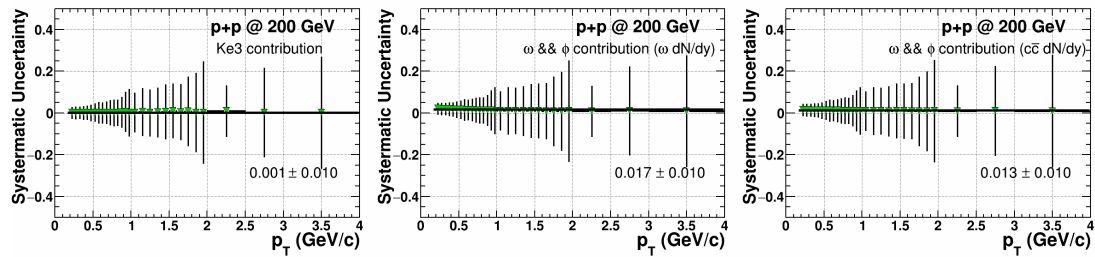


Fig. 3.34 Systematic uncertainties of K_{e3} and hadron decayed electron contribution as a function of p_T .

The error transfer formula

$$\sigma_{total} = \sqrt{\sigma_1^2 + \sigma_2^2 + \sigma_3^2 + \dots} \quad (3.18)$$

was used to calculate the total systematic uncertainties, which are shown in Fig. 3.35.

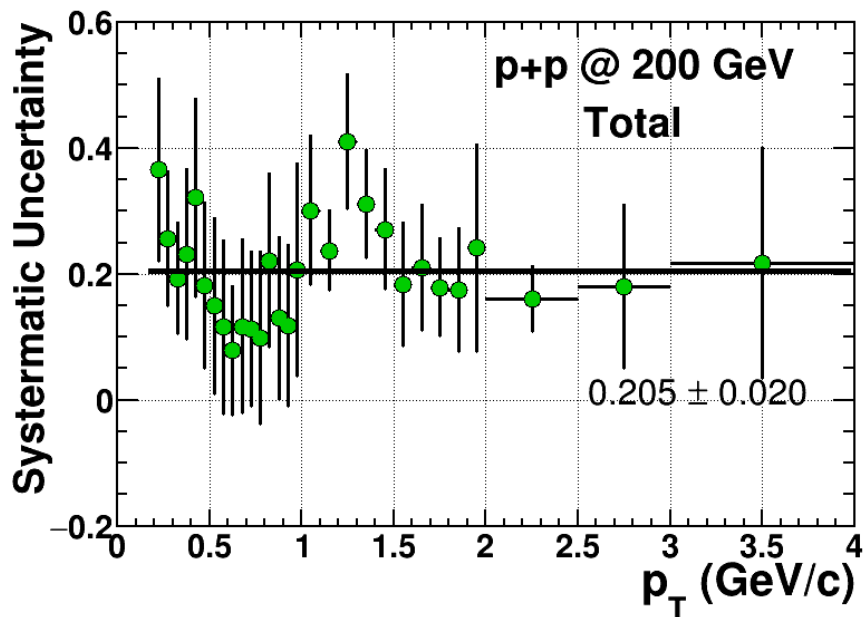


Fig. 3.35 Total systematic uncertainties as a function of p_T .

3.2 Run 2014 200 GeV $Au + Au$ Collision Analysis

3.2.1. Dataset and Event selection

The analysis was based on the Run14 $Au + Au$ High-Tower (HT) triggered events collected by requiring a certain threshold on the energy deposited in one BEMC tower

in order to get a highly enriched high- p_T electrons. There were total of 51.7M HT1 and 60.8M HT2 events for lowmid-luminosity, and 33.7M HT1 and 75.2M HT2 events for high-luminosity, which were the statistics for number of events satisfying the trigger ID 450201 and 450211 for HT1, 450202 and 450212 for HT2, in run14 $Au + Au$ 200 GeV collisions. The HT1 and HT2 are online triggers which require transverse energy (E_T) thresholds of ~ 3.4 GeV and ~ 4.3 GeV. The data production library version was P15ic. Table 3.2 shows the event selection criteria and the number of events after event selections is shown in Table 3.3. The correlation and difference distributions between the V_z position from the TPC and the VPD from HT1 events of lowmid-luminosity are shown in Fig. 3.36. In addition, to reject the events from the beam hitting the beam pipe, a radial length less than 2 cm for the vertex was required.

Table 3.2 Event selection criteria

Event Selections
$!(V_x == 0 \&\& V_y == 0 \&\& V_z == 0)$
$ V_r < 2 \text{ cm}$
$ V_z^{TPC} < 30 \text{ cm}$
$ V_z^{TPC} - V_z^{VPD} < 3 \text{ cm}$

Table 3.3 Number of events after event selections.

Event Trigger	N_{events} after event selection (M)
HT1*VPDDB (lowmid-lumilosity)	50.8
HT2*VPDDB (lowmid-lumilosity)	59.5
HT1*VPDDB (high-lumilosity)	32.9
HT2*VPDDB (high-lumilosity)	73.2

3.2.2. Centrality definition

In this analysis, the 0-80% MB centrality was determined by measured multiplicity (grefmult) of charged particles at mid-rapidity ($|\eta| < 0.5$) with no less than 10 TPC hits

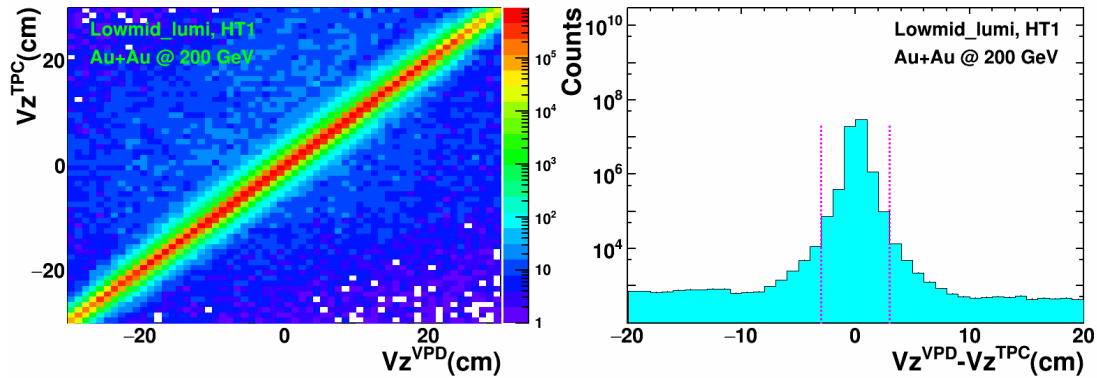


Fig. 3.36 Left panel: Correlation between V_z^{TPC} and V_z^{VPD} from HT1 events of lowmid-luminosity. Right panel: Difference of V_z^{VPD} and V_z^{TPC} from HT1 events of lowmid-luminosity.

and DCA less than 3 cm with some correction according to V_z and luminosity. Performing the V_z and luminosity correction are because of grefmult depends on the V_z cuts, which is caused by the west and east halves of TPC do not necessarily have the same efficiency, and the luminosity, which is due to the associated TPC tracking efficiency has luminosity dependence. The luminosity correction was done through the ZdcX (Zdc coincidence rate) correction. The sub-centralities were selected by applying the grefmult cuts to 0-80% multiplicity distribution with a weight from the ratio function of data to calculation of Glauber model [43]. This is due to the VPD trigger is less efficient in low multiplicity collisions, which causes losses in peripheral $Au + Au$ collisions. In this analysis, the centrality dependence study of the NPE has three centrality bins: 0-10%, 10-20% and 20-40%. The detailed information can be found at [111, 112]. Table 3.4 lists the definition of the MB centrality for Run14 200 GeV $Au + Au$ collisions.

Table 3.4 Centrality definition, N_{coll} and N_{part} .

Centrality	grefmult cut	N_{coll}	N_{part}
0 – 10%	> 373	959.42547 ± 27.80131	324.30271 ± 3.66202
10 – 20%	> 263	606.93118 ± 30.60806	235.21466 ± 8.53404
20 – 40%	> 116	299.07347 ± 31.49844	141.18049 ± 10.66581
0 – 80%	> 10	303.78965 ± 21.22558	127.49225 ± 7.52968

3.2.3. Track selection and Electron identification

In this analysis, two main detectors of STAR, the TPC and the BEMC, were used to reconstruct charged tracks and perform PID. The difference of the electron identification in $p + p$ and $Au + Au$ collisions is that the SMD were used to provide the shower shape in order to identify high- p_T electrons in $Au + Au$ collisions.

3.2.4. NPE raw yield extraction

1. Inclusive electrons and purity

For our inclusive electrons, identification was carried with TPC combined with BEMC (SMD). Table 3.5 lists the main cuts for the track candidate selections. The cuts of

Table 3.5 Cuts of track candidate selections.

Track quality cuts
Primary track
$nHitsFit \geq 20$
$0.52 < nHitsFit/nMax < 1.2$
$nHitsDedx \geq 15$
$Gdca < 1.5 \text{ cm}$
$p_T > 2.5 \text{ GeV}/c$ for HT1; $p_T > 3.5 \text{ GeV}/c$ for HT2: p_T cut according trigger threshold.
$ \eta < 0.7$

electron selections are listed at the below:

- $ADC0 > 256$ && $dsmADC > 15$ (corresponding to $E_T \sim 3.4 \text{ GeV}$) for HT1; $ADC0 > 304$ && $dsmADC > 18$ (corresponding to $E_T \sim 4.3 \text{ GeV}$) for HT2: required triggered electron; Data Storage and Manipulation (DSM) recorded ADC (dsmADC) value provides the online firing HT trigger if higher than thresholds (15 for HT1, 18 for HT2); ADC0 (Analog Digital Converters) is the offline ADC value of the most energetic tower in a BTOW cluster and is responsible for firing HT triggers.
- Tower energy $E > 0$:
- $0.3 < p/E < 1.5$:
- $nEta > 1$ && $nPhi > 1$: the number of SMD hits in η - ϕ plane.

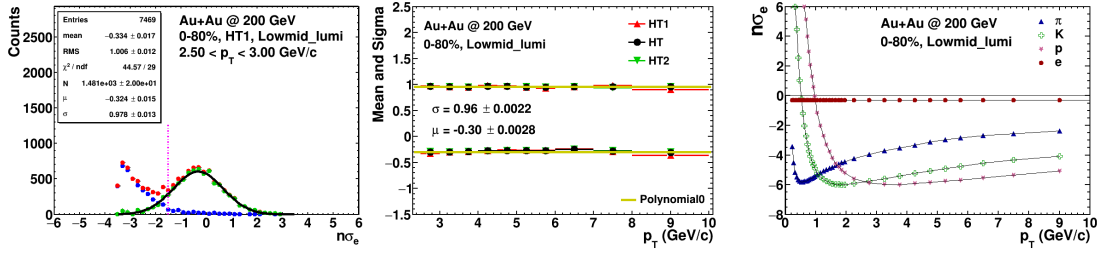


Fig. 3.37 Left panel: $n\sigma_e$ distribution in $2.50 < p_T < 3.00$ GeV/c bin of pure electrons at 0-80% centrality for HT1 events of lowmid-luminosity. The Gaussian function was used to fit this distribution. The pink lines show the $n\sigma_e$ cut of inclusive electron. Middle panel: Mean and sigma from the fittings of $n\sigma_e$ distributions for pure electrons as a function of p_T at 0-80% centrality in different triggers of lowmid-luminosity. The polynomial0 were performed to fit them. Right panel: Means from Bischel function as a function of p_T for pure hadrons at 0-80% centrality of lowmid-luminosity.

- $|\Delta\phi| < 0.08$ && $|\Delta Z| < 3$: the distance between the position of shower center provided by SMD and the track projection position on SMD from TPC in ϕ and Z direction, respectively.
- $-1.5 < n\sigma_e < 3.0$

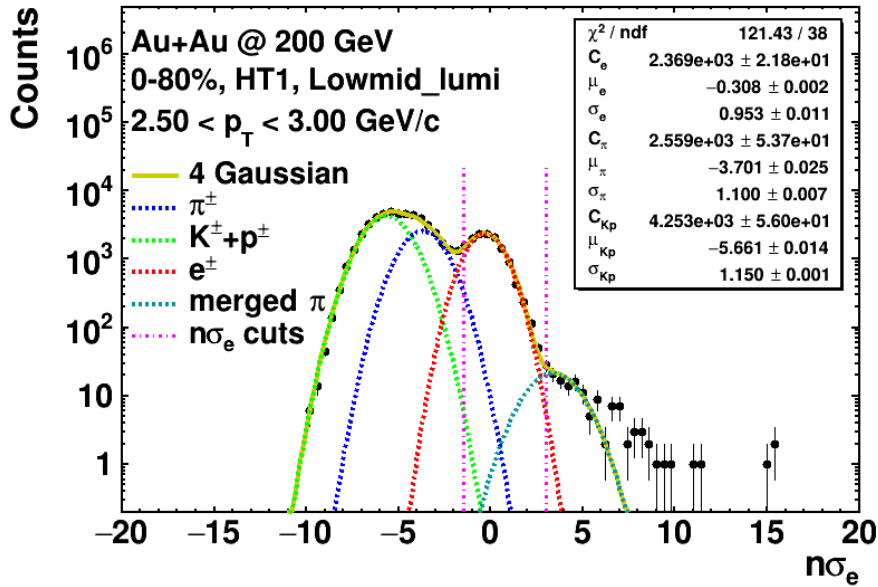


Fig. 3.38 $n\sigma_e$ distribution and its fitting result of multi-Gaussian function in $2.50 < p_T < 3.00$ GeV/c bin for identified particles for HT1 events of lowmid-luminosity. The pink dotted lines show the $n\sigma_e$ cuts of inclusive electrons.

After applying the above cuts, the $n\sigma_e$ distributions of identified particles in dif-

ferent p_T bins were obtained for different centralities, triggers and luminosities. Then Gaussian functions were used to fit these distributions. The constraints of electrons were also from the fitting results of $n\sigma_e$ distributions of pure electrons in different p_T bins, which in $2.50 < p_T < 3.00$ GeV/c bin at 0-80% centrality for HT1 events of lowmid-luminosity is exhibited in the left panel of Fig. 3.37. And the mean and sigma from fitting results as a function of p_T in 0-80% centrality for lowmid-luminosity are shown in the middle panel of Fig. 3.37. For the constraints of pure hadrons ($\pi, K + p$), the

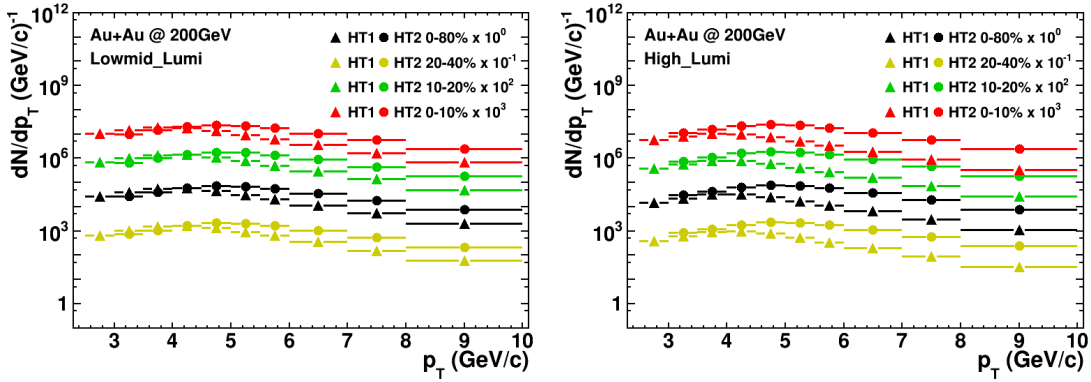


Fig. 3.39 Raw dN/dp_T distributions of inclusive electrons in different centralities, triggers and luminosities.

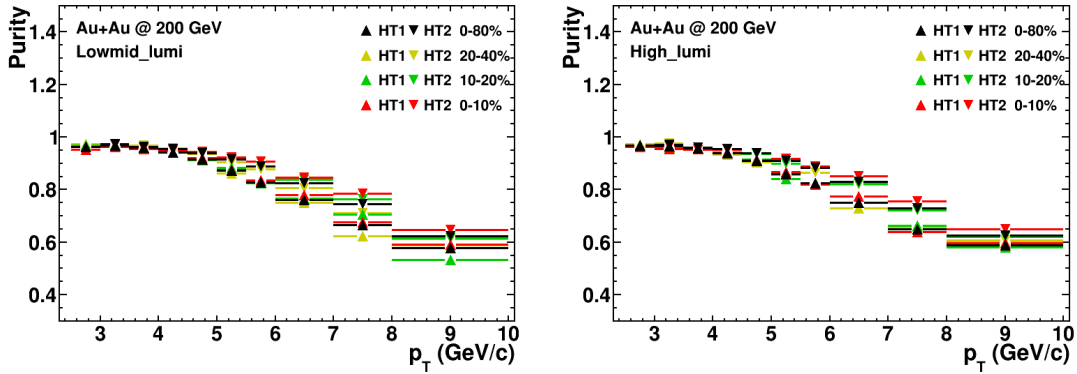


Fig. 3.40 Purity distributions of inclusive electrons in different centralities, triggers and luminosities.

mean are from theoretical calculation of Bischel function with considering $n\sigma_e$ shift of electrons. And the sigma was set as 1.2 ± 0.1 for π and 1.25 ± 0.1 for $K + p$ according to the Gaussian fitting results of $n\sigma_e$ distributions of pure hadron sample, which was selected via applying a very tight m^2 cut provided by TOF and $|n\sigma_h| < 4$ ($h = \pi, K, p$) [113]. The right panel of Fig. 3.37 show the mean as a function of p_T of pure hadrons. The final fitting of $n\sigma_e$ distribution in each p_T bin was obtained and that in $1.50 < p_T <$

1.60 GeV/c bin is shown in Fig. 3.38. The obtained raw dN/dp_T distributions of inclusive electrons in different centralities, triggers and luminosities are shown in Fig. 3.39. Fig. 3.40 shows the purity distributions of inclusive electrons in different centralities, triggers and luminosities.

2. Photonic electron cocktail

The partner electron and e^+e^- pair cuts for photonic electrons (same cuts with inclusive electrons for tagged electrons) are listed in Table 3.6. Fig. 3.41 shows the obtained

Table 3.6 Cuts of the partner electrons and e^+e^- pairs for photonic electrons.

Partner electrons	e^+e^- pairs
Global track	
$nHitsFit \geq 15$	
$0.52 \leq nHitsFit/nMax \leq 1.2$	$M_{ee} < 0.24 \text{ GeV}/c^2$
$Gdca < 3.0 \text{ cm}$	$pairDca < 1.0 \text{ cm}$
$ p_T > 0.3 \text{ GeV}/c$	
$ \eta < 1.0$	

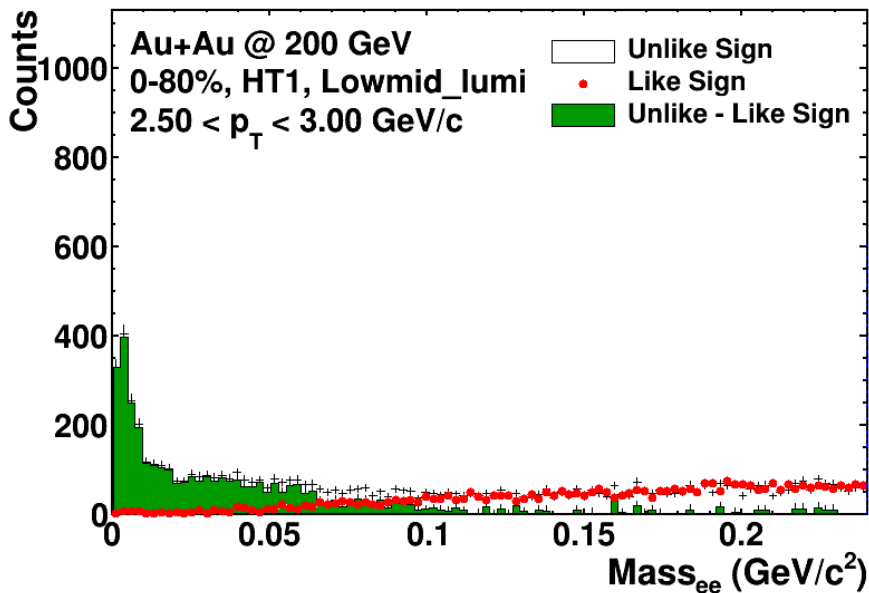


Fig. 3.41 $M_{e^+e^-}$ distribution at $2.50 < p_T < 3.00 \text{ GeV}/c$ bin in 0-80% centrality for HT1 events of lowmid-luminosity.

$M_{e^+e^-}$ distribution at $2.50 < p_T < 3.00 \text{ GeV}/c$ bin in 0-80% centrality for HT1 events

of lowmid-luminosity. The raw dN/dp_T distributions of photonic electrons in different centralities, triggers and luminosities are shown in Fig. 3.42.

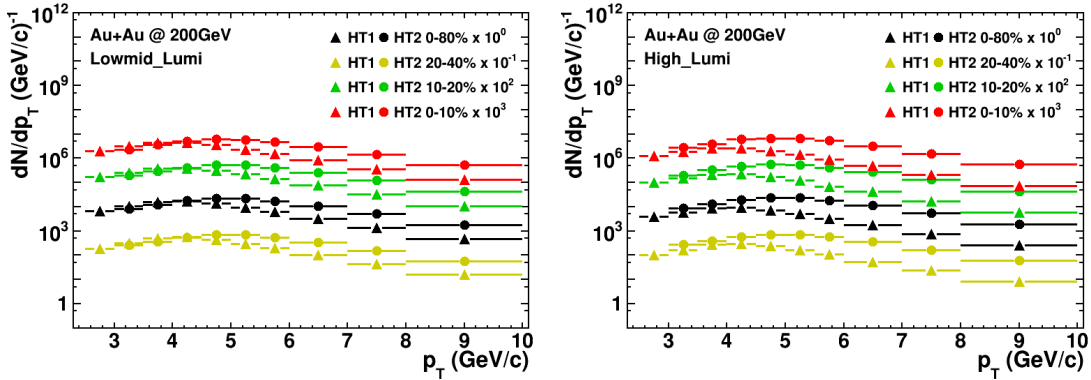


Fig. 3.42 Raw dN/dp_T distributions of photonic electrons in different centralities, triggers and luminosities.

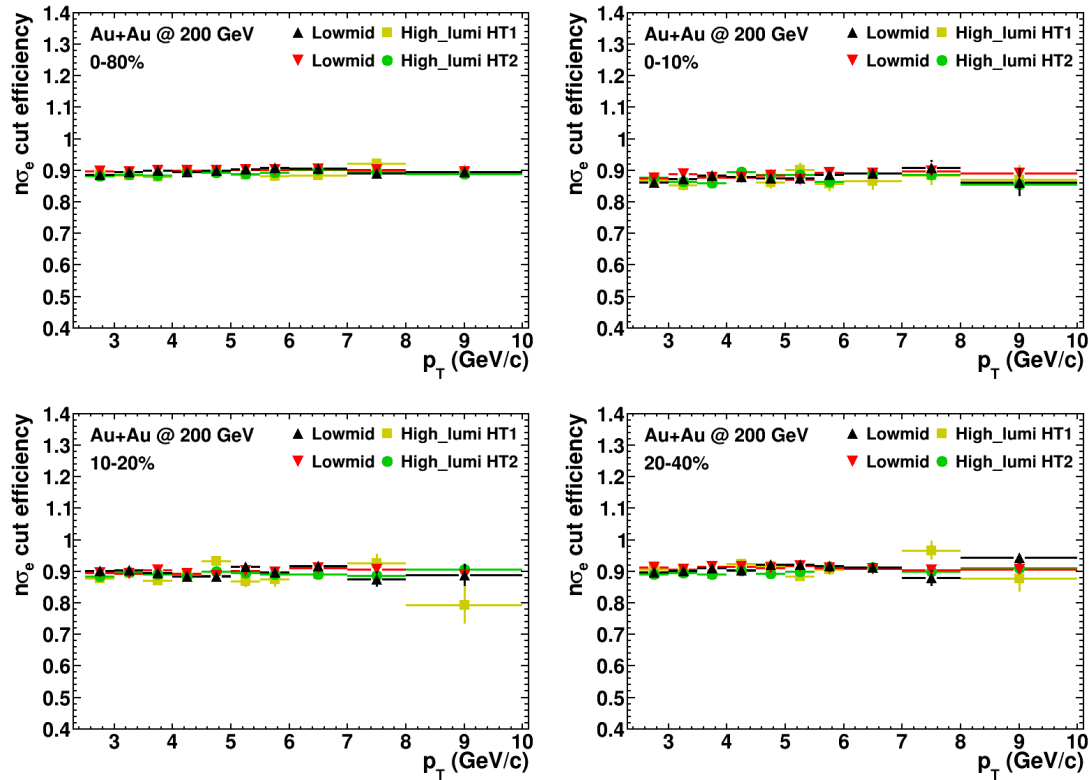


Fig. 3.43 $n\sigma_e$ cut efficiencies as a function of p_T in different centralities, triggers and luminosities.

3.2.5. Efficiency and Acceptance

The efficiencies, used to correct raw yields of NPE in $Au + Au$ collisions, includes:

- $n\sigma_e$ cut efficiency.

- BEMC matching efficiency.
- BEMC (SMD) EPID efficiency.
- Trigger efficiency.
- Photonic electron reconstruction efficiency.
- TPC tracking efficiency.

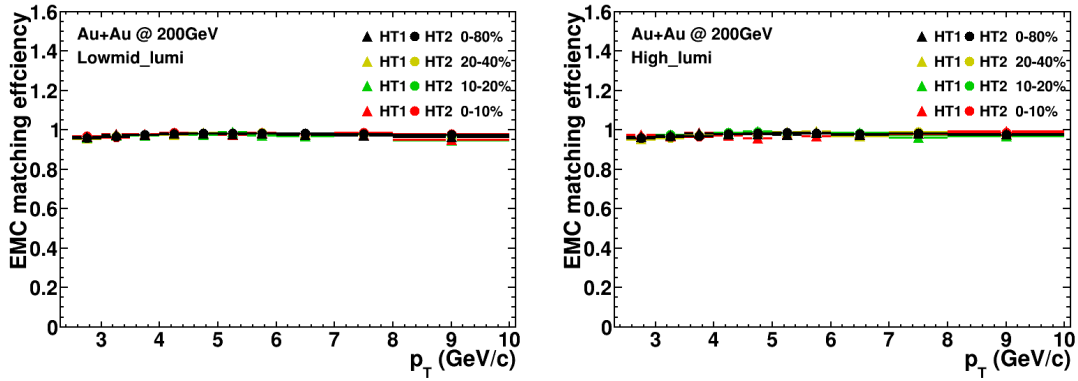


Fig. 3.44 BEMC matching efficiencies as a function of p_T in different centralities, triggers and luminosities.

For $n\sigma_e$ cut, BEMC matching and TPC tracking efficiencies were obtained using the same method in $p + p$ collisions. They are shown in Fig. 3.43, 3.44 and 3.45.

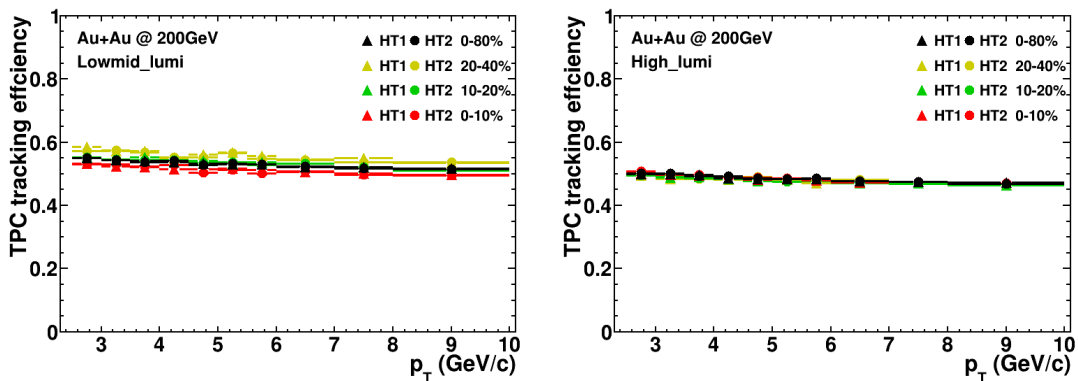


Fig. 3.45 TPC tracking efficiencies as a function of p_T in different centralities, triggers and luminosities.

Due to the SMD was used for electron identification in $Au + Au$ collisions, the BEMC (SMD) EPID efficiency was obtained by taking the ratio of the number of tracks with BEMC (SMD) EPID cut and the number of tracks in TPC passed the track quality

and acceptance cuts using the pure electron sample with requiring the triggered electron. The BEMC (SMD) EPID efficiency was defined as:

$$\epsilon = \frac{N(0.3 < p/E < 1.5 \& \& n\eta > 1 \& \& n\Phi > 1 \& \& |\Delta\phi| < 0.08 \& \& |\Delta Z| < 3)}{N_{TPC}} |trigger\ electron. (3.19)$$

The BEMC (SMD) EPID efficiencies as function of p_T in different centralities, triggers and luminosities are shown in Fig. 3.46.

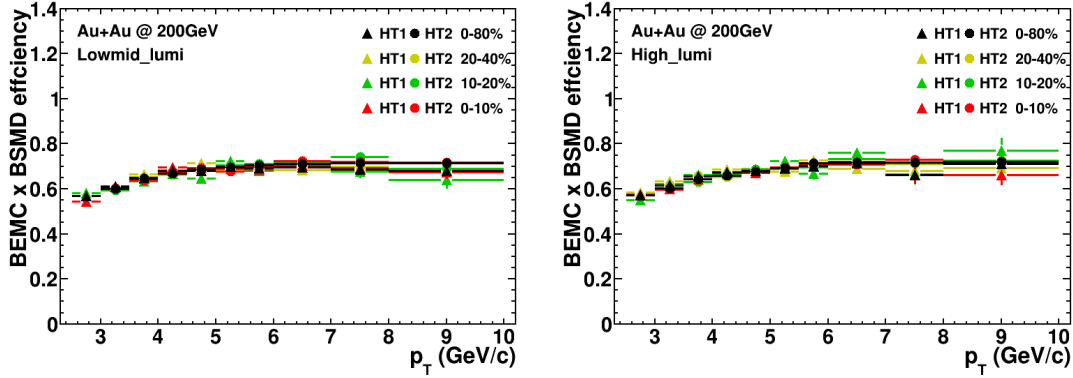


Fig. 3.46 BEMC (SMD) EPID efficiencies as a function of p_T in different centralities, triggers and luminosities.

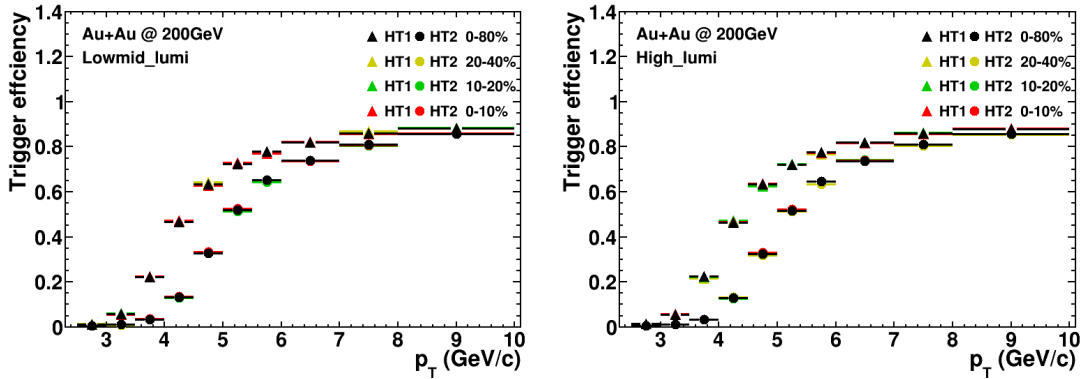


Fig. 3.47 Trigger efficiencies as a function of p_T in different centralities, triggers and luminosities.

When an event with electrons is marked as a HT trigger one, it does not mean this trigger must be fired by the signal, e.g. electrons, in the events but may be fired by the trigger circuit noise, e.g. a photon in the same events or a background event, which goes beyond the trigger threshold. This electron from random trigger benefit should be removed to avoid the uncontrollable condition, e.g. dirty beams, etc. Just like mentioned in section of photonic electron cocktail, the triggered electrons were required in this analysis by providing a ADC0 cut for different HT trigger. Thus the trigger efficiency was obtained by taking the ratio of the number of tracks with ADC0 and

dsmADC cuts and the number of tracks in TPC passed the track quality and acceptance cuts using electron embedding. The trigger efficiency was defined as:

$$\epsilon = \frac{N(ADC0 \&\& dsmADC \text{ cuts})}{N_{TPC}}. \quad (3.20)$$

The trigger efficiencies as function of p_T in different centralities, triggers and luminosities are shown in Fig. 3.47.

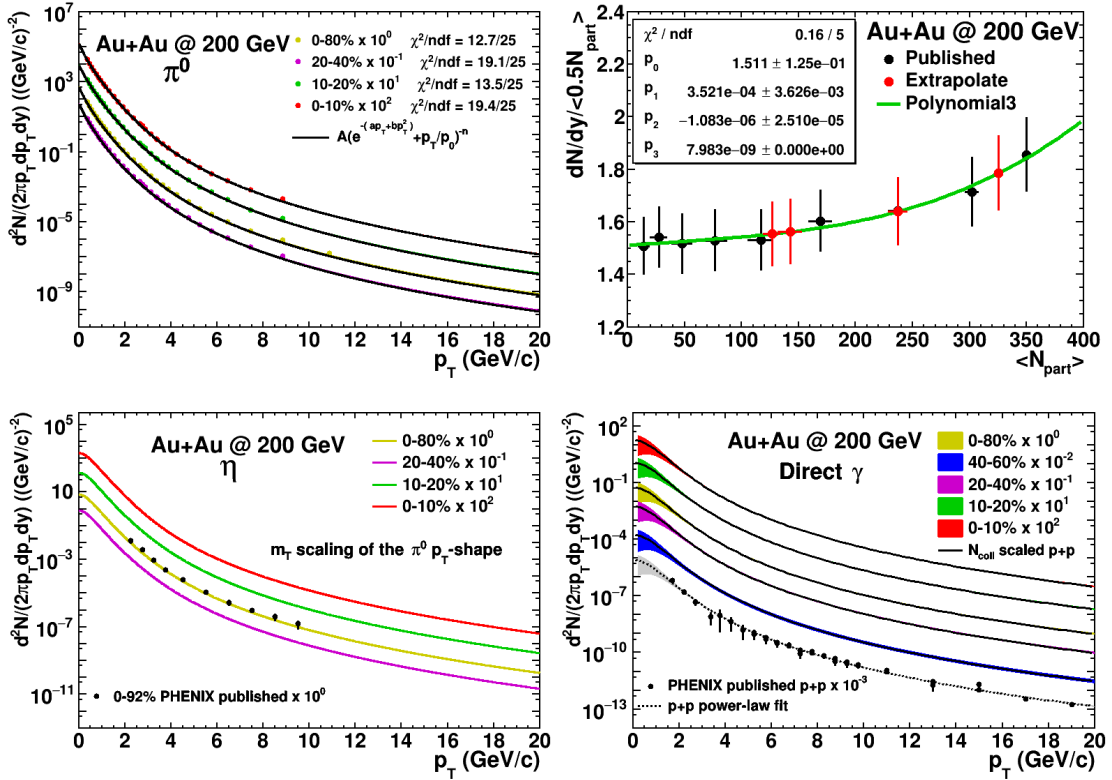


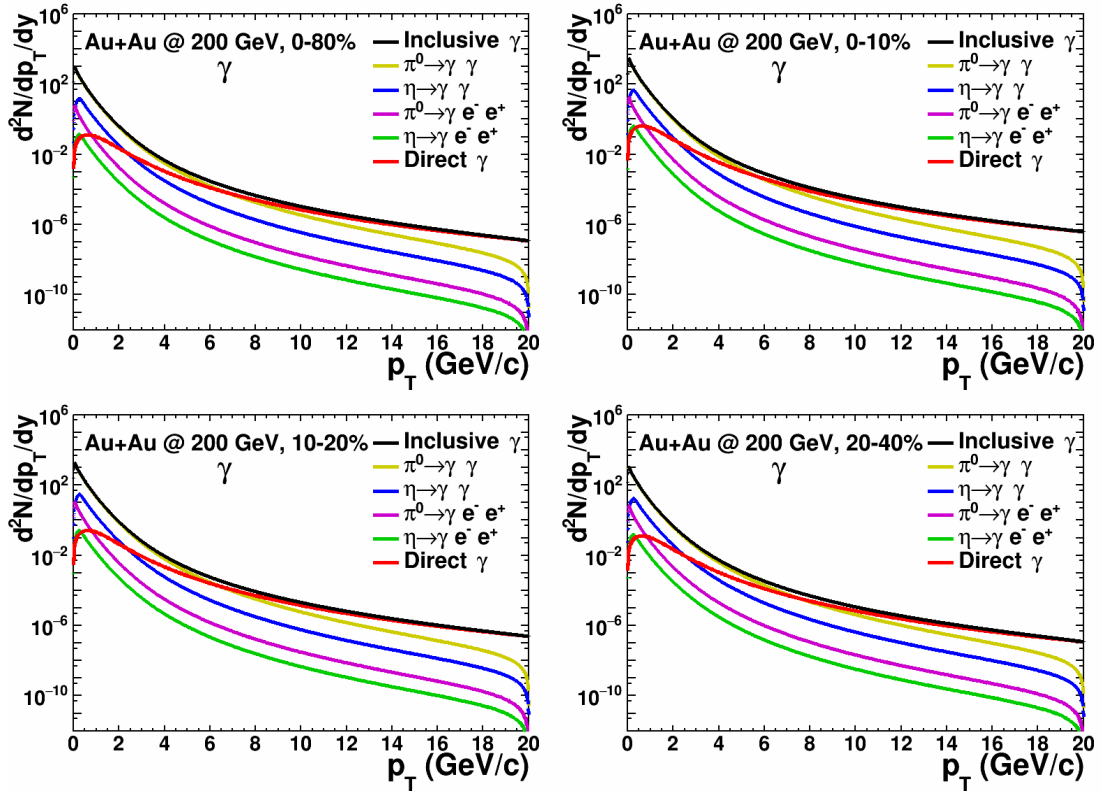
Fig. 3.48 Top-left panel: π^0 invariant yield distributions in different centralities. The functions of a power-law with an exponential were used to fit invariant yield distributions. Top-right panel: $dN/dy|_{<0.5N_{part}>}$ as a function of N_{part} for π^0 . Bottom-left panel: η invariant yield distributions in different centralities from m_T scaling of the π^0 p_T -shape, along with that in 0-92% $Au + Au$ collisions from PHENIX published one. Bottom-right panel: Direct γ invariant yield distributions in different centralities in $Au + Au$ collisions along with that in $p + p$ collisions. The power-law was used to fit invariant yield in $p + p$ collisions.

For photonic electron reconstruction efficiency, the same method with that in $p + p$ collisions was used. Here, the detailed information about obtaining the π^0 , η and inclusive γ spectra used to weight the embedded parents in different centralities only will be discussed. The STAR published invariant yields of π^0 $((\pi^+ + \pi^-)/2)$ [114, 115] along with fitting functions of a power-law with an exponential in different centralities are shown in the top-left panel of Fig. 3.48. For η spectra in different centralities, STAR

Table 3.7 dN/dy of π^0 , R_π and dN/dy of η at mid-rapidity in different centralities.

Centrality	20-40%	10-20%	0-10%	0-80%
dN/dy_π	111.4 ± 8.9	194.5 ± 15.6	290.6 ± 23.2	98.5 ± 7.9
R_π	1.131	1.975	2.950	1.000
dN/dy_η	8.89 ± 2.67	15.52 ± 4.66	23.19 ± 6.96	7.86 ± 2.36

has not measured results. The method of m_T scaling of the π^0 p_T -shape (change p_T of π^0 to $\sqrt{p_T^2 + m_\eta^2 - m_{\pi^0}^2}$) was utilized to obtain the invariant yields of η . Certainly, these obtained invariant yields need to be normalized by dN/dy of η , which were got by the following process:


Fig. 3.49 Inclusive γ p_T spectra in different centralities, along with those from different sources.

- Obtain $dN/dy / \langle 0.5N_{part} \rangle$ as a function of N_{part} using published dN/dy for π^0 .
- Fit this distribution using the Polynomial3 function to obtain the dN/dy of π^0 in our analysis centrality bins.

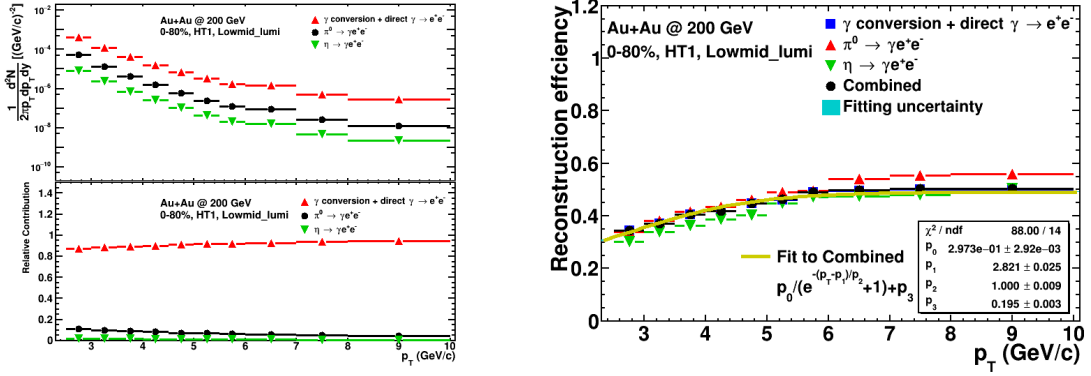


Fig. 3.50 Left panel: Relative contribution from γ conversion, π^0 and η Dalitz decays to photonic electrons as a function of p_T at 0-80% centrality in HT1 events of lowmid-luminosity. Right panel: Combined reconstruction efficiency as a function of p_T along with the individual efficiencies from γ conversion, π^0 and η Dalitz decays at 0-80% centrality in HT1 events of lowmid-luminosity.

- Calculate R_π in different centrality bins: $R_{\pi_i} = \frac{dN/dy_i}{dN/dy_{0-80\%}}$, i means different centralities bins.
- Calculate dN/dy of η in different centrality bins: $dN/dy_i = R_{\pi_i} * dN/dy_{0-80\%}$, $dN/dy_{0-80\%}$ of η is from PHENIX published result.

The $dN/dy / \langle 0.5N_{part} \rangle$ as a function of N_{part} for π^0 is shown in the top-right panel of Fig. 3.48. Table 3.7 shows the dN/dy of π^0 , R_π and dN/dy of η at mid-rapidity in different centralities. The obtained invariant yields of η in different centralities are shown in the bottom-left panel of Fig. 3.48, along with compared the PHENIX published result in 0-92% centrality [116].

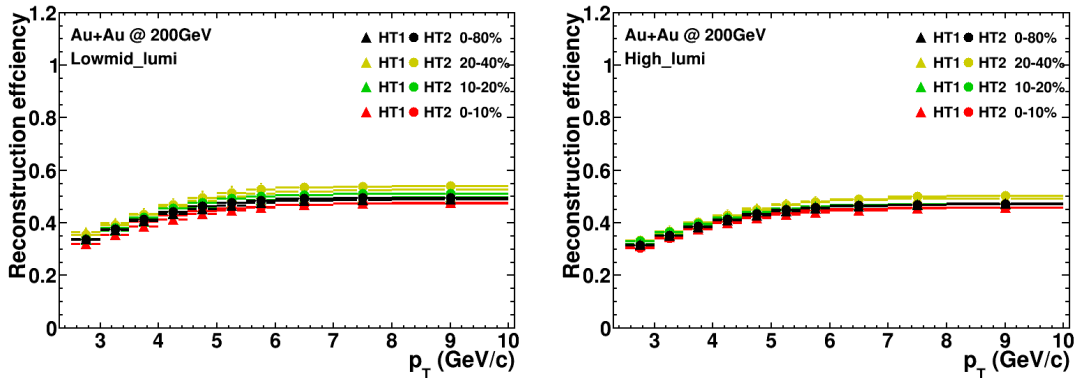


Fig. 3.51 Combined reconstruction efficiencies as a function of p_T in different centralities, triggers and luminosities.

The invariant yields of the direct γ at different centralities in $Au + Au$ collisions were obtained via the PHENIX $p + p$ results fitted by the power-law function and then

scaled by N_{coll} [103, 117, 118]. Despite the results from N_{coll} scaled $p + p$ one in different centralities are different with those in $Au + Au$ collisions. The differences are at the low p_T and have no effects on our results at high p_T analysis. The invariant yields of direct γ in different centralities are shown in the bottom-right panel of Fig. 3.48. The obtained inclusive γ p_T spectra in different centralities are shown in Fig. 3.49. The relative contributions and reconstruction efficiencies at 0-80% centrality in HT1 events of lowmid-luminosity for γ conversion, π^0 and η Dalitz decays are shown in Fig. 3.50. The combined reconstruction efficiencies in different centralities, triggers and luminosities are shown in Fig. 3.51.

All efficiencies as a function of p_T in different centralities, triggers and luminosities, which will be used to correct the NPE raw yields, are shown in Fig. 3.52.

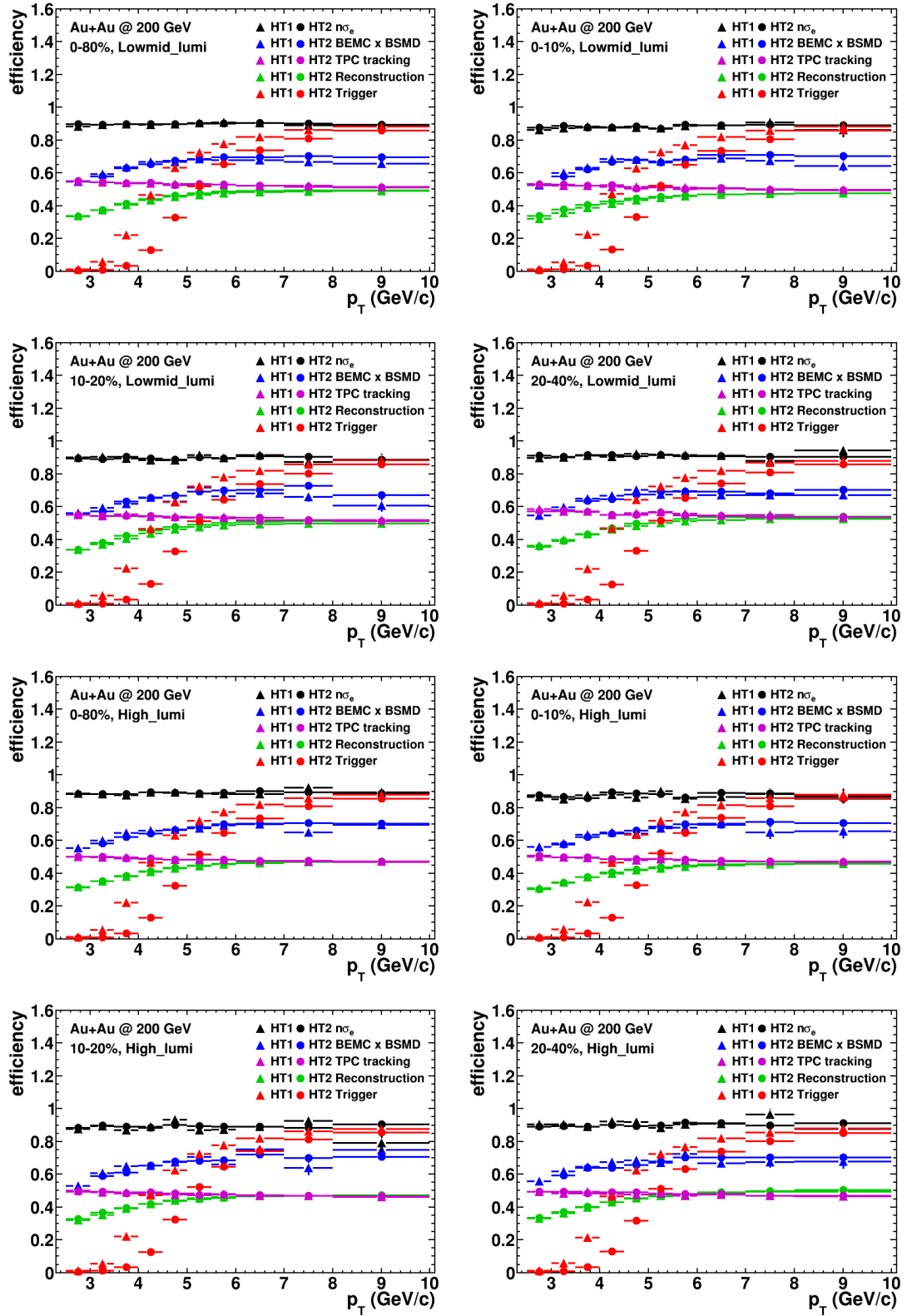
3.2.6. Equivalent number of MB events

Not all events which fire MB and HT triggers are recorded due to the finite bandwidth of the DAQ system. The random sampling is implemented to select these triggers. So the MB and HT trigger events are pre-scaled. Furthermore, when the HT trigger events were recorded, a VPDMB coincidence requirement was applied to reduce the trigger rate in order to improve the quality (Vz distribution for example) of the recorded events. Thus the equivalent number of MB events were used to normalize the measured NPE yield. It can be calculated as:

$$N_{MB}^{cent} = N_{MB}^{VtxCut} \times w^{cent} \times \frac{PS_{MB}}{PS_{HT}} \times \frac{N_{HT}^{ana}}{N_{HT}^{record}}, \quad (3.21)$$

- N_{MB}^{VtxCut} : number of MB events after vertex cuts.
- w^{cent} : event weights to take into account VPD trigger inefficiency for non-central events.
- PS : pre-scaling factor of triggers, some of which are fixed and the others are dynamic according to available bandwidth of DAQ during the data taking.
- N_{HT}^{ana} : number of analyzed HT events.
- N_{HT}^{record} : number of recorded HT events.

Fig. 3.53 shows the equivalent number of MB events in different centralities, triggers and luminosities.


 Fig. 3.52 Efficiencies as a function of p_T in different centralities, triggers and luminosities.

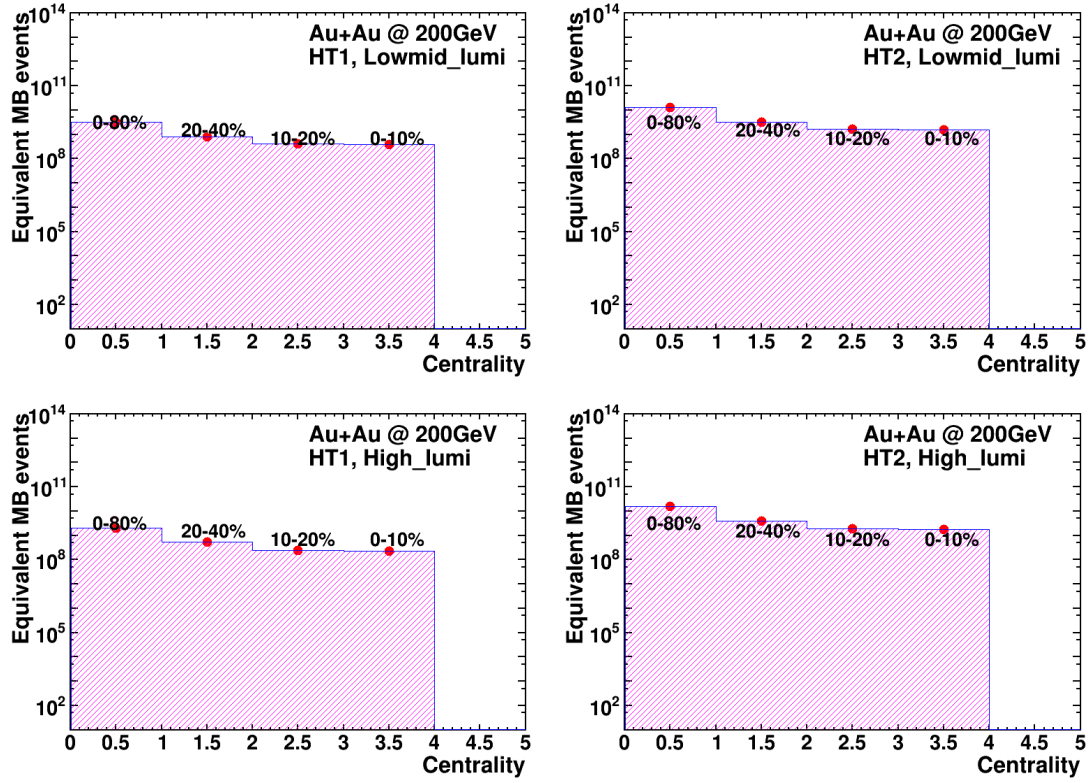


Fig. 3.53 Equivalent number of MB events in different centralities, triggers and luminosities.

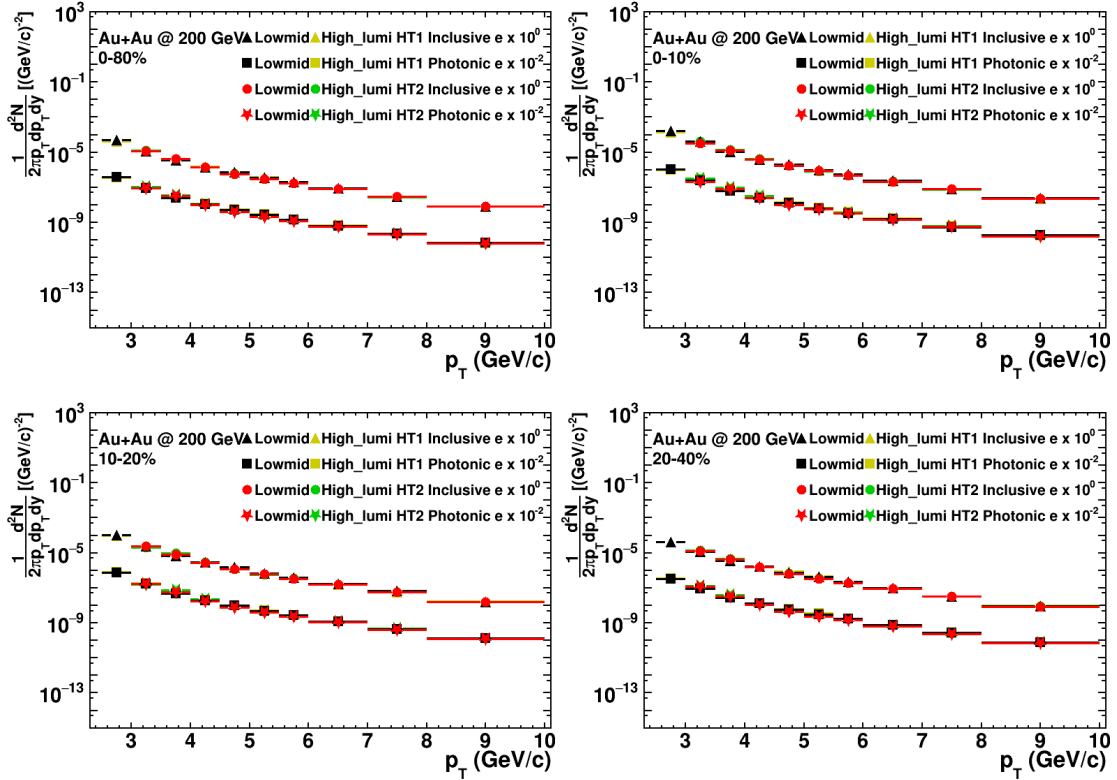


Fig. 3.54 Invariant yields of inclusive and photonic electrons in different centralities, triggers and luminosities.

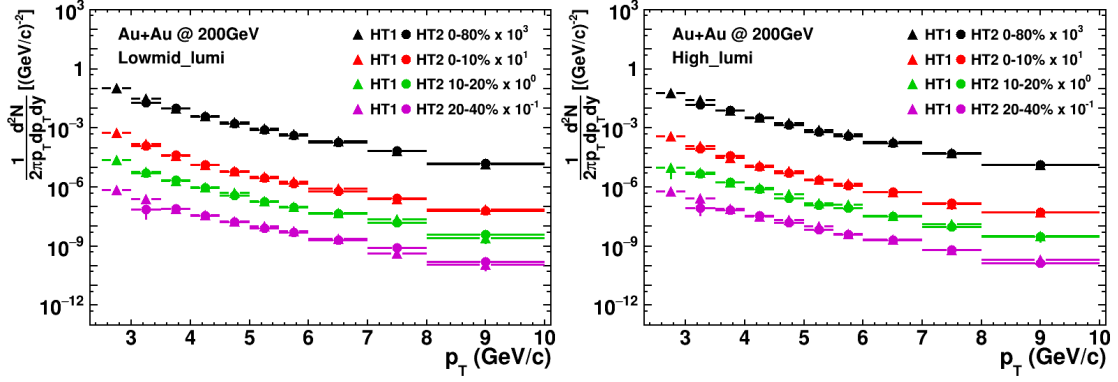


Fig. 3.55 Invariant yields of NPE in different centralities, triggers and luminosities.

The NPE invariant yield is defined as:

$$\frac{d^2 N}{2\pi p_T dp_T dy} = \frac{1}{N_{MB}^{cent}} \frac{1}{2\pi p_T \Delta p_T \Delta y} \frac{N_{NPE}}{\epsilon} \quad (3.22)$$

where N_{NPE} is the number of events in the relevant $Au + Au$ centrality selection, ϵ is the total efficiency, and Δp_T and Δy are the bin width in p_T and y , respectively. The invariant yields of inclusive electrons, photonic electrons and NPE in different centralities, triggers and luminosities are shown in Fig. 3.54 and 3.55.

3.2.7. Combine NPE results

In this section, we combined the results from the different luminosities for each centrality in $Au + Au$ 200 GeV collisions. The data points and their statistic errors from lowmid- and high-luminosities were combined by standard error propagate formula:

$$Y_{com} = w_{high} \times Y_{high} + w_{lowmid} \times Y_{lowmid}$$

$$\Delta_{com} = \sqrt{w_{high}^2 \delta_{high}^2 + w_{lowmid}^2 \delta_{lowmid}^2}$$

$$w_{high} = \frac{1/\delta_{high}^2}{1/\delta_{high}^2 + 1/\delta_{lowmid}^2} \quad (3.23)$$

$$w_{lowmid} = \frac{1/\delta_{lowmid}^2}{1/\delta_{high}^2 + 1/\delta_{lowmid}^2}$$

where $Y \sim$ yield, $w \sim$ weight and $\delta \sim$ relative statistic uncertainty.

The method used to combine the systematic uncertainties from the different luminosities are:

- relative systematic uncertainties: $\sigma_{com} = \sqrt{w_{high}^2 \sigma_{high}^2 + w_{lowmid}^2 \sigma_{lowmid}^2}$.

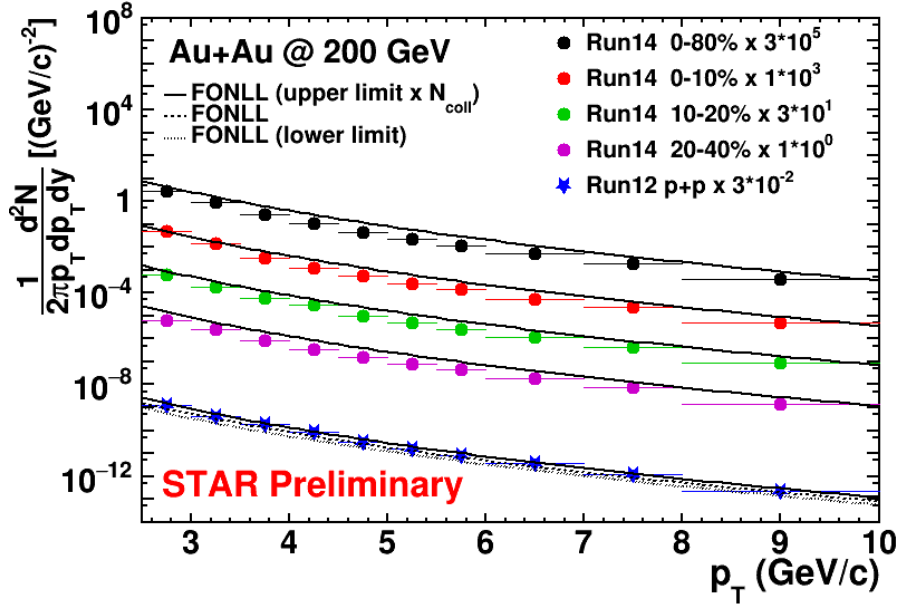


Fig. 3.56 Combined invariant yields of NPE in different centralities.

- total systematic uncertainties: $\Sigma_{com} = \sigma_{com} \times Y_{com}$.

The combined systematic uncertainties will be presented in section 3.2.9. For data points from the different triggers, the HT1 data points were used at $p_T < 4$ GeV/c while the HT2 data points were used at $p_T > 4$ GeV/c. Fig. 3.56 shows the combined invariant yields of NPE in different centralities.

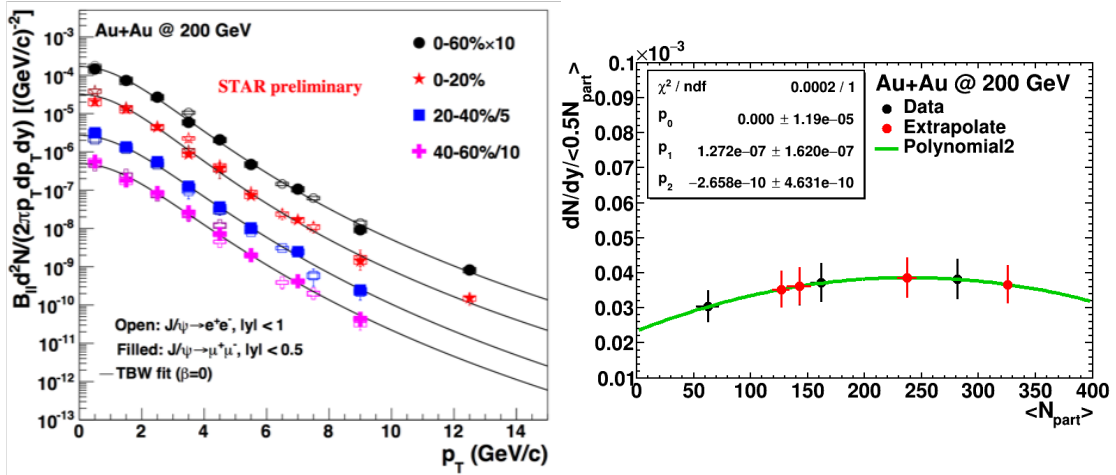


Fig. 3.57 Left panel: STAR preliminary J/Ψ invariant yields as a function of p_T in different centralities. Right panel: $dN/dy / \langle 0.5N_{part} \rangle$ as a function of N_{part} for J/Ψ .

Table 3.8 dN/dy of J/Ψ at mid-rapidity in different centralities

Centrality	20-40%	10-20%	0-10%	0-80%
$dN/dy_{J/\Psi}$	0.00258 ± 0.00039	0.00459 ± 0.00069	0.00598 ± 0.00090	0.00224 ± 0.00034

3.2.8. Background from J/Ψ decay

Thanks to the DCA cut we apply in analysis at STAR and kaon decay through the weak interaction have large c_τ , the K_{e3} production is significantly rejected, especially at high p_T , which is confirmed by our studies in $p + p$ collisions. Therefore K_{e3} contribution to the measured electron yield is negligible in this analysis. The non-photonic electron background from J/Ψ decay is a major background contribution to the calculated non-photonic electrons. Decaying the $J/\Psi \rightarrow e^+e^-$ through PYTHIA decay routine was

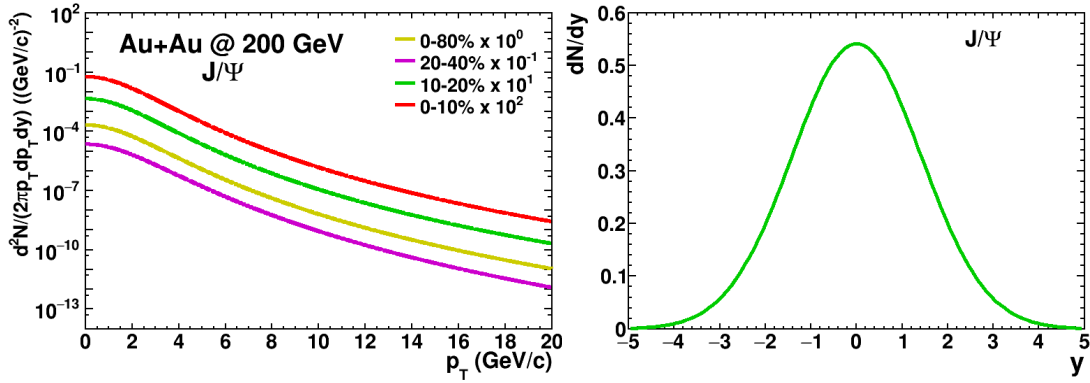


Fig. 3.58 Left panel: J/Ψ invariant yields as a function of p_T in different centralities. Right panel: J/Ψ dN/dy as a function of y .

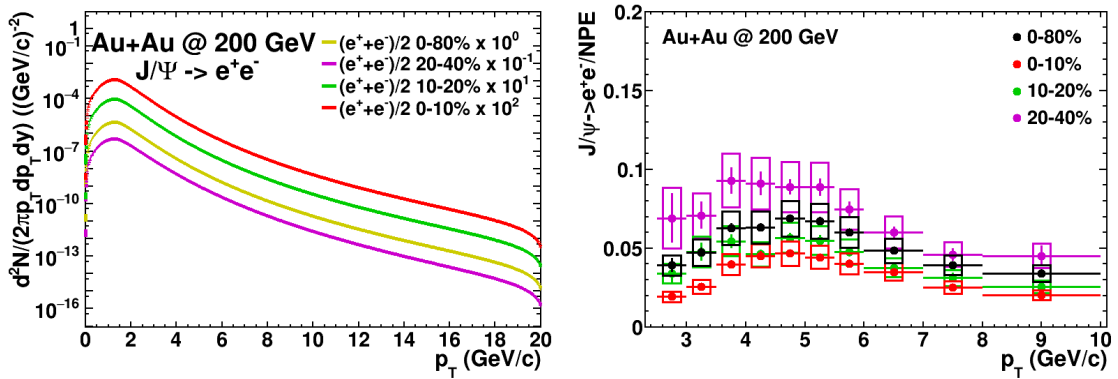


Fig. 3.59 Left panel: $J/\Psi \rightarrow e^+e^-$ invariant yields as a function of p_T in different centralities. Right panel: Ratios of $J/\Psi \rightarrow e^+e^-$ to NPE as a function of p_T in different centralities.

used to estimate this contribution. The algorithm is same as obtaining inclusive γ spec-

trum. Firstly, the invariant yields of J/Ψ in our centrality bins need to be extrapolated. The invariant yields of J/Ψ in different centrality bins, which were used to extrapolate, are from STAR preliminary results [119] and shown in the left panel of Fig. 3.57. The $dN/dy / \langle 0.5N_{part} \rangle$ as a function of N_{part} for J/Ψ is shown in the right panel of Fig. 3.57 and Table 3.8 shows the dN/dy of J/Ψ in our centrality bins from extrapolation. The final extrapolated invariant yields of J/Ψ in our centrality bins are shown in the left panel of Fig. 3.58, which were used p_T input in the PYTHIA decaying process, while input dN/dy vs. y distribution is shown in the right panel of Fig. 3.58. The left panel of Fig. 3.59 shows the invariant yields of electrons from J/Ψ decay in different centralities. The ratios of $J/\Psi \rightarrow e^+e^-$ invariant yields to those of NPE subtracting J/Ψ decayed electron contribution and correcting bin shift in different centralities are shown in the right panel of Fig. 3.59. The bin shift correction factors in different centralities are shown in Fig. 3.60.

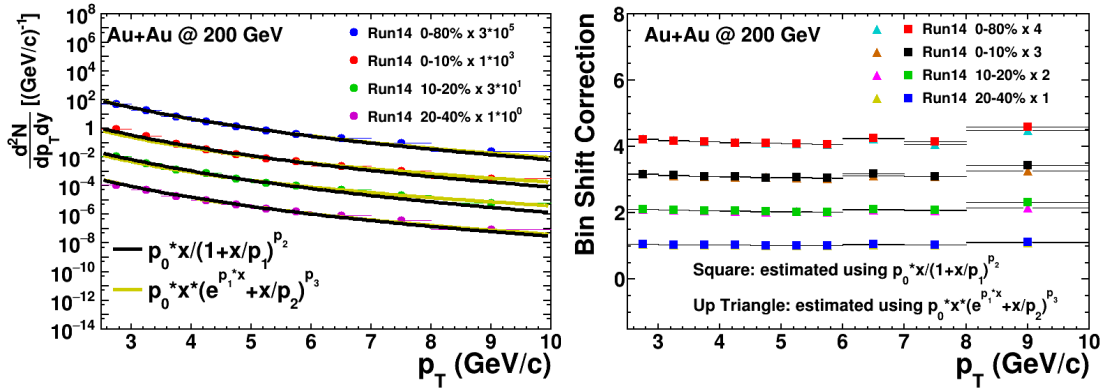


Fig. 3.60 Left panel: NPE p_T spectra without bin shift correction in different centralities, along with two different function fittings. Right panel: Bin shift correction factors as a function of p_T from two different function fittings in different centralities.

3.2.9. Systematic uncertainties

The systematic uncertainties for NPE have four primary sources: cuts, electron purity extraction, efficiency and background from J/Ψ decay. In $Au + Au$ collisions, the systematic uncertainties except additional trigger efficiency and J/Ψ decayed electron contribution uncertainties were obtained using the same method in $p + p$ collisions. For the systematic uncertainty from trigger efficiency was calculated by changing the $ADC0$ cut to 260 for HT1 and 308 for HT2, which as a function of p_T in 0-80% centrality is shown in the left panel of Fig 3.61. The systematic uncertainty of J/Ψ decayed electron contribution, which as a function of p_T in 0-80% centrality is shown in the right

panel of Fig. 3.61, was caused by the dN/dy uncertainty of J/Ψ . The total systematic

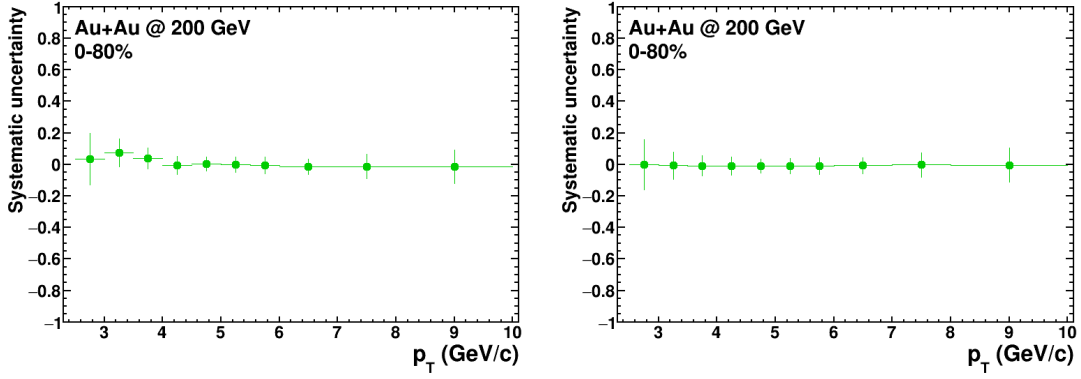


Fig. 3.61 Left panel: Systematic uncertainty of trigger efficiency as a function of p_T in 0-80% centrality. Right panel: Systematic uncertainty of J/Ψ decayed electron contribution as a function of p_T in 0-80% centrality.

uncertainties in different centralities were obtained through error transfer formula and are shown in Fig. 3.62.

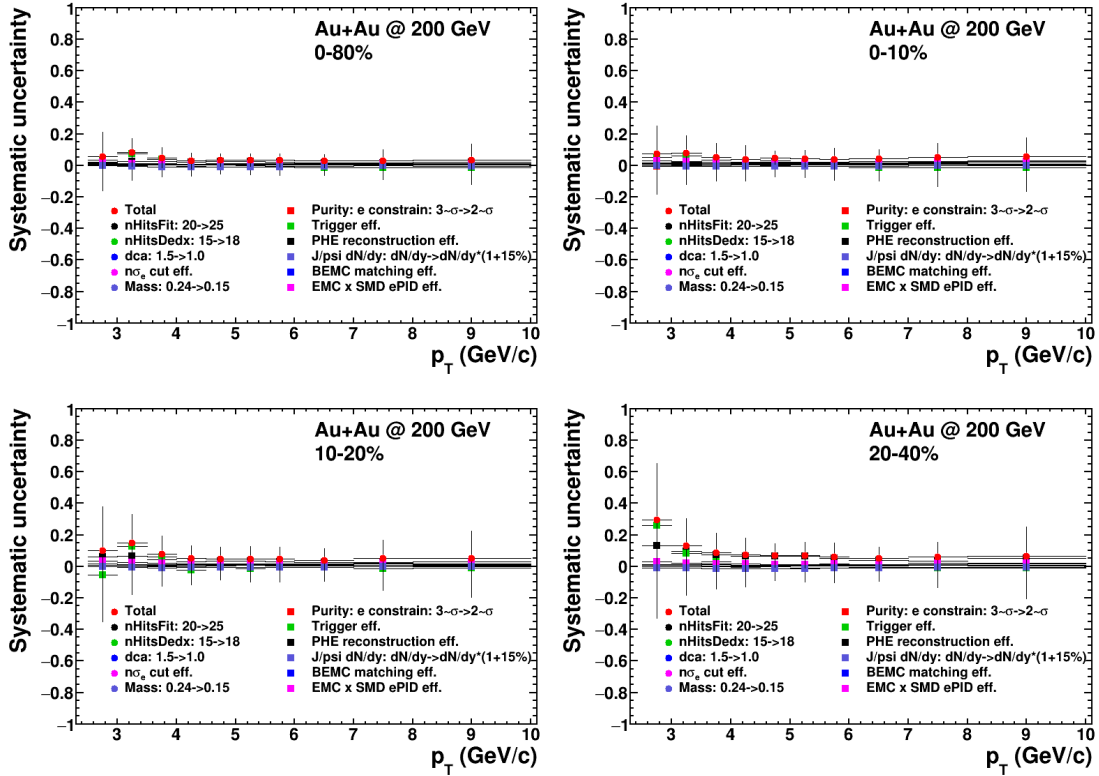


Fig. 3.62 Total systematic uncertainties as a function of p_T in different centralities.

Chapter 4 Results and Discussion

4.1 Cross-section of NPE at low p_T in 200 GeV $p + p$ collisions

The measured NPE cross-section for p+p collisions at $\sqrt{s} = 200$ GeV from year 2012 data is shown in the top-right panel of Fig. 4.1, along with the FONLL pQCD calculation. The bottom panel of Fig. 4.1 shows the ratio of data to FONLL calculation. The error bars depict the statistical uncertainties. The boxes represent the systematic uncertainties. The uncertainty band of FONLL calculation was obtained through independently varying the factorization and normalization scales with an additional uncertainty from varying charm and bottom masses. The final uncertainty is the quadratic sum of all uncertainties [120]. The new measurement extends to the lower p_T region compared to the previous STAR measurement [121] and is consistent with the FONLL prediction upper limit. Furthermore this provides more precise reference for R_{AA} in heavy-ion collisions. Due to the large uncertainties in the gluon density function and the dramatic increase of strong coupling constant towards low p_T , pQCD calculations have little predictive power for the charm cross-section at low p_T [70]. The top-left panel of Fig. 4.1 shows the ratio of signal (NPE) to background (photonic electrons) as a function of p_T .

4.2 Invariant yields and R_{AA} of NPE at high p_T in 200 GeV $Au + Au$ collisions

The measured NPE invariant yields for Au+Au collisions at $\sqrt{s_{NN}} = 200$ GeV from year 2014 data are shown in Fig. 4.2 for different centralities, along with a comparison to the FONLL pQCD calculation scaled by N_{coll} . In central collisions, there are significant differences between Au+Au measurements and the scaled FONLL calculation despite of the large log-scale spanned in the figure, indicating the existence of hot medium effects. From central to peripheral collisions, the difference is getting smaller, which is consistent with the expectation of less QGP effects in peripheral collisions.

Fig. 4.3 shows the signal to background ratios as a function of p_T in different centralities. Due to the increased gamma conversions with the newly installed HFT and the supporting structure in Run14, the signal to background ratio decreased by about a factor of 3-4 for central Au+Au collisions in Run14 compared to that in Run10 [16].

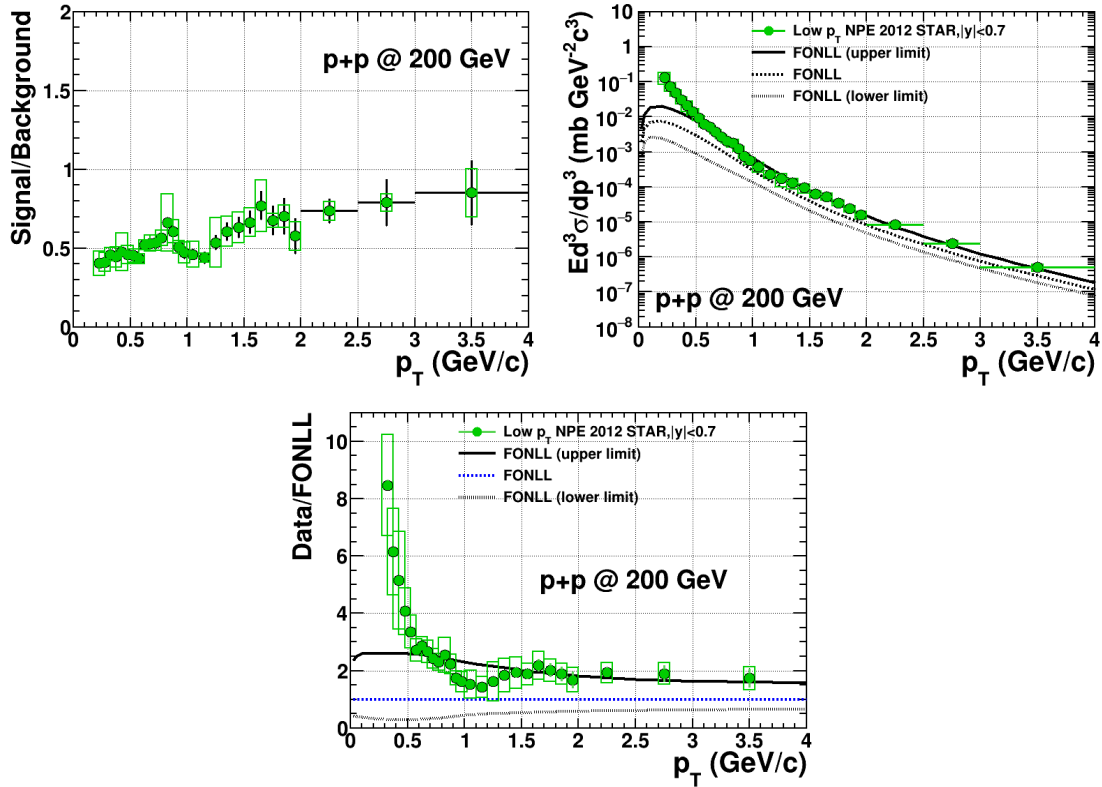


Fig. 4.1 Top-left panel: Ratio of signal to background as a function of p_T . Top-right panel: Cross-section of NPE as a function of p_T . Bottom panel: Ratio of data to the pQCD calculation as a function of p_T .

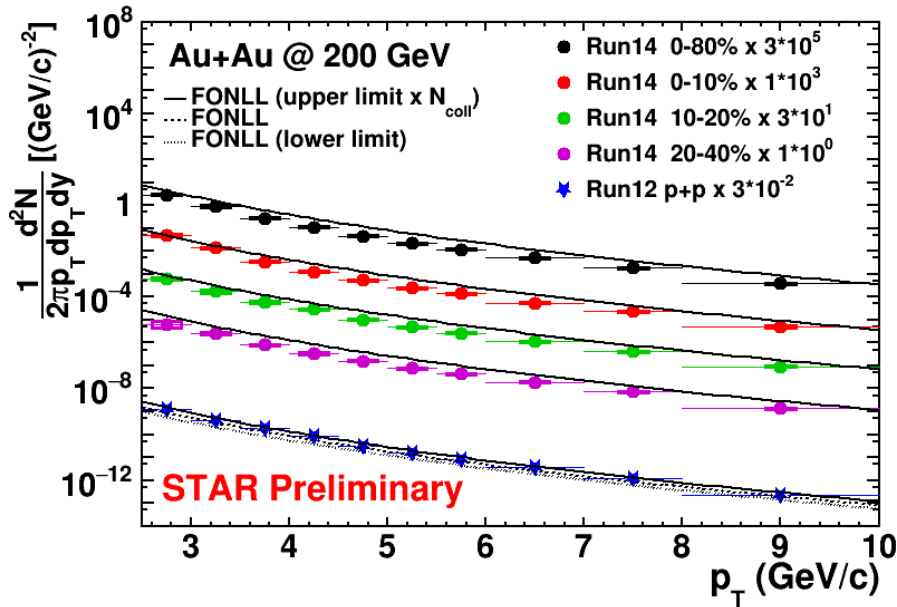


Fig. 4.2 NPE invariant yields as a function of p_T in different centralities for Au+Au collisions at $\sqrt{s_{NN}} = 200$ GeV, and scaled STAR preliminary p+p [15]. Error bars are statistical errors, and boxes are point-by-point systematic uncertainties.

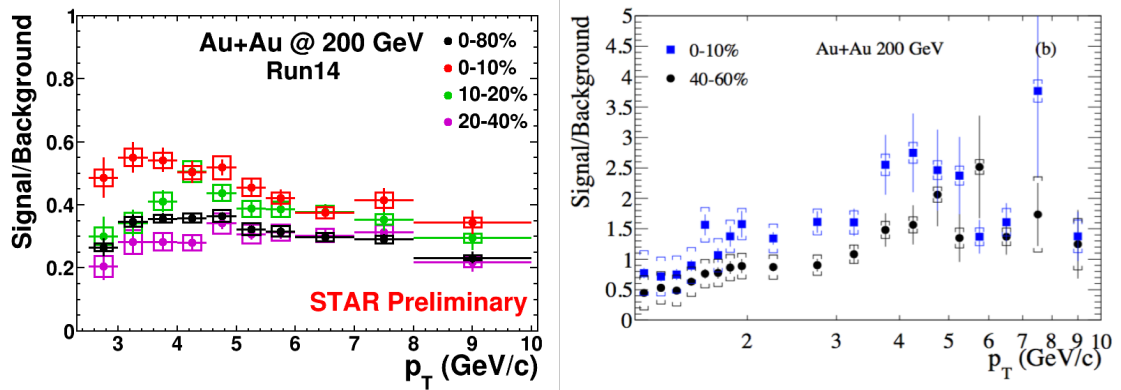


Fig. 4.3 Signal to background ratios as a function of p_T in different centralities in Run14 and Run10 [16] for Au+Au collisions at $\sqrt{s_{NN}} = 200$ GeV.

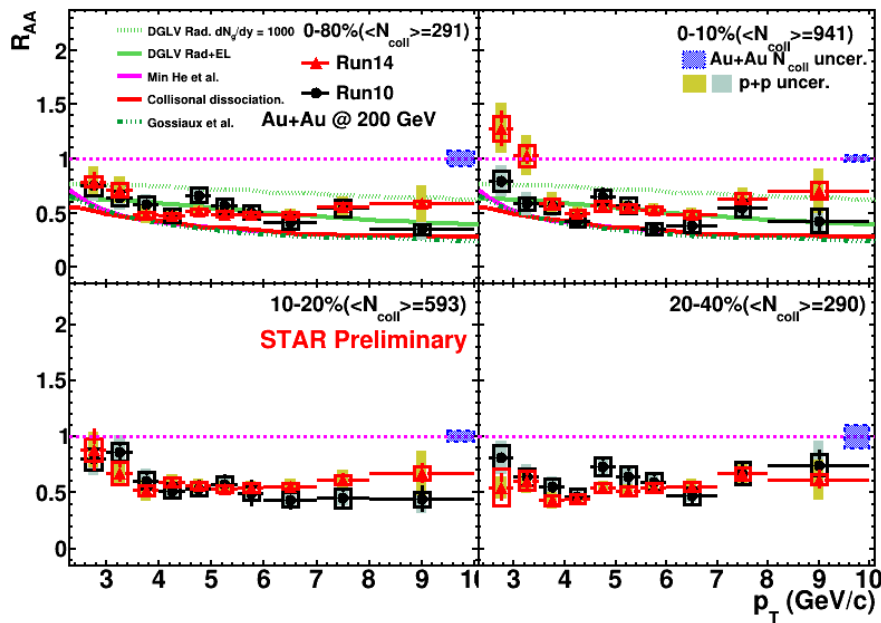


Fig. 4.4 NPE R_{AA} as a function of p_T in different centralities of Au+Au collisions at $\sqrt{s_{NN}} = 200$ GeV. Bars and Error boxes are statistical and systematic errors, respectively. Bands around each data point depict the uncertainties from the p+p baseline measurement.

In Fig. 4.4, there are four panels showing R_{AA} in different centralities. As we can see, the new Run14 results are consistent with Run10 results and have greatly reduced uncertainties despite of large difference in photonic electron background in all presented centralities (first two data points in 0-10% centrality need to be checked). We observe the strong suppression at high p_T in central collisions. Different model calculations were compared with our data in the 0-10% centrality. The DGLV model with only radiative energy loss via few hard scatterings with initial gluon density $dNg/dy = 1000$ [122] underestimates the suppression of NPE. With the addition of the elastic collisional energy loss of heavy quarks with light partons, the model calculation agrees with our data better. The other models, Collisional dissociation from collisional dissociation of heavy mesons in QGP by deriving heavy meson survival and dissociation probability from the collisional broadening of their light cone wave function [123, 124], Min He [125, 126] et al. considering the heavy-quark diffusion and hadronization in quark-gluon plasma, and Gossiaux [127–129] et al. considering the radiative and collisional energy loss both calculated in a running α_s pQCD-inspired model have some difficulties to describe the data. However there is no measurement of most peripheral collisions (40-60%) for Run14 due to the photonic electron reconstruction efficiency has a large fluctuation.

4.3 R_{AA} at intermediate p_T in 200 GeV $Au + Au$ collisions

In last section, the R_{AA} as a function of high p_T in different centralities of Au+Au collisions at $\sqrt{s_{NN}} = 200$ GeV have been presented. But there are no measurements of NPE yields at low and intermediate p_T in different centralities for Run14 Au+Au collisions at $\sqrt{s_{NN}} = 200$ GeV. Using the yields of NPE from Run10 Au+Au collisions and Run12 p+p collisions, the R_{AA} in different centralities were extended to intermediate p_T , which are shown in Fig. 4.5. We observe the strong suppression at high p_T in central collisions, which reduces gradually towards peripheral collisions. At intermediate p_T , these models more or less can describe our data. And we observe that there is no obvious suppression at intermediate p_T across all centralities, with large systematic uncertainties from p+p reference. The new precise R_{AA} measurements provide more information for the investigation of heavy quark energy loss mechanism.

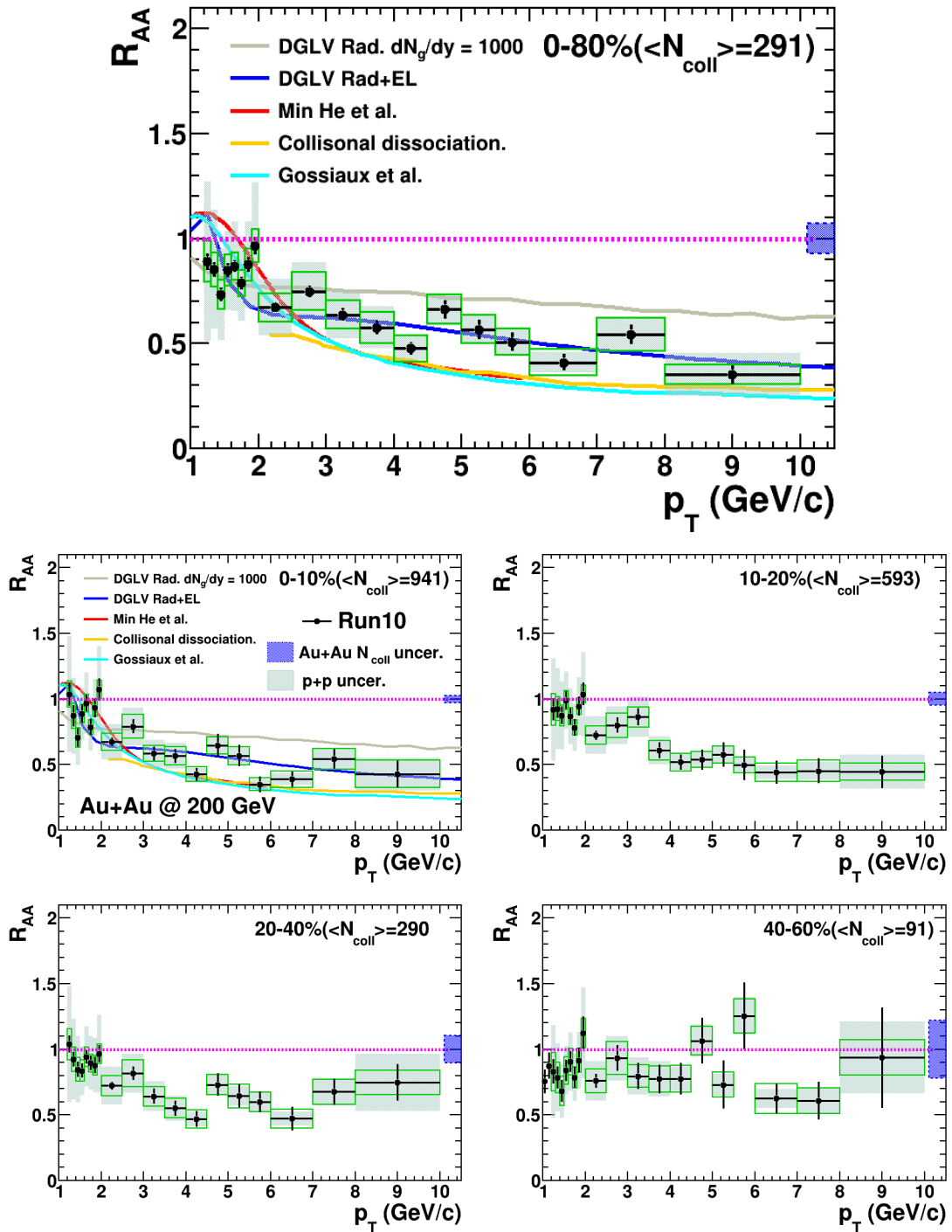


Fig. 4.5 NPE R_{AA} as a function of p_T for different centralities of Au+Au collisions at $\sqrt{s_{NN}} = 200$ GeV. Bars and Error boxes are statistical and systematic errors, respectively. Bands around each data point depict the uncertainties from the p+p baseline measurement.

4.4 Summary

We have presented the open heavy flavor hadron decayed electron (NPE) production cross-section in p+p collisions at $\sqrt{s} = 200$ GeV, which first extends the NPE measurement to low p_T (0.2 GeV/c). The new result with $p_T > 0.5$ GeV/c can be described by the pQCD calculation, which is consistent with the expectation that the pQCD calculation is only applicative at $p_T > m_{c,b}$, and the one with $p_T < 0.5$ GeV/c provides further constraints on theoretical calculations at low p_T . In particular, the increasing excess of the NPE cross-section below 0.5 GeV/c may hide some interesting production mechanisms, which deserves further investigation. In this thesis, we have completed the detailed study on the subtraction of non-photon electronic backgrounds including vector meson decays, K_{e3} , and as well as on the extraction of inclusive gamma spectrum, which is a good contribution to STAR physics analysis and provides a good technical reference for similar topics in this field.

The new measurements of NPE at high p_T for different centralities in Au+Au collisions at $\sqrt{s_{NN}} = 200$ GeV from Run14 have been presented, which have greatly reduced uncertainties compared to the previous STAR measurements from Run10 and can be used to cross-check NPE results with HFT. Together with the measurement at high p_T in p+p collisions as reference, the NPE R_{AA} at high p_T for different centralities in Au+Au collisions at $\sqrt{s_{NN}} = 200$ GeV are presented. Strong suppression is observed at high p_T in central collisions, which is consistent with the scenario of substantial energy loss of heavy quarks in the hot and dense matter. The DGLV model calculation, considering the radiative energy loss of heavy quarks via few hard scatterings and the elastic collisional energy loss of heavy quarks with light partons, can describe our data better than the other models. Furthermore, the NPE R_{AA} will serve as a reference for the isolation of bottom and charm quark hadrons.

Taking advantage of the new NPE p+p reference and the Run10 NPE spectra in Au+Au collisions at $\sqrt{s_{NN}} = 200$ GeV, the NPE R_{AA} at intermediate p_T for different centralities are presented. There is no obvious suppression at intermediate p_T across all centralities. However, it needs to be further confirmed with the measurement of NPE R_{AA} with improved precision.

Chapter 5 Outlook

As we discussed in the introduction chapter, heavy quarks are predominantly produced in hard scatterings (because of $m_{c,b} \gg \Lambda_{QCD}$) at early stages of the relativistic heavy-ion collisions before the creation of the deconfined QCD medium (due to $m_{c,b} \gg T_{QGP}$). They subsequently traverse the created system throughout its evolution thereby carry information of interactions with the medium, and thus are suggested as an excellent probe for studying the properties of the QGP. The energy loss of heavy quarks is considered as a unique tool to study the interactions between heavy quarks and the QCD medium created in the heavy-ion collisions, and provide us important information of the medium properties. As we discussed in the chapter of results and discussion, there is not a excellent model calculation can describe our R_{AA} results very well at intermediate and high p_T . So what can we do for measuring the heavy quark production via electron channel to know how the behavior of heavy flavor decayed electrons can reflect heavy quarks? By comparing the yields of heavy flavor hadron decayed electrons at high p_T in $Au + Au$ collisions with those in $p + p$ collisions at $\sqrt{s_{NN}} = 200$ GeV, a significant suppression has been observed. This suppression is believed to be caused by the energy loss of heavy flavor quarks through interactions with the QGP, which is expected to be different for bottom and charm quarks because of their different masses [130]. Separate measurements of open bottom and charm hadron production in $Au + Au$ collisions are crucial to test the mass hierarchy of the parton energy loss in the QGP. So what is the contribution of bottom in single electron measurements?

5.1 The Heavy Flavor Tracker

The HFT, whose physical goal is to identify short displaced vertices of open heavy flavor particles, need to provide an excellent track pointing resolution for precise measurements of displaced vertices. In addition, HFT is also required to have a excellent tracking resolution to match tracks from TPC with the corresponding hits in the vertex detector due to the TPC has not enough good resolution to allocate hits in the vertex detector for TPC identified particles with high efficiency in the high-multiplicity heavy ion collisions. So it was designed to be composed of three sub-detectors: the two layers silicon PiXeL detector (PXL) lay at the radius of 2.8 cm and 8 cm, the Intermediate Silicon Tracker (IST) at 14 cm and the Silicon Strip Detector (SSD) at 22 cm. A schematic

view of the different HFT layers is shown in Fig. 5.1.

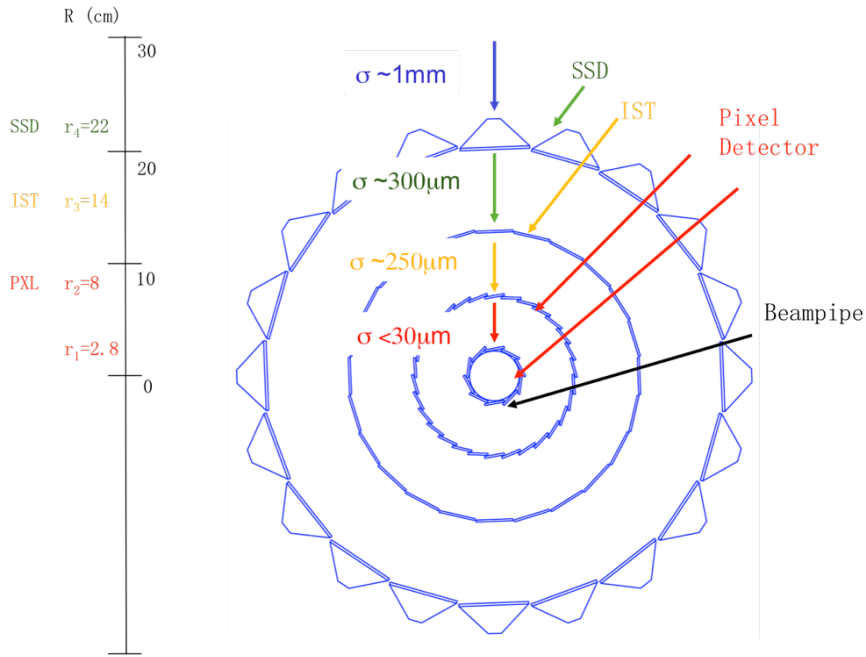


Fig. 5.1 Schematic view of the different layers of the HFT.

The PXL is the innermost sub-detector of HFT. It is a double layers detector with 40 ladders (10 inner and 30 outer ones) based on the CMOS Monolithic Active Pixel Sensors (MAPS) [131] technology. Each ladder has 10 MAPS sensors with $2 \text{ cm} \times 2 \text{ cm}$, on which there are 928×960 pixels array with $20.7 \times 20.7 \mu\text{m}$ pitch [132]. The MAPS not only makes PXL has an excellent resolution, but also is a low radiation length material. It makes the thickness of each layer only as 0.4% radiation length, which can minimize a contribution from multiple scattering effect to pointing resolution. The outermost of HFT is the SSD. It is a single-layer double-sided silicon strip sensors with $95 \mu\text{m}$ pitch and the thickness is about 1% radiation length. The position resolution of SSD is $20 \mu\text{m}$ in the $r \times \phi$ direction and $740 \mu\text{m}$ in the z direction. It is an existing detector with electronics upgrade. The PXL has provided the excellent pointing resolution, but the SSD only has a good resolution in the $r \times \phi$ direction. To reach the physics capabilities of the HFT, the IST is placed at between PXL and SSD. The track reconstruction efficiency yields improvement by combining SSD and IST to guide the track from the outer TPC to the inner PXL detector. The IST is a single-sided double-metal silicon pad sensors with $6000 \mu\text{m} \times 600 \mu\text{m}$ pad size and has a thickness of less than 1.5% radiation length. Its position resolution is $170 \mu\text{m}$ in the $r \times \phi$ direction and 1.8 mm in the z direction. The resolution of HFT is less than $30 \mu\text{m}$ for charged particles with $p_T > 1.5 \text{ GeV}/c$. Therefore, the HFT can be used to identify particles from charm and

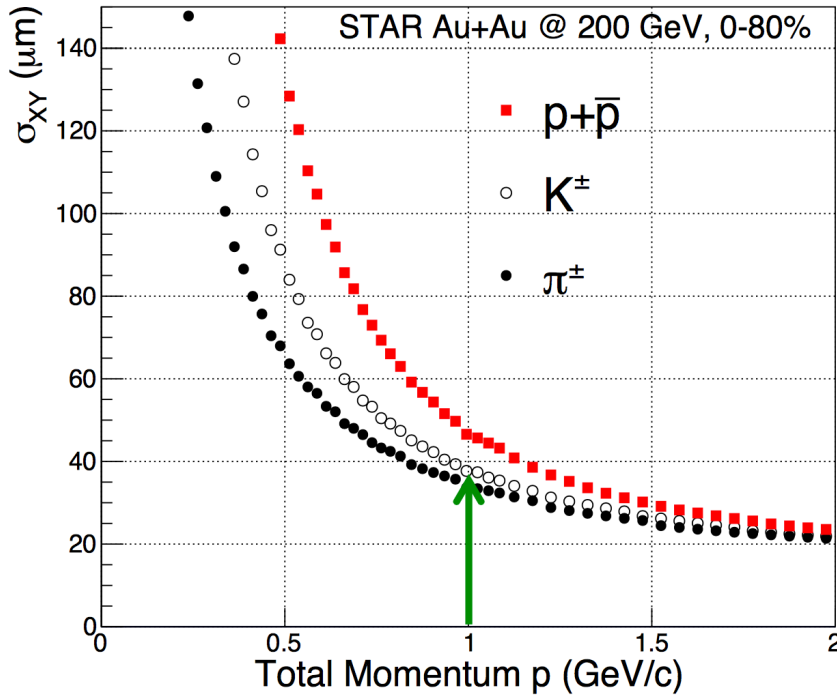


Fig. 5.2 Track pointing resolution in the transverse plane as a function of particle momentum.

bottom hadron decays by taking advantage of their different decay lengths. Figure 5.2 shows the track pointing resolution in the transverse plane as a function of momentum for identified particles.

5.2 Invariant yields and R_{AA} of NPE in 200 GeV $Au + Au$ collisions

In this analysis about NPE production in $Au + Au$ collisions, the newly-installed HFT was not employed, because the simulation and embedding of HFT was not ready at that time. As soon as the complete simulation and embedding of HFT are done, we will reanalysis the current data with HFT, which could extend the analysis to peripheral centrality classes and enable us to separate the contribution from B-hadron and C-hadron. And the results from this analysis can then served a good baseline to check the validity of the analysis with HFT. Furthermore, we plan to analysis the MB dataset from RHIC Run 2014 and 2016, focus on the NPE production at low and intermediate p_T range. Together with precise $p + p$ result in this thesis, we could extract the R_{AA} of NPE at low and intermediate p_T range with much better precision than the previous measurements from Run10. With the excellent performance of HFT, we can also have direct precise measurement of D^0 via hadronic channel [10]. However, due to the lack of statistic and

large combinatorial background, the measurement of D^0 at $p_T < 1$ GeV/ c and $p_T > 6$ GeV/ c is poor, which prevents us to get precise R_{AA} results at these p_T range. Coming back to the NPE analysis, benefit from the large branching ratio and BEMC trigger ability, we can have precise R_{AA} measurements of NPE at these low and high p_T region, which is very important for studying the interactions between heavy quarks and QGP, and can provide us important information of QGP properties.

5.3 Bottom decayed electrons in 200 GeV $Au + Au$ collisions

There are about 900 million MB and ~ 0.2 nb $^{-1}$ HT trigger $Au + Au$ events at $\sqrt{s_{NN}} = 200$ GeV from 2014 data for the separation of open bottom and charm hadron production. Due to the B and D hadrons have different lifetime. For example, the c_τ of D^0 and B^0 is about 123 μm and 459 μm respectively. The HFT can be used to identify particles from charm and bottom hadron decays by taking advantage of their different decay lengths because of its precise reconstruction of displaced decay vertices.

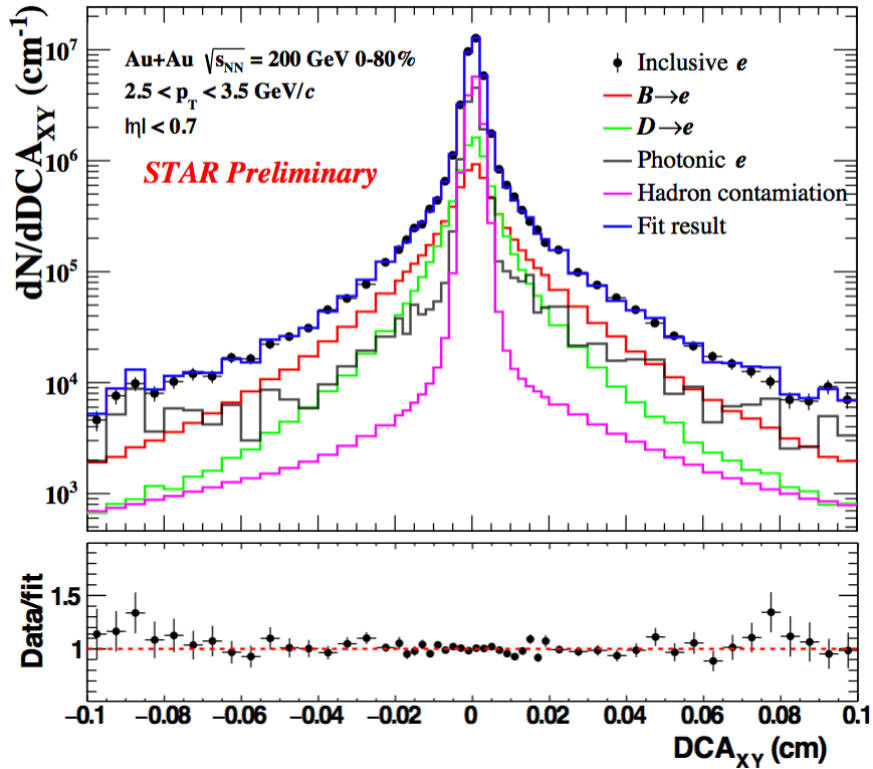


Fig. 5.3 *Top* : DCA_{XY} distribution for inclusive electrons with a template fit including $B \rightarrow e$, $D \rightarrow e$, and background electrons. *Bottom* : Ratio of data to the fitted template.

The DCA to the collision primary vertex was used to separate the bottom hadron decayed electrons ($B \rightarrow e$) from charm hadron decayed electrons ($D \rightarrow e$). The measured

DCA distribution in the transverse plane (DCA_{XY}) for inclusive electrons is shown in the upper panel of Fig. 5.3, along with the template fit including $B \rightarrow e$, $D \rightarrow e$, background from photonic electrons, and hadron contamination. The templates for $B \rightarrow e$ and $D \rightarrow e$ were obtained from a data-driven simulation coupled with a EvtGen[133] decayer (D^0, D^\pm, B^0 and B^\pm). The DCA_{XY} distribution for $B \rightarrow e$ is broader than that for $D \rightarrow e$ on account of the longer lifetime of B hadrons. The template for photonic electrons, arising from gamma conversions, π^0 and η Dalitz decays, was obtained from data corrected for the electron reconstruction efficiency extracted from embedding based on HIJING[134] simulations. Furthermore, hadrons misidentified as electron candidates need to be accounted for. Their template was obtained from data and the magnitude was constrained by the inclusive electron purity. The lower panel of Fig. 5.3 shows the ratio between data to the combined template fit, which agrees with data quite well. Using these results, the fraction of $B \rightarrow e$ to open heavy flavor hadron decayed electrons was obtained, which is shown as red circles in Fig. 5.4, along with that in $p + p$ collisions (blue circles) [135]. An enhancement of the fraction of $B \rightarrow e$ was observed in $Au + Au$ collisions compared to $p + p$ collisions.

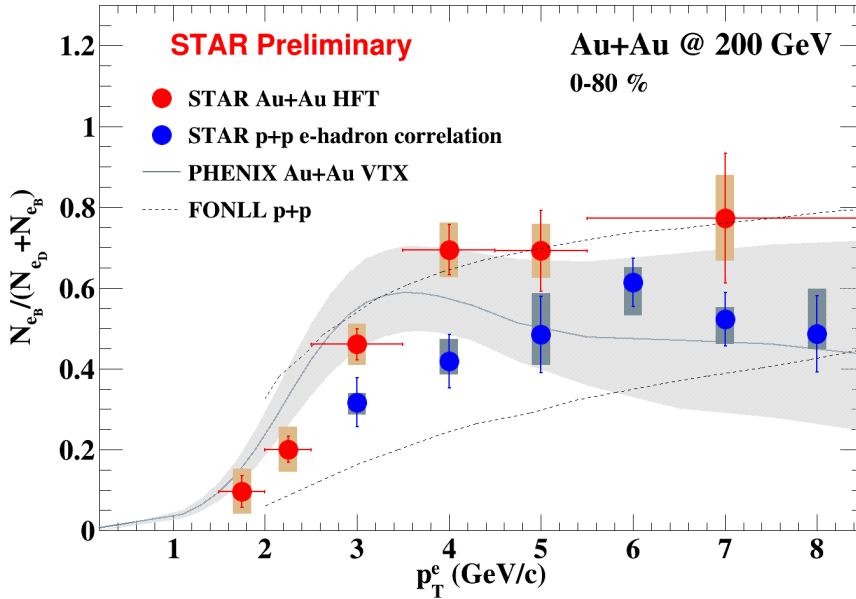


Fig. 5.4 Fraction of $B \rightarrow e$ to open heavy flavor hadron decayed electrons in 200 GeV $p + p$ and $Au + Au$ collisions.

The R_{AA} of $B \rightarrow e$ and $D \rightarrow e$ are obtained using:

$$R_{AA}^{B \rightarrow e} = \frac{f_{Au+Au}^{B \rightarrow e}(data)}{f_{p+p}^{B \rightarrow e}(data)} R_{AA}^{HF_e}(data), \quad R_{AA}^{D \rightarrow e} = \frac{1 - f_{Au+Au}^{B \rightarrow e}(data)}{1 - f_{p+p}^{B \rightarrow e}(data)} R_{AA}^{HF_e}(data), \quad (5.1)$$

where $f^{B \rightarrow e}$ is the fraction of $B \rightarrow e$ in $Au + Au$ or $p + p$ collisions, and $R_{AA}^{HF_e}$ the R_{AA}

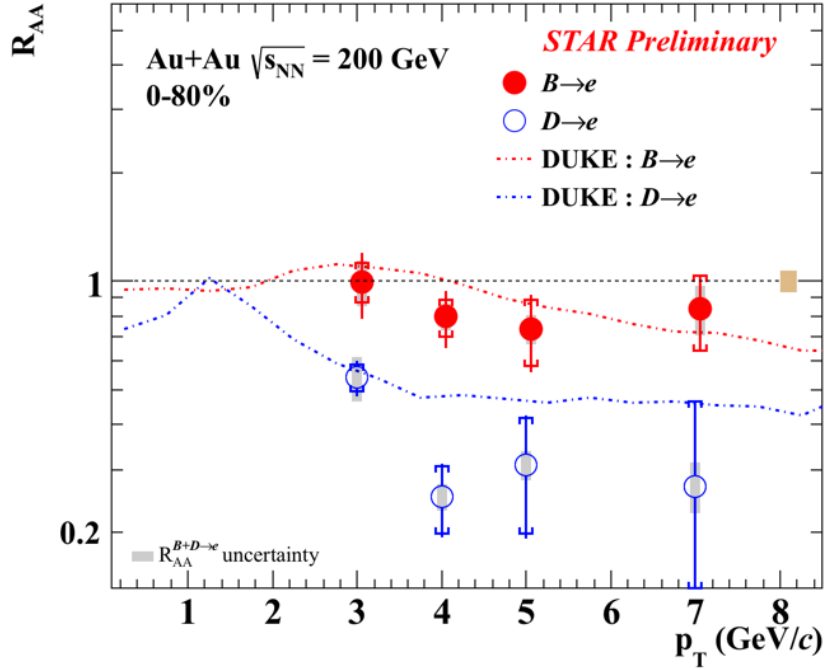


Fig. 5.5 $R_{AA}^{B \rightarrow e}$ and $R_{AA}^{D \rightarrow e}$ as a function of p_T .

of open heavy flavor hadron decayed electrons (from my result in Fig. 4.4). Fig. 5.5 shows $R_{AA}^{B \rightarrow e}$ and $R_{AA}^{D \rightarrow e}$, along with a comparison to the DUKE model calculation for $B \rightarrow e$ and $D \rightarrow e$ [136] in 0-80% central $Au + Au$ collisions. The $R_{AA}^{D \rightarrow e}$ is less than $R_{AA}^{B \rightarrow e}$ at $\sim 2\sigma$ significance level, which is qualitatively described by the DUKE model calculation [136]. This is consistent with the theoretical prediction that bottom quarks should lose less energy than charm quarks due to their larger mass. In 2016, there were a factor of ~ 2 more minimum-bias and ~ 5 more high- p_T electron triggered events in 200 GeV $Au + Au$ collisions events recorded by the STAR experiment, which can be used to further improve the precision of the measurements for electrons from B-hadron decays. In addition, the inclusive gamma spectra detailedly studied by we have been used to the template fit of background from photonic electrons. About this and the detailed information of the separation of B-hadron and D-hadron decayed electrons can be found at [137, 138].

For STAR, the open bottom hadron production can be measured through multiple decay channels, $B \rightarrow e$, D^0 , J/Ψ in $Au + Au$ collisions at $\sqrt{s_{NN}} = 200$ GeV. However, due to the lack of available data with HFT in $p + p$ collisions, we could not make measurements of $B \rightarrow D^0$, J/Ψ in $p + p$ collisions. The study of the mass hierarchy of the parton energy loss in the QGP via $B \rightarrow D^0$, J/Ψ channels will rely on the model calculation from $p + p$ collisions [73]. So the bottom production measurement through

the electron channel is indispensable for STAR.

Bibliography

- [1] BERINGER J, et al. Review of Particle Physics[J]. Phys. Rev. D, 2012, 86(1): 010001.
- [2] DAS D. Recent results from STAR experiment in Au+Au collisions at $\sqrt{s_{NN}} = 9.2$ GeV [C]/Nuclear Experiment. 2009.
- [3] DUKE U. <http://www.phy.duke.edu>[M].
- [4] CAINES H. What's interesting about strangeness production? An overview of recent results [C]//: volume 31. 2005: S101.
- [5] SCHNEDERMANN E, et al. Thermal phenomenology of hadrons from 200A gev S+S collisions[J]. Phys. Rev. C, 1993, 48(5): 2462.
- [6] ZHANG Y. Measurement of charm production cross-section and leptons from its semileptonic decay at RHIC[D]. Hefei: University of Science and Technology of China, 2007.
- [7] IANCU E. Qcd in heavy ion collisions[J]. CERN, 2014, 003: 197–266.
- [8] ADAMCZYK L, et al. Measurement of d^0 Azimuthal Anisotropy at Midrapidity in Au+Au Collisions at $\sqrt{s_{NN}} = 200$ GeV[J]. Phys. Rev. Lett., 2017, 118(21): 212301.
- [9] ADAMCZYK L, et al. Measurements of D^0 and D^* Production in $p + p$ Collisions at $\sqrt{s} = 200$ GeV[J]. Phys. Rev. D, 2012, 86(7): 072013.
- [10] SPECTRA PAPER DRAFT D. <http://www.star.bnl.gov/protected/heavy/xgn1992/Centrality/Run2014/VPDMB5/index.html>[M].
- [11] OPEN CHARM HADRON PRODUCTION IN P+P A, AT STAR U C. https://indico.cern.ch/event/219436/contributions/1522978/attachments/355691/495401/yezhenyu_QM2014_v7.pdf[M].
- [12] BUZZATTI A, GYULASSY M. Erratum: Transverse Momentum and Centrality Dependence of High- p_T Nonphotonic Electron Suppression in Au+Au Collisions at $\sqrt{s_{NN}} = 200$ GeV [*Phys. Rev. Lett.* 98, 192301 (2007)][J]. Phys. Rev. Lett., 2011, 106(15): 159902.
- [13] BUZZATTI A, GYULASSY M. Jet Flavor Tomography of Quark Gluon Plasmas at RHIC and LHC[J]. Phys. Rev. Lett., 2012, 108(2): 022301.
- [14] BUZZATTI A, GYULASSY M. Measurement of the Bottom Quark Contribution to Nonphotonic Electron Production in p+p Collisions at $\sqrt{s} = 200$ GeV[J]. Phys. Rev. Lett., 2010, 105(20): 202301.
- [15] BAI X. Measurements of Open Heavy Flavor Production in Semi-leptonic Channels at STAR [J]. Nuclear Physics A, 2016, 956: 513–516.
- [16] MUSTAFA M. EXPERIMENTAL STUDY OF ELECTRONS FROM HEAVY FLAVOR HADRONS DECAYS IN AU+AU COLLISIONS AT 200, 62.4 AND 39 GEV IN THE STAR

BIBLIOGRAPHY

- EXPERIMENT AT RHIC[D]. West Lafayette, Indiana: Purdue University, 2013.
- [17] BLOOM E D, et al. HIGH-ENERGY INELASTIC e-p SCATTERING AT 6° AND 10° [J]. Phys. Rev. Lett., 1969, 23(16): 930.
- [18] BJORKEN B J, GLASHOW S L. Elementary particles and SU(4)[J]. Phys. Lett., 1964, 11 (3): 255–257.
- [19] BREIDENBACH M, et al. OBSERVED BEHAVIOR OF HIGHLY INELASTIC ELECTRON-PROTON SCATTERING[J]. Phys. Rev. Lett., 1969, 23(16): 935.
- [20] ABE F, et al. Observation of Top Quark Production in $\bar{p}p$ Collisions with the Collider Detector at Fermilab[J]. Phys. Rev. Lett., 1995, 74(14): 2626.
- [21] HERB S W, et al. Observation of a Dimuon Resonance at 9.5 GeV in 400-GeV Proton-Nucleus Collisions[J]. Phys. Rev. Lett., 1977, 39(5): 252.
- [22] AAD G, et al. Broken Symmetries and the Masses of Gauge Bosons[J]. Phys. Rev. Lett., 1964, 13(16): 508.
- [23] HIGGS P W. Observation of a new particle in the search for the Standard Model Higgs boson with the ATLAS detector at the LHC[J]. Phys. Lett. B, 2012, 716(1): 1–29.
- [24] FRITZSCH H, GELL-MANN M. Quarks and what else?[C]//eConfC720906V2. 1972: 135–165.
- [25] GROSS D J, WILCZEK F. Ultraviolet Behavior of Non-Abelian Gauge Theories[J]. Phys. Rev. Lett., 1973, 30(26): 1343.
- [26] POLITZER H D. Reliable Perturbative Results for Strong Interactions?[J]. Phys. Rev. Lett., 1973, 30(26): 1346.
- [27] GROSS D J, WILCZEK F. Asymptotically Free Gauge Theories. I[J]. Phys. Rev. D, 1973, 8(10): 3633.
- [28] POLITZER H D. Asymptotic freedom: An approach to strong interactions[J]. Phys. Rep., 1974, 14(4): 129.
- [29] BETHKE S. The 2009 world average of α_s [J]. Eur. Phys. J. C, 2009, 64(4): 689–703.
- [30] GUPTA R. Introduction to Lattice QCD[M]. 1998.
- [31] SHURYAK E V. Quantum chromodynamics and the theory of superdense matter[J]. Phys. Rept., 1980, 61(2): 71–158.
- [32] BRAUN-MUNZINGER P, STACHEL J. The quest for the quark–gluon plasma[J]. Nature, 2007, 448(7151): 302–309.
- [33] ELLIS J. From Little Bangs to the Big Bang[J]. J. Phys. Conf. Ser., 2006, 50: 8–21.
- [34] SARKAR, et al. The physics of the quark-gluon plasma[M]. [S.l.]: Springer, 1985.
- [35] HELMUTSATZ. Colour screening in SU(N) gauge theory at finite temperature[J]. Nucl. Phys. A, 1984, 418: 447–465.

BIBLIOGRAPHY

- [36] BETHKE S. Lattice QCD at High Temperature and Density[J]. Lect.Notes Phys., 2002, 583: 209–249.
- [37] FODOR Z, et al. The QCD equation of state at nonzero densities: lattice result[J]. Phys. Lett. B, 2003, 568(1-2): 73–77.
- [38] FODOR Z, KATZ S. Critical point of QCD at finite T and μ , lattice results for physical quark masses[J]. JHEP, 2004, 0404: 050.
- [39] GAVAI R V, GUPTA S. Simple patterns for nonlinear susceptibilities near T_c [J]. Phys. Rev. D, 2005, 72(5): 054006.
- [40] AGGARWAL M M, et al. An Experimental Exploration of the QCD Phase Diagram: The Search for the Critical Point and the Onset of De-confinement[J]. arXiv:1007.2613v1, 2010.
- [41] HARRISON M, et al. Rhic project overview[J]. Nucl. Instr. Meth. A, 2003, 499(2-3): 235–244.
- [42] BRAUN-MUNZINGER P, et al. Chemical equilibration in Pb+Pb collisions at the SPS[J]. Phys. Lett. B, 1999, 465(1-4): 15–20.
- [43] MILLER M L, et al. Glauber Modeling in High-Energy Nuclear Collisions[J]. Annu. Rev. Nucl. Part. Sci., 2007, 57: 205–243.
- [44] KOLB P F, HEINZ U. Hydrodynamic description of ultrarelativistic heavy-ion collisions[J]. arXiv: nucl-th/0305084, 2003.
- [45] ADAMS J, et al. Experimental and Theoretical Challenges in the Search for the Quark Gluon Plasma: The STAR Collaboration’s Critical Assessment of the Evidence from RHIC Collisions[J]. Nucl. Phys. A, 2005, 757(1-2): 102–183.
- [46] K.GUETTLER, et al. Inclusive production of low-momentum charged pions at $x = 0$ at the CERN intersecting storage rings[J]. Phys. Lett. B, 1976, 64(1): 111–116.
- [47] ADAMS J, et al. Identified Particle Distributions in pp and Au+Au Collisions at $\sqrt{s_{NN}} = 200$ GeV[J]. Phys. Rev. Lett., 2004, 92(11): 112301.
- [48] ADAMS J, et al. Particle-Type Dependence of Azimuthal Anisotropy and Nuclear Modification of Particle Production in Au+Au Collisions at $\sqrt{s_{NN}} = 200$ GeV[J]. Phys. Rev. Lett., 2004, 92(5): 052302.
- [49] ADAMS J, et al. ϕ meson production in Au+Au and p+p Collisions at $\sqrt{s_{NN}} = 200$ GeV[J]. Phys. Lett. B, 2005, 612(3-4): 181–189.
- [50] CASTILLO J, et al. Elliptic flow of multistrange baryons Ξ and Ω in Au+Au collisions at $\sqrt{s_{NN}} = 200$ GeV[C]//: volume 30. 2004: S1207.
- [51] ZHANG Y. Open charm production in $\sqrt{s_{NN}} = 200$ GeV Au+Au collisions[C]//: volume 32. 2006: S529–S532.
- [52] ADAMS J, et al. Centrality Dependence of High- p_T Hadron Suppression in Au+Au

- Collisions at $\sqrt{s_{NN}} = 130$ GeV[J]. Phys. Rev. Lett., 2002, 89(20): 202301.
- [53] WONG C Y. Introduction to High-Energy Heavy-Ion Collisions[M]. [S.l.]: World Scientific Publishing Co. Pte. Ltd, 1994.
- [54] ADAMS J, et al. Evidence from d+Au Measurements for Final-State Suppression of High- p_T Hadrons in Au+Au Collisions at RHIC[J]. Phys. Rev. Lett., 2003, 91(7): 072304.
- [55] ESKOLA K, et al. THE SCALE DEPENDENT NUCLEAR EFFECTS IN PARTON DISTRIBUTIONS FOR PRACTICAL APPLICATIONS[J]. Eur. Phys. J. C, 1999, 9(1): 61–68.
- [56] DE FLORIAN D, SASSOT R. Nuclear parton distributions at next to leading order[J]. Phys. Rev. D, 2004, 69(7): 074028.
- [57] KOPELIOVICH B Z. Transparent nuclei and deuteron-gold collisions at relativistic energies [J]. Phys. Rev. C, 2003, 68(4): 044906.
- [58] VOGT R. Shadowing effects on the nuclear suppression factor, R_{dAu} , in d+Au interactions [J]. Phys. Rev. C, 2004, 70(6): 064902.
- [59] ACCARDI A, GYULASSY M. Cronin effect and geometrical shadowing in d+Au collisions: pQCD versus colour glass condensate[C]//: volume 30. 2004: S969.
- [60] ACCARDI A, GYULASSY M. Cronin effect vs. geometrical shadowing in d+Au collisions at RHIC[J]. Phys. Lett. B, 2004, 586(3-4): 244–253.
- [61] CATTARUZZA E, TRELEANI D. Cronin effect and energy conservation constraints in high energy proton-nucleus collisions[J]. Phys. Rev. D, 2004, 69(9): 094006.
- [62] BARNAFÖLDI G G, et al. Cronin effect at different rapidities at RHIC[C]//J. Phys. G: Nucl. Part. Phys.: volume 30. 2004: S1125.
- [63] MOLNÁR D, VOLOSHIN S A. Elliptic Flow at Large Transverse Momenta from Quark Coalescence[J]. Phys. Rev. Lett., 2003, 91(9): 092301.
- [64] WEI LIN Z, KO C M. Flavor Ordering of Elliptic Flows at High Transverse Momentum[J]. Phys. Rev. Lett., 2002, 89(20): 202302.
- [65] UPHOFF J, et al. Heavy-quark production in ultrarelativistic heavy-ion collisions within a partonic transport model[J]. Phys. Rev. C, 2010, 82(4): 044906.
- [66] LÉVAI P, et al. Open charm production in an equilibrating parton plasma[J]. Phys. Rev. C, 1995, 51(6): 3326.
- [67] LÉVAI P, VOGT R. Thermal charm production by massive gluons and quarks[J]. Phys. Rev. C, 1997, 56(5): 2707.
- [68] MÜLLER B. Hadronic signals of deconfinement at rhic[J]. Phys. Rev. A, 2005, 750(1): 84–97.
- [69] JACOBS P, WANG X N. Matter in extremis: ultrarelativistic nuclear collisions at RHIC[J]. Progress in Part. and Nucl. Phys., 2005, 54(2): 443–534.

BIBLIOGRAPHY

- [70] VOGT R. The total charm cross section[J]. *Eur. Phys. J. ST.*, 2008, 155(1): 213–222.
- [71] VOGT R. Determining the uncertainty on the total heavy-flavor cross section[J]. *Eur. Phys. J. C*, 2009, 61: 793.
- [72] BUZZATTI A, GYULASSY M. Measurement of the Bottom Quark Contribution to Nonphotonic Electron Production in p+p Collisions at $\sqrt{s} = 200$ GeV[J]. *Phys. Lett. B*, 2001, 519(3-4): 199–206.
- [73] OH K. Measurements of open bottom and charm hadron productions through multiple decay channels in p+p and Au+Au collisions with the STAR experiment[J]. *Nuclear Physics A*, 2017, 967: 632–635.
- [74] RHIC. <https://www.bnl.gov/rhic/default.asp>[M].
- [75] FISCHER W. <http://www.agrhome.bnl.gov/RHIC/Runs/>[M].
- [76] ALESSI J. ELECTRON BEAM ION SOURCE PRE-INJECTOR PROJECT (EBIS) CONCEPTUAL DESIGN REPORT[R]. [S.l.]: <https://www.bnl.gov/isd/documents/30527.pdf>, 2005.
- [77] STAR. <http://www.star.bnl.gov>[M].
- [78] PHENIX. <http://www.phenix.bnl.gov>[M].
- [79] ACKERMANN K H, et al. STAR detector overview[J]. *Nucl. Instr. Meth. A*, 2003, 499(2-3): 624–632.
- [80] BEAVIS D. The STAR Heavy Flavor Tracker Technical Design Report[R]. [S.l.]: <https://drupal.star.bnl.gov/STAR/starnotes/public/sn0600>, 2011.
- [81] ANDERSON M, et al. The STAR time projection chamber: a unique tool for studying high multiplicity events at RHIC[J]. *Nucl. Instr. Meth. A*, 2003, 499(2-3): 659–678.
- [82] LLOPE W J. The TOFP/pVPD time-of-flight system for STAR[J]. *Nucl. Instr. Meth. A*, 2004, 522(3): 252–273.
- [83] BEDDO M, et al. The STAR Barrel Electromagnetic Calorimeter[J]. *Nucl. Instr. Meth. A*, 2003, 499(2-3): 725–739.
- [84] BERGSMA F, et al. The STAR detector magnet subsystem[J]. *Nucl. Instr. Meth. A*, 2003, 499(2-3): 633–639.
- [85] RUAN L, et al. Perspectives of a mid-rapidity dimuon program at the RHIC: a novel and compact muon telescope detector[C]//*J. Phys. G: Nucl. Part. Phys.*: volume 36. 2009: 095001.
- [86] BIESER F S, et al. The STAR trigger[J]. *Nucl. Instr. Meth. A*, 2003, 499(2-3): 766–777.
- [87] LLOPE W J, et al. The STAR Vertex Position Detector[J]. *Nucl. Instr. Meth. A*, 2014, 759: 23–28.
- [88] JR. C A W. The Beam-Beam Counter: A Local Polarimeter at STAR[C]//*AIP Conference Proceedings*: volume 980. 2008: 390.

BIBLIOGRAPHY

- [89] ADLER C, et al. The RHIC zero-degree calorimeters[J]. Nucl. Instr. Meth. A, 2003, 499(2-3): 433–436.
- [90] ANDERSON M, et al. A readout system for the STAR time projection chamber[J]. Nucl. Instr. Meth. A, 2003, 499(2-3): 679–691.
- [91] BUREN G V, et al. Correcting for Distortions due to Ionization in the STAR TPC[J]. Nucl. Instr. Meth. A, 2006, 566(1): 22–25.
- [92] BICHSEL H. A method to improve tracking and particle identification in TPCs and silicon detectors[J]. Nucl. Instr. Meth. A, 2006, 562(1): 154–197.
- [93] BICHSEL H. Stopping power and ranges of fast ions in heavy elements[J]. Phys. Rev. A, 1992, 46(9): 5761–5773.
- [94] LLOPE W J. Multigap RPCs in the STAR experiment at RHIC[J]. Nucl. Instr. Meth. A, 2012, 661(1): 110–113.
- [95] TANG Z. *J/Psi* production at high transverse momentum in p+p and a+a collisions[D]. Hefei: University of Science and Technology of China, 2009.
- [96] ADCOX K, et al. Measurement of Single Electrons and Implications for Charm Production in Au+Au Collisions at $\sqrt{s_{NN}} = 130$ GeV[J]. Phys. Rev. Lett., 2002, 88(19): 192303.
- [97] DONG X. Single Electron Transverse Momentum and Azimuthal Anisotropy Distributions: Charm Hadron Production at RHIC[D]. Hefei: University of Science and Technology of China, 2005.
- [98] ADARE A, et al. Detailed measurement of the e^+e^- pair continuum in p+p and Au+Au collisions at $\sqrt{s_{NN}} = 200$ GeV and implications for direct photon production[J]. Phys. Rev. C, 2010, 81(3): 034911.
- [99] ADAMS J, et al. Identified hadron spectra at large transverse momentum in p+p and d+Au collisions at $\sqrt{s_{NN}} = 200$ GeV[J]. Phys. Lett. B, 2006, 637(3): 161–169.
- [100] RUAN L. Pion, Kaon, Proton and Antiproton Spectra in d+Au and p+p Collisions at $\sqrt{s_{NN}} = 200$ GeV at the Relativistic Heavy Ion Collider[D]. Hefei: University of Science and Technology of China, 2004.
- [101] ADAMS J, et al. Pion, kaon, proton and anti-proton transverse momentum distributions from p+p and d+Au collisions at $\sqrt{s_{NN}} = 200$ GeV[J]. Phys. Lett. B, 2005, 616(1-2): 8–16.
- [102] ADLER S S, et al. High transverse momentum η meson production in p+p, d+Au, and Au+Au collisions at $\sqrt{s_{NN}} = 200$ GeV[J]. Phys. Rev. C, 2007, 75(2): 024909.
- [103] ADARE A, et al. Centrality dependence of low-momentum direct-photon production in Au+Au collisions at $\sqrt{s_{NN}} = 200$ GeV[J]. Phys. Rev. C, 2015, 91(6): 064904.
- [104] ADLER S S, et al. Measurement of Direct Photon Production in p+p Collisions at $\sqrt{s} = 200$ GeV[J]. Phys. Rev. Lett., 2007, 98(1): 012002.

BIBLIOGRAPHY

- [105] ADARE A, et al. Direct photon production in p+p collisions at $\sqrt{s} = 200$ GeV at midrapidity [J]. Phys. Rev. D, 2012, 86(7): 072008.
- [106] CROSS SECTION J, EVENT ACTIVITIES IN P+P COLLISIONS. http://www.star.bnl.gov/protected/heavy/huangbc/web/jpsi_production_and_event_activites/SupportingDoc/Jpsi_evtAct_anaNote_v14.pdf[M].
- [107] ADAMCZYK L, et al. Di-electron spectrum at mid-rapidity in p+p collisions at $\sqrt{s_{NN}} = 200$ GeV[J]. Phys. Rev. C, 2012, 86(2): 024906.
- [108] SKANDS P Z. Tuning Monte Carlo Generators: The Perugia Tunes[J]. Phys. Rev. D, 2010, 82(7): 074018.
- [109] ABELEV B I, et al. Strange particle production in p+p collisions at $\sqrt{s_{NN}} = 200$ GeV[J]. Phys. Rev. C, 2007, 75(6): 064901.
- [110] ADAMS J, et al. Transverse-Momentum and Collision-Energy Dependence of High- p_T Hadron Suppression in Au+Au Collisions at Ultrarelativistic Energies[J]. Phys. Rev. Lett., 2003, 91(17): 172302.
- [111] DEFINITION C. <http://www.star.bnl.gov/protected/heavy/xgn1992/Centrality/Run2014/VPDMB5/index.html>[M].
- [112] DETAILED INFORMATION C D. https://www.star.bnl.gov/protected/heavy/xgn1992/paper/D0spectra/note/20171102_D0spectra_Note.pdf[M].
- [113] HADRON SAMPLE IN AU+AU COLLISIONS P. <https://drupal.star.bnl.gov/STAR/system/files/pureSampleNoHFT.pdf>[M].
- [114] ABELEV B, et al. Systematic Measurements of Identified Particle Spectra in pp, d+Au and Au+Au Collisions from STAR[J]. Phys. Rev. C, 2009, 79(3): 034909.
- [115] ADAMS J, et al. Identified Particle Distributions in p+p and in Au+Au Collisions at $\sqrt{s_{NN}} = 200$ GeV[J]. Phys. Rev. Lett., 2004, 92(11): 112301.
- [116] ADLER S S, et al. High transverse momentum η meson production in p+p, d+Au, and in Au+Au collisions at $\sqrt{s_{NN}} = 200$ GeV[J]. Phys. Rev. C, 2007, 75(2): 024909.
- [117] ADARE A, et al. Enhanced Production of Direct Photons in Au+Au Collisions at $\sqrt{s_{NN}} = 200$ GeV and Implications for the Initial Temperature[J]. Phys. Rev. Lett., 2010, 104(13): 132301.
- [118] ADARE A, et al. Measurement of Direct Photons in Au+Au Collisions at $\sqrt{s_{NN}} = 200$ GeV [J]. Phys. Rev. Lett., 2012, 109(15): 152302.
- [119] TODOROKI T. Quarkonium measurements via the di-muon decay channel in p+p and Au+Au collisions with the STAR experiment[C]//Journal of Physics: Conference Series: volume 779. 2017: 012040.
- [120] AGGARWAL M M, et al. QCD Predictions for Charm and Bottom Quark Production at

BIBLIOGRAPHY

- RHIC[J]. Phys. Rev. Lett., 2005, 95(12): 122001.
- [121] AGAKISHIEV H, et al. High p_T nonphotonic electron production in p+p collisions at $\sqrt{s_{NN}} = 200$ GeV[J]. Phys. Rev. D, 2011, 83(5): 052006.
- [122] DJORDJEVIC M, et al. Influence of bottom quark jet quenching on single electron tomography of Au+Au[J]. Phys. Lett. B, 2006, 632(1): 81–86.
- [123] SHARMA R, et al. Light-cone wave function approach to open heavy flavor dynamics in QCD matter[J]. Phys. Rev. C, 2009, 80(5): 054902.
- [124] SHARMA R, et al. Collisional dissociation of heavy mesons in dense QCD matter[J]. Phys. Lett. B, 2007, 649(2-3): 139–146.
- [125] HE M, et al. Heavy-quark diffusion and hadronization in quark-gluon plasma[J]. Phys. Rev. C, 2012, 86(1): 014903.
- [126] CAO S, et al. Heavy-quark dynamics and hadronization in ultrarelativistic heavy-ion collisions: Collisional versus radiative energy loss[J]. Phys. Rev. C, 2013, 88(4): 044907.
- [127] GOSSIAUX P B, et al. Competition of heavy quark radiative and collisional energy loss in deconfined matter[J]. J. Phys. G: Nucl. Part. Phys., 2010, 37(9): 094019.
- [128] GOSSIAUX P B, AICHELIN J. Toward an understanding of the single electron data measured at the BNL Relativistic Heavy Ion Collider (RHIC)[J]. Phys. Rev. C, 2008, 78(1): 014904.
- [129] AICHELIN J, et al. RADIATIVE AND COLLISIONAL ENERGY LOSS OF HEAVY QUARKS IN DECONFINED MATTER□[J]. Acta Phys. Polon. B, 2012, 43(4): 655–662.
- [130] BUZZATTI A, GYULASSY M. Jet Flavor Tomography of Quark Gluon Plasmas at RHIC and LHC[J]. Phys. Rev. Lett., 2012, 108(2): 022301.
- [131] HU-GUO C, et al. First reticule size MAPS with digital output and integrated zero suppression for the EUDET-JRA1 beam telescope[C]/Nucl. Instr. Meth. A: volume 623. 2010: 480–482.
- [132] QIU H. STAR heavy flavor tracker[C]/Nuclear Physics A: volume 931. 2014: 1141–1146.
- [133] LANGE D J. The EvtGen particle decay simulation package[J]. Nuclear Instruments and Methods in Physics Research A, 2001, 462(1-2): 152–155.
- [134] WANG X N, GYULASSY M. Hijing: A Monte Carlo model for multiple jet production in pp, pA, and AA collisions[J]. Phys. Rev. D, 1991, 44(11): 3501.
- [135] AGGARWAL M M, et al. Measurement of the Bottom Quark Contribution to Nonphotonic Electron Production in p+p Collisions at $\sqrt{s}= 200$ GeV[J]. Phys. Rev. Lett., 2010, 105(20): 202301.
- [136] CAO S, et al. Energy loss, hadronization, and hadronic interactions of heavy flavors in relativistic heavy-ion collisions[J]. Phys. Rev. C, 2015, 92(2): 024907.
- [137] DONG X. Measurements of open heavy flavor production in p+p and Au+Au collisions at

BIBLIOGRAPHY

- RHIC energy[D]. Wuhan: Central China Normal University, 2017.
- [138] OH K. Charm and Bottom Hadron Production via Semi-leptonic Decay Channel in Relativistic Heavy Ion Collisions[D]. Pusan: Pusan National University, 2017.

Acknowledgements

弹指一挥，六年时间已过，毕业论文开篇之时，想着在致谢篇，要怎样怎样表达，写出自己的特色，在论文完成之际，突然发现最简单的感谢才是最真诚的。在这六年里，要感谢的人太多太多。

首先，感谢我的导师李澄教授，李老师渊博的知识，严谨的科研态度以及和蔼可亲的为人让我受益良多。感谢我的老师张一飞，在博士期间的研究工作都是在张一飞老师的指导下完成的，他知识层面广泛，科研想法极多，使我在科研方面获益匪浅，能力得到很大的提升，为我博士论文的完成倾注了很大的心血和汗水。感谢 UIC 的叶震宇老师，他做事认真，精益求精的科研态度，使我在做科研的过程中踏踏实实。感谢唐泽波老师，在科研和生活中对我给予很大的帮助，尤其在迷茫的时候，收到了很好的建议。感谢陈宏芳教授，陈老师广博的知识和持之以恒的科研态度令我非常敬佩。感谢周意老师，在硬件方面遇到麻烦，意哥总是不令赐教。感谢邵明老师，孙勇杰老师和李昕师兄在科研上的帮助。

感谢我的学长周龙，是他将一个刚入行，啥都不懂的菜鸟我，一步步带到了今天能独立完成科研任务的我，他很热心而且有耐心，总是细心地指导我，而且在生活中，遇到迷茫之际，总是悉心地开导我，使我能在科研的道路上走下去。感谢查王妹师兄，在科研中遇到不解的问题，跟他交流，总能使我茅塞顿开。感谢杨帅师兄，虽然相处时间很短，但是一直在科研和生活上给予我很多帮助，跟他的讨论，使我对很多不解的问题有了更深刻的认识。感谢杨钱，不仅是师兄，也是能一起玩耍的朋友，有了他的陪伴，在博士辛苦的这六年间，有了很多欢乐。也感谢江琨师兄，张辉师兄，杨驰师兄，黄卫平师兄，帅鹏师兄，朱银莹师姐，陈天翔师兄，王小壮师兄和刘钦师兄。同时也感谢 UIC 的黄炳鑫师兄，Zach，叶早晨师兄，王霄，罗四维和白晓智，给了在国外的我生活和科研上的帮助。

感谢我们同一级的赵晓坤，尤文豪，杨荣星和谢冠男，一起度过了在教室上课的最后的时光。感谢实验室的师弟和师妹们，刘圳，陈小龙，胡东栋，孙艳坤，王鹏飞，纪媛婧，巨欣跃，宋国锋，吴奕涛，周健，李子味，李洋，李子洋，吕游，曹泽华和洪道金，因为有了你们，实验室才多了很多欢笑。

感谢我的父母和姐姐，是他们一直的支持和鼓励，我才能很好地完成博士期间的学习和科研，在遇到困难时能坚持下来。也感谢我的男神羽生结弦，每当在困难和遇到烦恼时，看着他的微笑和活成热血动漫的花滑人生，就觉着人生在世没有什么困难是过不去的。最后，想说，命运对勇士低语，你将无法抵御风暴，勇士低声应语，我就是风暴，以此献给自己以后的人生。最后的最后，对大家再一次表达感谢，希望大家身体健康，生活幸福。

Publications

已发表论文

1. Measurements of Open Heavy Flavor Production in Semi-leptonic Decay Channels at the STAR experiment; HOT QUARKS 2016 proceeding; J. Phys.: Conf. Ser. 832(1) 012032, 2017.
2. Open Bottom Production in Au+Au Collisions at $\sqrt{s_{NN}} = 200$ GeV with the STAR Experiment; PANIC 2017 Proceeding; Int. J. Mod. Phys. Conf. Ser., 46, 1860014 (2018).

待发表论文

1. Multiplicity Dependence of Charged Particle, ϕ Meson and Multi-strange Particle Productions in p+p Collisions at $\sqrt{s} = 200$ GeV with PYTHIA Simulation; Have submitted to Physical Review C and been waiting for review response (<https://arxiv.org/abs/1803.05767>).
2. Measurements of Open Heavy Flavor Production in Semi-leptonic Channels at the STAR; one of PAs, Prepare to submit to Physical Review C.

研究报告

1. Measurements of electrons from heavy flavor decays in Au+Au collisions at $\sqrt{s_{NN}} = 200$ GeV by the STAR experiment; 2017 APS Prairie Section Fall Meeting; 2017/11/11-2017/11/12; 美国伊利诺伊州芝加哥伊利诺伊大学芝加哥分校.
2. Measurements of open bottom and charm hadron production through multiple decay channels in Au+Au collisions at $\sqrt{s_{NN}} = 200$ GeV with the STAR experiment; Particles and Nuclei International Conference 2017(PANIC2017); 2017/09/01-2017/09/05; 中国北京中国科学院高能物理研究所.
3. Measurements of electron production from open heavy flavor decays in Au+Au collisions at $\sqrt{s_{NN}} = 200$ GeV by the STAR experiment; the 12th workshop on QCD phase transitions and relativistic heavy ion collisions (QPT2017); 2017/07/21-2017/07/23; 中国陕西西安西安交通大学.

4. Measurements of Open Heavy Flavor Production in Semi-leptonic Channels at the STAR experiment; 第十七届全国中高能核物理大会; 2017/05/05-2017/05/09; 中国湖北宜昌三峡大学.
5. Measurements of electron production from open heavy flavor decays in Au+Au collisions at $\sqrt{s_{NN}} = 200$ GeV by the STAR experiment; QUARK MATTER 2017; 2017/02/05-2017/02/11; 美国伊利诺伊州芝加哥伊利诺伊大学芝加哥分校.
6. Measurements of Open Heavy Flavor Production in Semi-leptonic Channels at the STAR experiment; 33rd Winter Workshop on Nuclear Dynamics (WWND 2017); 2017/01/08-2017/01/14; 美国犹他州盐湖城休斯顿大学.
7. Measurements of Open Heavy Flavor Production in Semi-leptonic Channels at the STAR experiment; HOT QUARKS 2016; 2016/09/12-2016/09/17; 美国德克萨斯州南帕诸岛.
8. Measurements of heavy flavor decay electron production in p+p collisions at $\sqrt{s} = 200$ GeV at STAR; QUARK MATTER 2015; 2015/09/27-2015/10/03; 日本神户东京大学.
9. Measurements of heavy flavor decay electron production at STAR; 第十六届全国中高能核物理大会; 2015/08/19-2015/08/23; 中国重庆西南大学.
10. *R&D* of Forward EMC for eSTAR (BSO Calorimeter); STAR Regional Meeting; 2013/09/09-2013/09/11; 中国安徽合肥中国科学技术大学.